

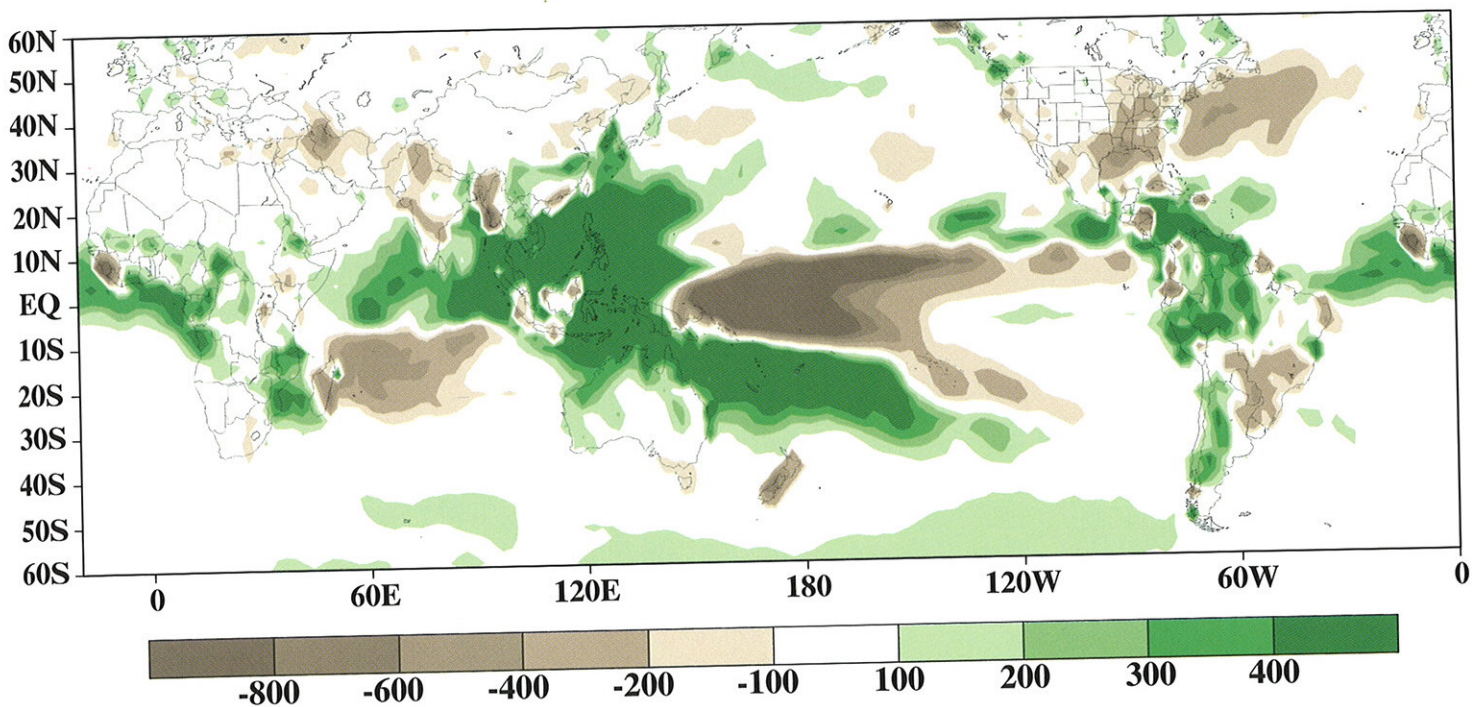
# CLIMATE ASSESSMENT FOR 1999

Gerald Bell,<sup>1</sup> Michael S. Halpert,<sup>1</sup> Russell C. Schnell,<sup>2</sup> R. Wayne Higgins,<sup>1</sup>  
Jay Lawrimore,<sup>3</sup> Vernon E. Kousky,<sup>1</sup> Richard Tinker,<sup>1</sup> Wasila Thiaw,<sup>1</sup>  
Muthuvel Chelliah,<sup>1</sup> and Anthony Artusa<sup>1</sup>

<sup>1</sup>Climate Prediction Center, NCEP/NWS/NOAA, Washington, DC

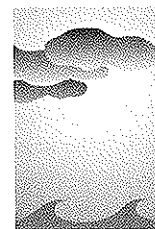
<sup>2</sup>Climate Monitoring and Diagnostics Laboratory, NOAA, Boulder, CO

<sup>3</sup>National Climatic Data Center, NESDIS/NOAA, Asheville, NC



Reprinted from the *Bulletin of the American Meteorological Society*,  
Vol. 81, No. 6, June 2000





# Climate Assessment for 1999

Gerald D. Bell,\* Michael S. Halpert,\* Russell C. Schnell,+ R. Wayne Higgins,\*  
Jay Lawrimore,# Vernon E. Kousky,\* Richard Tinker,\* Wasila Thiaw,\*  
Muthuvel Chelliah,\* and Anthony Artusa\*

## ABSTRACT

The global climate during 1999 was impacted by Pacific cold episode (La Niña) conditions throughout the year, which resulted in regional precipitation and atmospheric circulation patterns across the Pacific Ocean and the Americas that are generally consistent with those observed during past cold episodes. The primary La Niña-related precipitation anomalies included 1) increased rainfall across Indonesia, and a nearly complete disappearance of rainfall across the east-central and eastern equatorial Pacific; 2) above-normal rains across northwestern and northern Australia; 3) increased monsoon rains across the Sahel region of western Africa; 4) above-average rains over southeastern Africa; 5) above-average rains over the Caribbean Sea and portions of Central America, and 6) below-average rains in southeastern South America.

The La Niña also contributed to persistent cyclonic circulation anomalies in the subtropics of both hemispheres, which flanked the area of suppressed convective activity over the eastern half of the equatorial Pacific. In the Northern Hemisphere this anomaly feature contributed to a pronounced westward retraction of the wintertime East Asian jet stream, which subsequently impacted precipitation and storm patterns across the eastern North Pacific and western North America. The La Niña-related pattern of tropical rainfall also contributed to a very persistent pattern of anticyclonic circulation anomalies in the middle latitude of both hemispheres, extending from the eastern Pacific across the Atlantic and Africa eastward to Australasia. This anomaly pattern was associated with an active Atlantic hurricane season, an inactive eastern North Pacific hurricane season, above-average rains in the African Sahel, and an overall amplification of the entire southeast Asian summer monsoon complex.

The active 1999 North Atlantic hurricane season featured 12 named storms, 8 of which became hurricanes, and 5 of which became intense hurricanes. The peak of activity during mid-August–October was accompanied by low vertical wind shear across the central and western Atlantic, along with both a favorable structure and location of the African easterly jet. In contrast, only 9 tropical storms formed over the eastern North Pacific during the year, making it one of the most inactive years for that region in the historical record. This relative inactivity was linked to a persistent pattern of high vertical wind shear that covered much of the main development region of the eastern North Pacific.

Other regional aspects of the short-term climate included: 1) above-average wintertime precipitation and increased storminess in the Pacific Northwest, United States; 2) above-average monsoonal rainfall across the southwestern United States; 3) drought over the northeastern quadrant of the United States during April–mid-August; 4) hurricane-related flooding in the Carolinas during September; 5) drought over the south-central United States during July–November; 6) below-average rainfall in the Hawaiian Islands throughout the year, with long-term dryness affecting some parts of the islands since October 1997; 7) a continuation of long-term drought conditions in southeastern Australia, with most of Victoria experiencing below-average rainfall since late 1996; and 8) above-average rainfall in central China during April–August.

Global annual mean surface temperatures during 1999 for land and marine areas were 0.41°C above the 1880–1998 long-term mean, making it the fifth warmest year in the record. However, significant cooling was evident in the Tropics during 1999 in association with a continuation of La Niña conditions. In contrast, temperatures in both the Northern Hemisphere and Southern Hemisphere extratropics were the second warmest in the historical record during 1999, and only slightly below the record 1998 anomalies.

The areal extent of the Antarctic ozone hole remained near record levels during 1999. The ozone hole also lasted longer than has been observed in past years.

\*Climate Prediction Center, NCEP/NWS/NOAA, Washington, D.C.

+Climate Monitoring and Diagnostics Laboratory, NOAA, Boulder, Colorado.

#National Climatic Data Center, NOAA, Asheville, North Carolina.

Corresponding author address: Michael S. Halpert, Climate Prediction Center, NCEP/NOAA, W/NP52, NSC, Rm. 605, 5200 Auth Rd., Camp Springs, MD 20746



# Table of Contents

1. Introduction .....	S3
2. Global temperatures .....	S3
a. Surface temperature .....	S3
b. Troposphere .....	S6
c. Lower stratosphere .....	S8
3. The 1998–2000 Pacific cold episode (La Niña) .....	S11
a. Overview .....	S11
b. Precipitation impacts .....	S12
c. SSTs and subsurface ocean structure .....	S13
d. Tropical convection .....	S14
e. Atmospheric circulation .....	S15
1) Pacific basin .....	S15
2) Zonally symmetric streamfunction anomaly pattern .....	S17
4. Regional climate highlights .....	S18
a. North America .....	S18
1) Heavy wintertime precipitation in the Pacific Northwest .....	S18
2) The 1999 North Atlantic and eastern North Pacific hurricane seasons .....	S19
3) The July–September 1999 southwestern United States summer monsoon .....	S23
4) Drought in the United States .....	S24
b. Africa .....	S29
1) The 1998–99 southern Africa rainy season .....	S29
2) June–September 1999: Western Africa rainy season .....	S31
c. Asia .....	S32
1) Indian summer monsoon .....	S32
2) Central China rainfall .....	S34
d. South America .....	S34
e. Storminess across central Europe .....	S35
1) Excessive January–February snow .....	S35
2) December wind storms .....	S37
f. Precipitation extremes in Australia .....	S37
1) Northern and northwestern Australia .....	S37
2) Southeastern Australia .....	S38
5. Trace gases .....	S39
a. Ozone .....	S39
1) Continental United States and Hawaii .....	S39
2) Southern Hemisphere ozone .....	S40
b. Carbon cycle greenhouse gases .....	S42
1) Carbon dioxide .....	S42
2) Methane .....	S43
3) Carbon monoxide .....	S44
c. Chlorofluorocarbons (CFCs) .....	S44
6. Seasonal summaries .....	S46
Appendix: Contributors .....	S50
Acknowledgments .....	S50
References .....	S50



## 1. Introduction

This annual climate assessment is the tenth in an ongoing series produced by the Climate Prediction Center. It is designed to provide a timely summary of the global climate system during 1999. Specific components of the assessment include a documentation of global climate variations, an examination of oceanic and atmospheric anomalies in the global Tropics and extratropics, and an analysis of selected significant regional climate highlights.

Issues related to global temperatures are addressed in section 2. In section 3 an analysis is presented of the Pacific cold episode (La Niña), which persisted throughout the year. The La Niña impacts on global precipitation and atmospheric circulation patterns are also examined. Regional climate highlights and summaries of the major monsoon systems are discussed in section 4. Topics include heavy wintertime precipitation in the Pacific Northwest United States, an active North Atlantic hurricane season, above-average monsoon rains over the southwestern United States, severe drought in the northeastern and south-central United States, above-average rains in southern Africa, the African Sahel, and northern/northwestern Australia, dryness in southeastern Australia, near-average monsoon rains in India, above-average rains in central China, excessive January–February snowfall in the Alps, and December wind storms in Europe.

In section 5, an assessment of various trace gas concentrations and their potential impacts on climate is presented. This analysis includes a description of the near-record Antarctic ozone hole during 1999, along with trends in such gases as carbon dioxide, carbon monoxide, methane, and several chlorofluorocarbon species. In section 6, seasonal maps of temperature anomalies, precipitation percentiles, and 500-hPa heights and anomalies are presented. These maps are included for reference, and to continue the analyses that have appeared in previous annual climate assessments. While each section is essentially self-contained, there is liberal cross-referencing between sections to aid navigation through the document.

A variety of data sources were used in the compilation of this assessment, including 1) gridded analyses from the National Centers for Environmental Prediction–National Center for Atmospheric Research (NCEP–NCAR) Climate Data Assimilation System/Reanalysis Project (Kalnay et al. 1996), 2) surface data obtained from the operational Global Telecommunications System (GTS), 3) satellites, 4) radiosondes,

and 5) ship reports. Selected analyses were also obtained from international climate data centers. It should be noted that due to the variety of different data sources used in this assessment, it is not possible to maintain a consistent base period among all anomaly fields.

## 2. Global temperatures

### a. Surface temperature

Global surface temperatures are based on data collected from over 1000 land-based weather stations, combined with a blended sea surface temperature (SST) dataset derived from satellite, ship, and ocean buoy measurements. The estimated 1999 global mean temperature for land and ocean combined was  $0.41^{\circ}\text{C}$  above the 1880–1998 long-term mean (Fig. 1a), which was the fifth warmest year in the record. However, the 1999 temperature was  $0.25^{\circ}\text{C}$  cooler than the record-breaking anomaly of  $0.66^{\circ}\text{C}$  recorded in 1998. A similar decrease in global mean temperatures between 1998 and 1999 was also reported by the Hadley Centre of the U.K. Meteorological Office and the Climatic Research Unit of the University of East Anglia, United Kingdom (WMO press release).

The anomalous warmth during 1999 continues a period of well above-average global temperatures that began in 1977. Since that time global temperatures have risen at a rate of  $0.16^{\circ}\text{C decade}^{-1}$ , which is much larger than the rate of  $0.04^{\circ}\text{C decade}^{-1}$  recorded prior to 1977. This rapid rise in temperatures in recent years made the decade of the 1990s the warmest in the record, with seven of the ten warmest years occurring since 1990.

The global mean SST during 1999 was  $0.26^{\circ}\text{C}$  above the 1880–1998 mean (Fig. 1b), which is  $0.25^{\circ}\text{C}$  lower than that recorded in 1998. The global mean land-only temperature during 1999 was  $0.76^{\circ}\text{C}$  above the 1880–1998 mean (Fig. 1c) and was the second warmest in the record. However, this value was still considerably lower than the record departure of  $1.02^{\circ}\text{C}$  set in 1998.

The most significant cooling during 1999 occurred in the Tropics ( $20^{\circ}\text{N}$ – $20^{\circ}\text{S}$ ), where the combined land–ocean anomaly of  $0.21^{\circ}\text{C}$  (Fig. 2b) was well below the record value of  $0.72^{\circ}\text{C}$  set in 1998. This drop in temperatures was evident in both the land-only ( $0.14^{\circ}\text{C}$ ) and SST-only ( $0.43^{\circ}\text{C}$ ) anomalies (not shown), both of which were more than  $0.5^{\circ}\text{C}$  below the record 1998 values. This relative cooling throughout the Tropics was linked to the persistence of La Niña conditions throughout the year (Fig. 3, also see section 3).



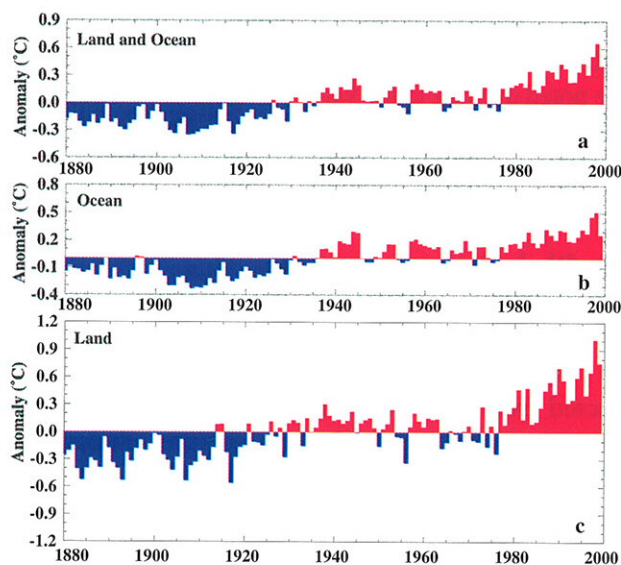


FIG. 1. Annual averages of global (a) combined land-air temperature and SST anomalies ( $^{\circ}\text{C}$ ), (b) SST anomalies, and (c) land-air temperature. Anomalies are departures from the 1880–1998 base period means. (Source: National Climatic Data Center.)

In contrast, temperatures during 1999 in both the Northern ( $20^{\circ}$ – $90^{\circ}\text{N}$ ; Fig. 2a) and Southern ( $20^{\circ}$ – $90^{\circ}\text{S}$ ; Fig. 2c) Hemisphere extratropics were the second warmest in the record dating back to 1880, and were only slightly below the record 1998 values. In the Northern Hemisphere extratropics, the 1999 mean land-only temperature anomaly was  $1.12^{\circ}\text{C}$ , while the mean SST anomaly was  $0.40^{\circ}\text{C}$  (not shown). These values were only  $0.05^{\circ}$  and  $0.1^{\circ}\text{C}$  below the record 1998 values, respectively.

The spatial pattern of mean annual temperature anomalies during 1999 (Fig. 3) featured below-average temperatures across the eastern half of the tropical Pacific, with temperatures ranging between  $1^{\circ}$  and  $2^{\circ}\text{C}$  below average across the equatorial Pacific east of  $170^{\circ}\text{E}$ . This anomalous cooling reflected the persistence of La Niña conditions throughout the year. Below-normal SSTs also prevailed along the west coast of the United States, across the higher latitudes of the North Pacific, and over the southeastern South Pacific. In contrast, above-normal SSTs covered much of the North Atlantic and South Atlantic Ocean basins during the year, with the largest positive anomalies (exceeding  $1^{\circ}\text{C}$ ) found over the central North Atlantic. Large areas of positive SST anomalies were also observed in the far western Pacific from  $20^{\circ}$  to  $45^{\circ}\text{N}$ , and along the west coast of Australia.

Most land areas recorded above-average temperatures for the year as a whole. This anomalous warmth

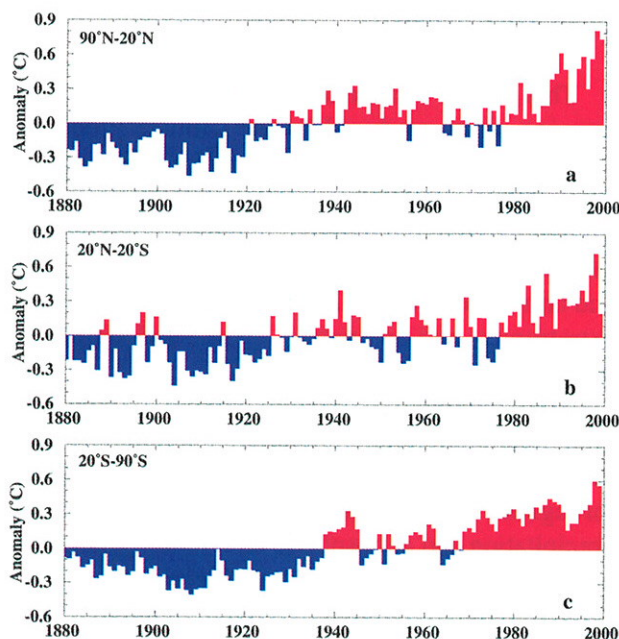


FIG. 2. Annual averages of combined land-air temperature and SST anomalies ( $^{\circ}\text{C}$ ): (a)  $20^{\circ}$ – $90^{\circ}\text{N}$ , (b)  $20^{\circ}\text{S}$ – $20^{\circ}\text{N}$ , and (c)  $20^{\circ}$ – $90^{\circ}\text{S}$ . Anomalies are departures from the 1880–1998 base period means. (Source: National Climatic Data Center.)

was particularly prominent across North America, where temperatures averaged  $1^{\circ}$ – $3^{\circ}\text{C}$  above normal across the eastern United States and central Canada, and more than  $3^{\circ}\text{C}$  above normal in northeastern Canada. Positive temperature anomalies were observed in these areas during much of the year (see section 6, Figs. 77a, 79a, 81a, 83a), in association with a persistent pattern of above-normal heights (see section 6, Figs. 78, 80, 82, 84) and anomalous anticyclonic circulations at upper levels that covered central North America and Canada (see section 3, Figs. 20a, 23). These conditions were accompanied by reduced snow cover duration across the central and eastern United States during December 1998–February 1999 (DJF) (Fig. 4a) and across the intermountain region of the western United States and large portions of central Canada during March–May 1999 (MAM) (Fig. 4b).

Annual mean temperatures during 1999 for Canada as a whole averaged  $1.7^{\circ}\text{C}$  above the 1961–90 mean (Fig. 5a), making it the third warmest year in the last 40 years. This warmth was surpassed only by the record anomaly of  $2.5^{\circ}\text{C}$  set in 1998 and by the anomaly of  $2.0^{\circ}\text{C}$  observed in 1981.

According to preliminary estimates, annual mean temperatures during 1999 for the contiguous United States averaged  $1.07^{\circ}\text{C}$  above the 1961–90 mean (Fig. 5b), making it the second warmest year since



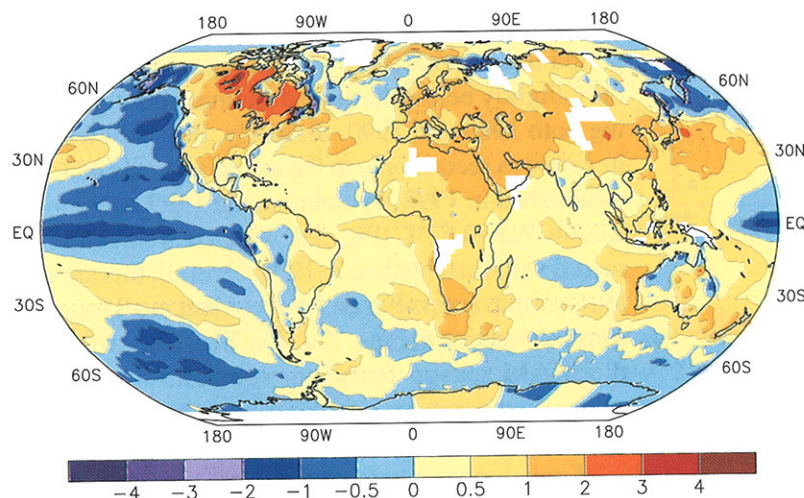


FIG. 3. Annual surface temperature anomalies ( $^{\circ}\text{C}$ ) for 1999. Analysis is based on station data over land and on SST data over the oceans. Anomalies are departures from the 1961–90 base period means. White areas are regions with insufficient data for analysis.

1900. This warmth was also surpassed only by the record anomaly of  $1.28^{\circ}\text{C}$  set in 1998.

This anomalous warmth across North America was particularly prominent during DJF, when temperatures were  $2^{\circ}$ – $4^{\circ}\text{C}$  above average from the U. S. Gulf Coast

to northern Canada (see section 6, Fig. 77a). Temperatures in the eastern two-thirds of Canada also remained  $2^{\circ}$ – $4^{\circ}\text{C}$  above average during MAM (see section 6, Fig. 79a) and were  $1^{\circ}$ – $2^{\circ}\text{C}$  above average during June–August (JJA) (see section 6, Fig. 81a). This anomalous warmth redeveloped across nearly all of North America during September–November (SON) (see section 6, Fig. 83) and was particularly evident in the United States during November when more than 70% of the country reported monthly mean temperatures in the top tenth percentile of the 1961–90 distribution (not shown).

A second extensive region of anomalous warmth extended across Europe, northern Africa, Russia, and much of Asia during 1999 (Fig. 3), with annual mean temperatures averaging more than  $1^{\circ}\text{C}$  above average in these regions. This anomalous warmth was associated with an anomalous upper-level anticyclonic circulation extending from the eastern Pacific eastward across the Atlantic Ocean to Asia throughout the year

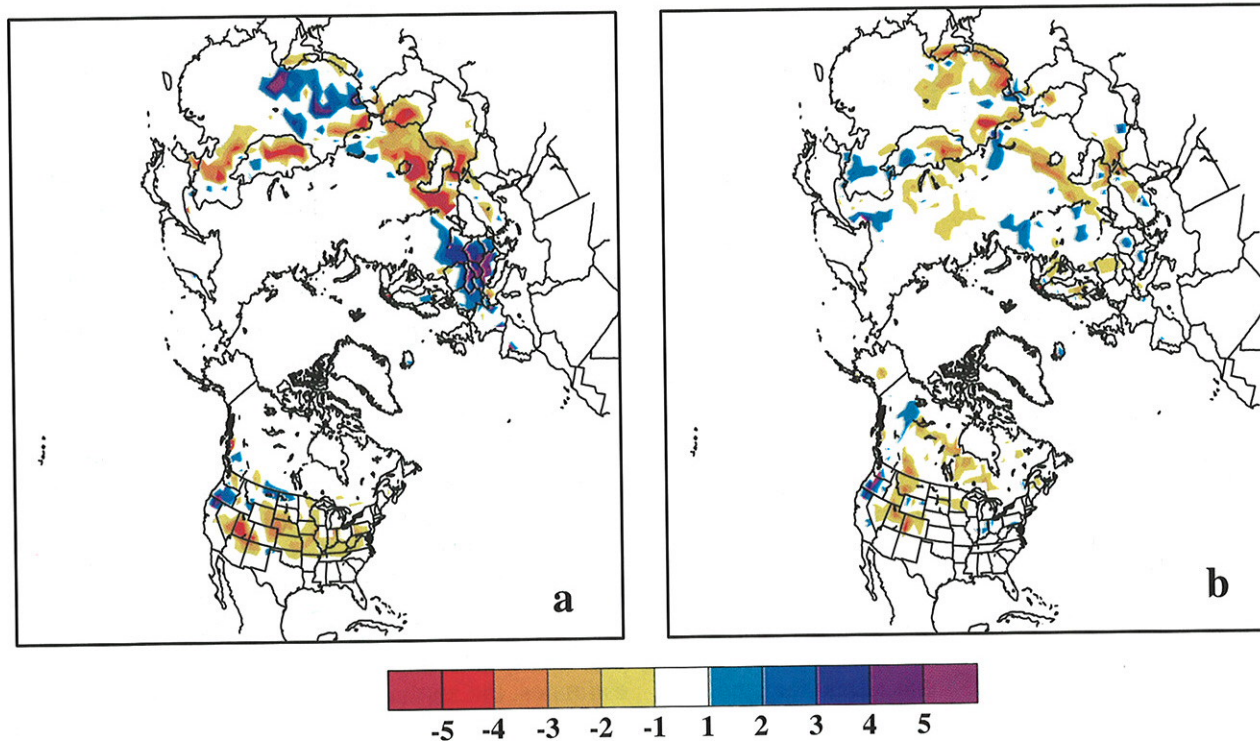


FIG. 4. Snow cover duration anomaly (weeks) during (a) Dec 1998–Feb 1999 and (b) Mar–May 1999. Values are derived from an operational analysis of visual satellite imagery by NOAA/NESDIS. Anomalies are departures from the 1972–98 base period means.



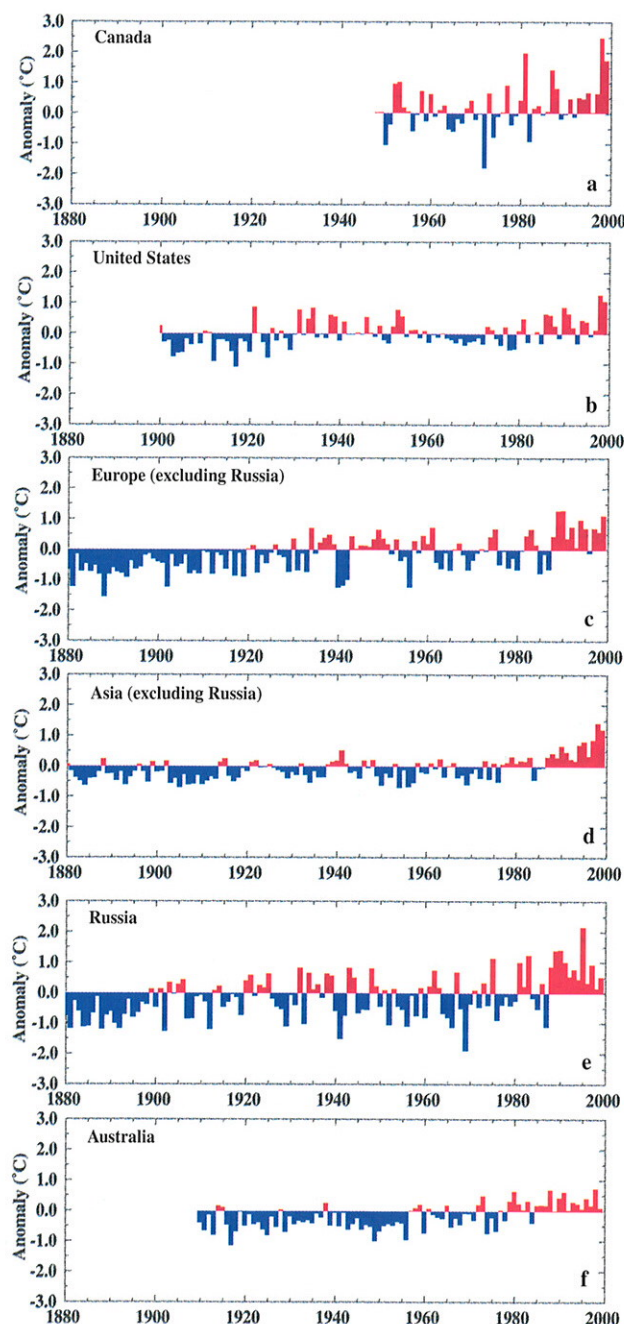


FIG. 5. Annual surface temperature anomalies ( $^{\circ}\text{C}$ ) for (a) Canada, (b) the contiguous United States, (c) Europe, (d) Asia, (e) Russia, and (f) Australia. Anomalies are departures from the 1961–90 base period means. [Source: (a) Environment Canada, (b–e) National Climatic Data Center, and (f) Australian Bureau of Meteorology.]

[see section 3e(2), Fig. 23]. It was also associated with a reduced southward extent of the snowpack during DJF and MAM (Fig. 4).

In Europe and Asia (excluding Russia), annual mean temperatures during 1999 averaged  $1.1^{\circ}\text{C}$

(Fig. 5c) and  $1.2^{\circ}\text{C}$  (Fig. 5d) above the 1961–90 base period mean, respectively. In Europe, this value was only slightly below the record anomaly observed during both 1989 and 1990. Similarly, the 1999 warmth in Asia was second only to the record anomaly of  $1.4^{\circ}\text{C}$  established in 1998. In contrast, the 1999 anomaly in Russia was  $+0.52^{\circ}\text{C}$  (Fig. 5e), which is well below the record value established in 1995. Overall, this anomalous warmth across Eurasia was evident in all four seasons (see section 6, Figs. 77a, 79a, 81a, 83a), with only the MAM season featuring substantially below-average temperatures over large portions of Russia and northeastern Asia (see section 6, Fig. 79a).

Annual mean temperatures were also above normal in Africa during 1999 (Fig. 3), with values of  $0.5^{\circ}\text{--}2^{\circ}\text{C}$  above average observed over much of the continent. In South Africa, this anomalous warmth was evident in all seasons (see section 6, Figs. 77a, 79a, 81a, 83a), while in northern Africa it was evident in all seasons except DJF.

In contrast to the near-record breaking temperatures observed over much of the Northern Hemisphere and Africa, annual mean temperatures in Australia during 1999 were only  $0.11^{\circ}\text{C}$  above the 1961–90 mean (Fig. 5f). This value is well below the record positive anomaly of  $+0.62^{\circ}\text{C}$  set in 1998. Regionally, annual mean temperatures in Australia averaged  $1^{\circ}\text{--}2^{\circ}\text{C}$  above normal in the interior regions, but were below average along the northwest coast and along the east coast near Brisbane.

Below-average temperatures also prevailed along the western interior of South America during 1999, in a band stretching southward from northern Brazil to northern Argentina (Fig. 3). Farther east, temperatures in the eastern half of the continent were only slightly warmer than normal during the year, with annual anomalies generally less than  $+1^{\circ}\text{C}$ .

### b. Troposphere

Global estimates of mean tropospheric temperatures are obtained from channel 2R of the Microwave Sounding Unit (MSU) (Spencer et al. 1990; Spencer and Christy 1992) on the National Oceanographic and Atmospheric Administration (NOAA) series of polar-orbiting satellites. The peak in the channel 2R weighting function is near 750 hPa. According to the MSU estimates, the annual mean global tropospheric temperature during 1999 was  $0.06^{\circ}\text{C}$  below the 1979–98 base period mean (Fig. 6), which is in stark contrast to the record positive anomaly of  $+0.46^{\circ}\text{C}$  observed in 1998. Since the beginning of MSU measurements



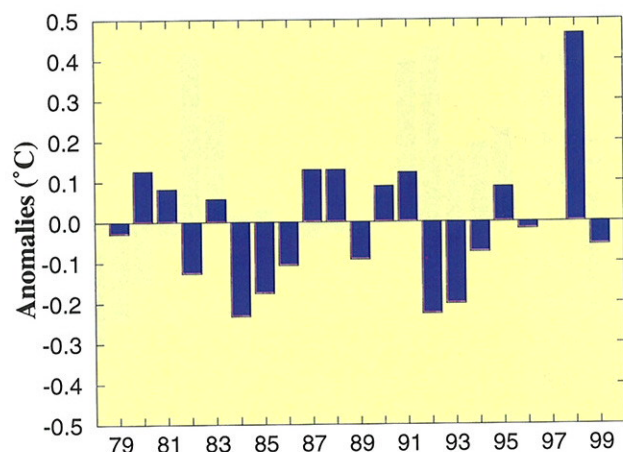


FIG. 6. Annual global-tropospheric temperature anomalies ( $^{\circ}\text{C}$ ) derived from the MSU channel 2R. Anomalies are departures from the 1979–98 base period means. (Data provided by the University of Alabama in Huntsville.)

in 1979, there has been little evidence of a trend in lower-tropospheric temperatures. This contrasts with a pronounced upward trend in surface air temperatures over the past 20 years (Fig. 1a), but according to the National Research Council (2000) “in no way invalidates the conclusion that surface temperature has been rising.”

The record decrease in mean tropospheric temperatures of approximately  $0.5^{\circ}\text{C}$  between 1998 and 1999 was linked to below-average temperatures throughout the global Tropics and subtropics [ $25^{\circ}\text{S}$ – $25^{\circ}\text{N}$ , Fig. 7], with the largest negative anomalies in this latitude band located over the central and eastern Pacific throughout the year (Figs. 8a,b). These anomalies reflected below-average SSTs and suppressed convection across the eastern half of the equatorial Pacific in association with La Niña conditions (see sections 3c, 3d; Figs. 16, 17), as well as the La Niña-related subtropical cyclonic circulation anomalies observed at upper levels that flanked the region of suppressed tropical convection.

In the Northern Hemisphere, a notable feature during 1999 was above-average temperatures in the middle latitudes centered near  $40^{\circ}\text{N}$ , which is also evident in the mean surface temperature anomalies (Fig. 3). These anomalies, together with the cooler-than-normal temperatures in the Tropics, reflected a decreased strength of the normal north–south temperature gradient near  $30^{\circ}\text{N}$ . An anomalously weak meridional temperature gradient was also evident in the Southern Hemisphere over the South Pacific near ( $30^{\circ}\text{S}$ ) throughout the year. In both hemispheres, this

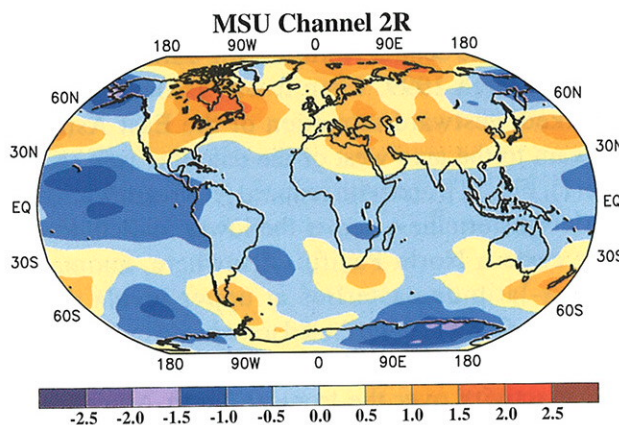


FIG. 7. Annual tropospheric temperature anomalies ( $^{\circ}\text{C}$ ) during 1999, derived from channel 2R of the MSU. Anomalies are departures from the 1979–98 base period means. (Data provided by the University of Alabama in Huntsville.)

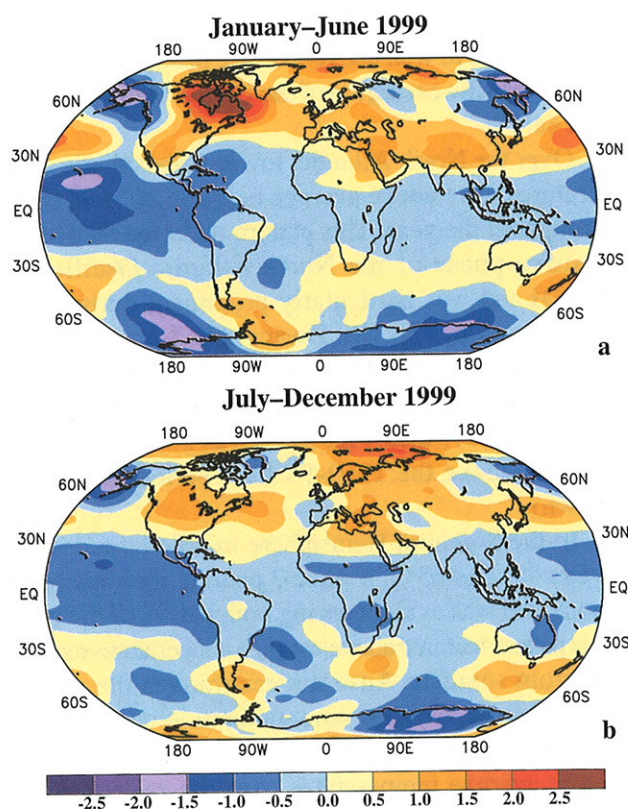


FIG. 8. Mean tropospheric temperature anomalies ( $^{\circ}\text{C}$ ) for (a) Jan–Jun 1999 and (b) Jul–Dec 1999 derived from the MSU channel 2R. Anomalies are departures from the 1979–98 base period means. (Data provided by the University of Alabama in Huntsville.)

reduced temperature gradient coincided with a large-scale pattern of anomalous easterly winds in the upper troposphere [see section 3e(1), Fig. 17].



This overall anomaly pattern was especially prominent over the central North Pacific during December 1998–March 1999, when it was associated with a marked westward retraction of the East Asian jet stream to the area west of the date line [see section 3e(1), Fig. 21], and with reduced jet stream winds and reduced storminess across the lower midlatitudes of the eastern North Pacific. Elsewhere, anomalous lower-latitude easterlies at upper levels during August–October contributed to reduced hurricane activity over the eastern Pacific and to enhanced hurricane activity over the tropical North Atlantic [see section 4a(2)(i)]. In contrast, an increased meridional temperature gradient was evident in the Northern Hemisphere between 40° and 55°N, which is consistent with increased westerlies in this latitude band during much of the year. During the winter season, these enhanced westerlies contributed to exceptionally warm temperatures over large portions of North America and to well above-average precipitation in the Pacific Northwest region of the United States [see section 4a(1)].

Over the North Atlantic, lower-tropospheric temperatures were above average between 30° and 60°N throughout the year. This pattern reflected an overall positive phase of the North Atlantic Oscillation (NAO) and was particularly prominent during DJF (see section 6, Fig. 78). During this 3-month period the standardized NAO index, determined from a rotated EOF analysis of 700-hPa heights (see Halpert and Bell 1997, their Fig. 31a), was 2.0 standard deviations above the 1950–99 base period mean (not shown).

In the Southern Hemisphere middle latitudes between 40° and 65°S, a wave-3 pattern of temperature anomalies was evident during both halves of the year. This pattern featured above-average temperatures extending from southern Australia eastward to the central South Pacific, over extreme southern South America, and in the region just poleward of South Africa, and below-average temperatures over the eastern South Pacific, the central South Atlantic, and the Indian Ocean. Over the Pacific sector, this anomaly pattern was very similar to its Northern Hemisphere counterpart, indicating a considerable interhemispheric symmetry of the anomalies in this region. Over the high latitudes of the eastern South Pacific, this anomaly pattern was associated with reduced blocking activity during much of the year and with increased westerlies and periods of increased storminess across southern South America (see section 4d, Fig. 55).

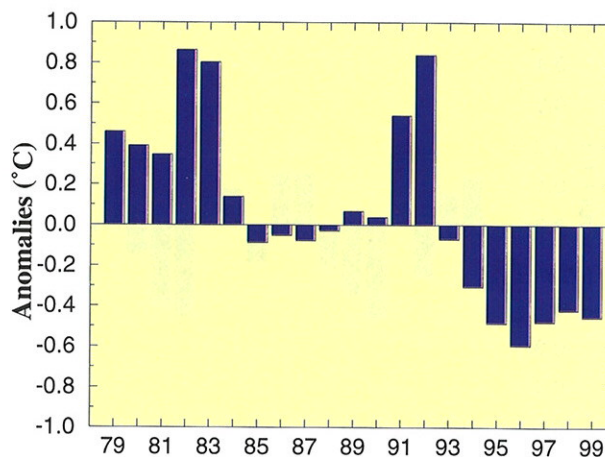


FIG. 9. Annual global-stratospheric temperature anomalies (°C) derived from the MSU channel 4. Anomalies are departures from the 1979–98 base period means. (Data provided by the University of Alabama in Huntsville.)

### c. Lower stratosphere

Global estimates of lower-stratospheric temperatures are derived from channel 4 of the MSU. The peak in the channel 4 weighting function varies from 70 hPa at extreme scan position to 100 hPa at nadir. During 1999, the estimated global mean temperature in the lower stratosphere was 0.45°C below the 1979–98 base period mean (Fig. 9), which is the fourth lowest value in the 21-yr record. The overall character of the time series has been dominated by major volcanic eruptions (i.e., El Chichon in 1982 and Mount Pinatubo in 1991), with an increase in temperatures observed immediately after these eruptions, followed by a rapid decrease in temperatures over the next several years. For the past seven years global lower-stratospheric temperatures have been below the long-term mean, although they have increased slightly during the past few years from the record low values observed in 1996.

Regionally, lower stratospheric temperatures were above average throughout the global Tropics during 1999 (Fig. 10), with the largest positive anomalies observed over the eastern half of the tropical Pacific Ocean in association with La Niña conditions. These positive anomalies were associated with a lowered tropopause and a cooler-than-normal troposphere (Fig. 8), in response to the La Niña–related suppressed convection and the accompanying subtropical cyclonic circulation anomalies flanking the region of suppressed convection in both hemispheres. An anomalously warm lower stratosphere was also evident elsewhere in the global Tropics throughout the year



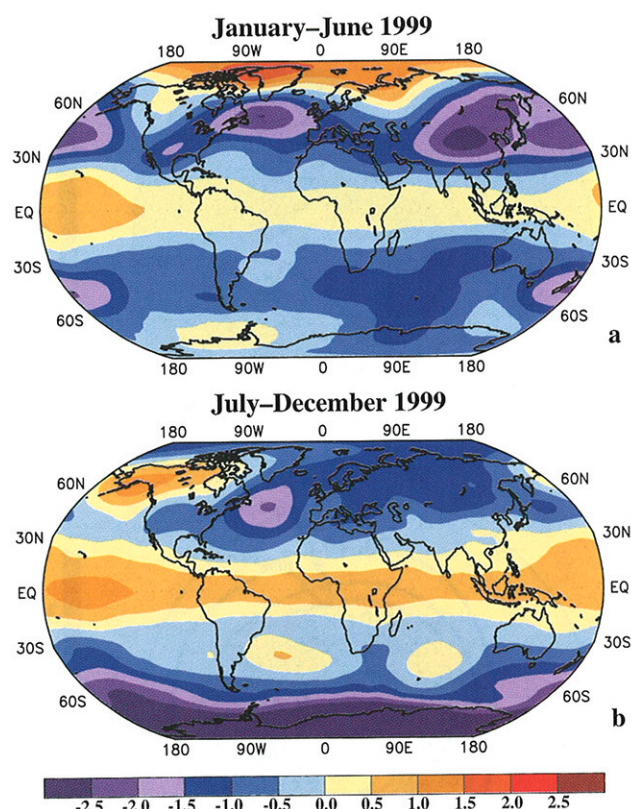


FIG. 10. Mean stratospheric temperature anomalies ( $^{\circ}\text{C}$ ) for (a) Jan–Jun 1999 and (b) Jul–Dec 1999 derived from the MSU channel 4. Anomalies are departures from the 1979–98 base period means. (Data provided by the University of Alabama in Huntsville.)

and contrasts with the anomalously cool tropical stratosphere that accompanies a major El Niño episode (see Bell and Halpert 1999, their Fig. 10a).

In the middle latitudes, lower-stratospheric temperatures were generally below average in both hemispheres during 1999 (Fig. 10), with the largest negative anomalies observed over the North Pacific, the North Atlantic, and eastern Asia. In each of these areas, the anomalies were accompanied by above-average tropospheric temperatures (Fig. 7) and above-average upper-tropospheric heights (see section 6, Figs. 78, 80, 82, 84). A reduced north–south slope of the tropopause and reduced jet stream winds existed in the area equatorward of all of these anomalies [see section 3e(1), Fig. 17], while an increased slope of the tropopause and enhanced westerly winds existed in the area poleward of these anomalies.

Lower-stratospheric temperatures have generally been below average in the middle latitudes of both hemispheres since early 1998 (Figs. 11a, 12a), with record negative anomalies observed in late 1998–early

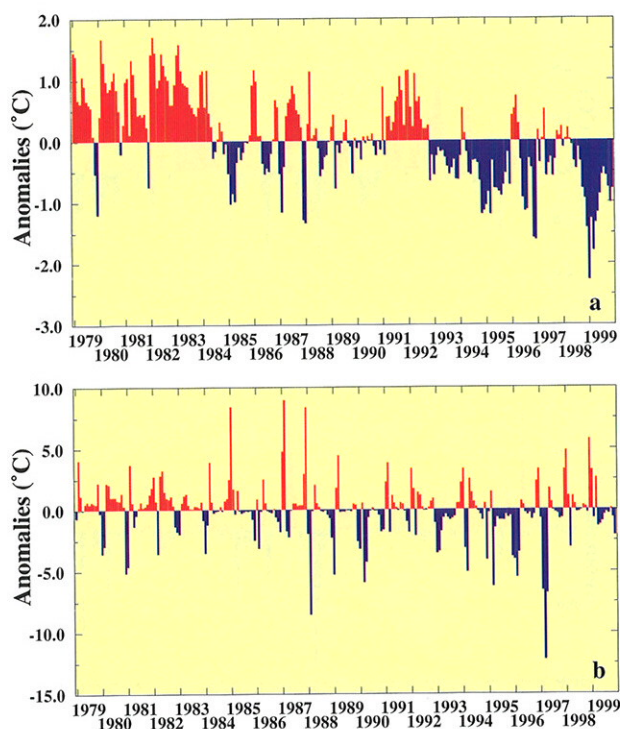


FIG. 11. Monthly Northern Hemisphere lower-stratospheric temperature anomalies ( $^{\circ}\text{C}$ ) for (a) the midlatitudes ( $30^{\circ}$ – $60^{\circ}\text{N}$ ) and (b) the polar region ( $60^{\circ}$ – $90^{\circ}\text{N}$ ) derived from the MSU channel 4. Anomalies are departures from the 1979–98 base period means. (Data provided by the University of Alabama in Huntsville.)

1999. In the Northern Hemisphere, this cooling contrasts with the near-normal to above-normal temperatures observed during the previous three winters. At higher latitudes, above-normal temperatures were observed in the lower stratosphere of the Northern Hemisphere polar region ( $60^{\circ}$ – $90^{\circ}\text{N}$ ) during the first half of the year (Fig. 10a), primarily in response to significant warming during DJF (Fig. 11b). This is the second consecutive winter with well-above-normal temperatures in this region, following a string of five consecutive winters with colder-than-normal temperatures (Fig. 11b).

Lower-stratospheric temperatures were significantly cooler than average over Antarctica during the second half of 1999 (Fig. 10b), with near-record low values evident during November 1999 (Fig. 12b). For the past five years, October–November temperatures have been below average across Antarctica, which has favored the persistence of polar stratospheric clouds that act to deplete Antarctic ozone [see section 5a(2)].

During October–November 1999 the anomalously low stratospheric temperatures were associated with below normal geopotential heights at 50 hPa every-



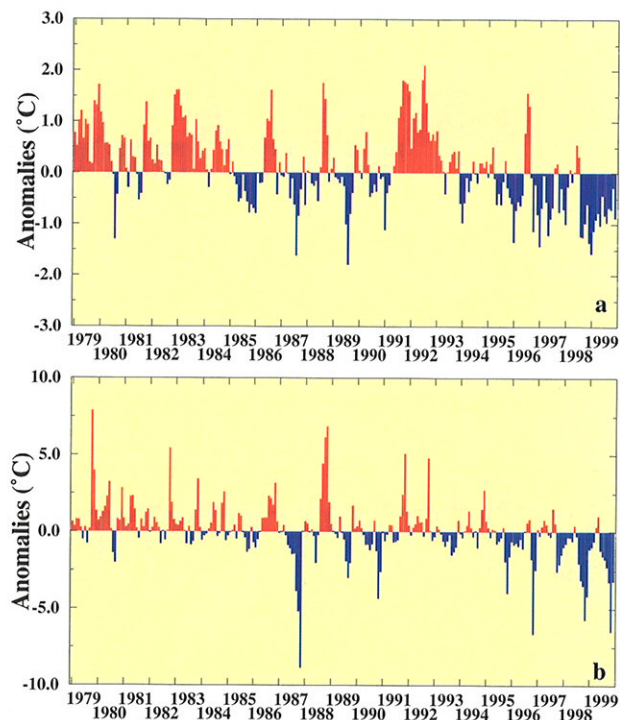


FIG. 12. Monthly Southern Hemisphere lower-stratospheric temperature anomalies ( $^{\circ}\text{C}$ ) for (a) the midlatitudes ( $30^{\circ}$ – $60^{\circ}\text{S}$ ) and (b) the polar region ( $60^{\circ}$ – $90^{\circ}\text{S}$ ) derived from the MSU channel 4. Anomalies are departures from the 1979–98 base period means. (Data provided by the University of Alabama in Huntsville.)

where poleward of  $60^{\circ}\text{S}$  (Fig. 13a). The largest anomalies were centered directly over the polar region, where heights averaged more than 300 m below normal and temperatures averaged more than  $6^{\circ}\text{C}$  below normal. Collectively, these conditions were associated with an exceptionally strong gradient in the geopotential height field between  $60^{\circ}$  and  $80^{\circ}\text{S}$  (Fig. 13b). This height field reflected an enhanced polar vortex and was accompanied by an enhanced subpolar jet stream which extended around the entire hemisphere with average zonal wind speeds exceeding  $30\text{ m s}^{-1}$ . These conditions reflect the positive phase of the Antarctic Oscillation (e.g., Thompson and Wallace 2000), and contrast with the weaker height gradient and weaker zonal wind maximum that characterize the climatological mean polar vortex (Fig. 13c).

### 3. The 1998–2000 Pacific cold episode (La Niña)

#### a. Overview

The global climate during most of 1999 was impacted by moderate-to-strong cold episode (La Niña)

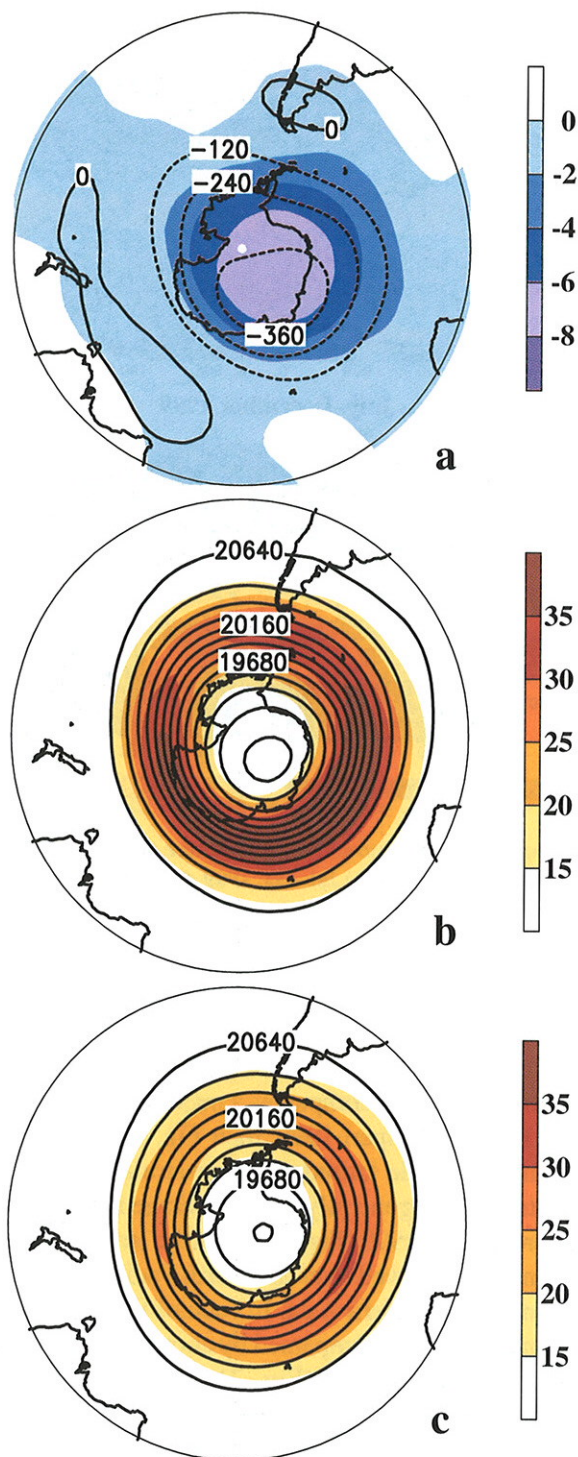


FIG. 13. Oct–Dec 1999 Southern Hemisphere (a) stratospheric temperature anomalies (shaded,  $^{\circ}\text{C}$ ) derived from the MSU channel 4 and 50-hPa height anomalies (contours, m), (b) 50-hPa height (contours, m) and zonal wind speed (shaded,  $\text{m s}^{-1}$ ), and (c) mean October–December 50-hPa height (contours, m) and zonal wind speed (shaded,  $\text{m s}^{-1}$ ). Contour interval for height and height anomalies is 120 m. Negative height anomalies in (a) are indicated by dashed contours. Anomalies are departures from the 1979–98 base period means. (MSU data provided by the University of Alabama in Huntsville.)



conditions in the tropical Pacific (Fig. 14). The evolution toward the 1998–2000 cold episode began in early 1998 as the oceanic thermocline (approximated by the depth of the 20°C isotherm) became shallower than normal across the central and eastern equatorial Pacific (Fig. 14a). Accompanying this evolution, subsurface temperatures dropped and the volume of anomalously warm water decreased across the central and eastern equatorial Pacific. Nonetheless, SSTs remained well above average across the eastern half of the equatorial Pacific in association with ongoing very strong El Niño conditions (Fig. 14c). These conditions set the stage for a rapid transition to below-normal SSTs during the first week in May. This transition was triggered by a dramatic return to near-normal easterly winds at lower levels (Fig. 14b), which contributed to enhanced oceanic upwelling that brought cold ocean waters to the surface.

The La Niña episode then became well established by July 1998 and continued to strengthen during September–November 1998 as SSTs dropped to more than 2°C below normal across large portions of the central and eastern Pacific (Fig. 14c). This combination of below-normal SSTs and an anomalously shallow thermocline across the central and eastern Pacific reflected increased oceanic upwelling in association with the establishment of enhanced low-level equatorial easterly winds across the central and east-central equatorial Pacific (Fig. 14b).

Accompanying this evolution, tropical convection became enhanced throughout Indonesia and the western Pacific, and suppressed [indicated by positive anomalies of outgoing longwave radiation (OLR)] across the central and eastern equatorial Pacific (Fig. 14d). The associated reduction in atmospheric heating between 160°E and the west coast of South America led to a drop in 200-hPa heights throughout that region (Fig. 14e) and to cyclonic circulation anomalies at upper levels that flanked the region of suppressed tropical convection. These cold episode conditions then persisted throughout 1999 and into the year 2000, and significantly impacted global temperature, precipitation, and atmospheric circulation patterns in a manner consistent with past cold episodes (Ropelewski and Halpert 1989; Halpert and Ropelewski 1992).

#### b. Precipitation impacts

Many areas of the world experienced precipitation patterns during 1999 that were consistent with past cold episodes (Fig. 15). Among the areas most impacted by La Niña-related precipitation anomalies

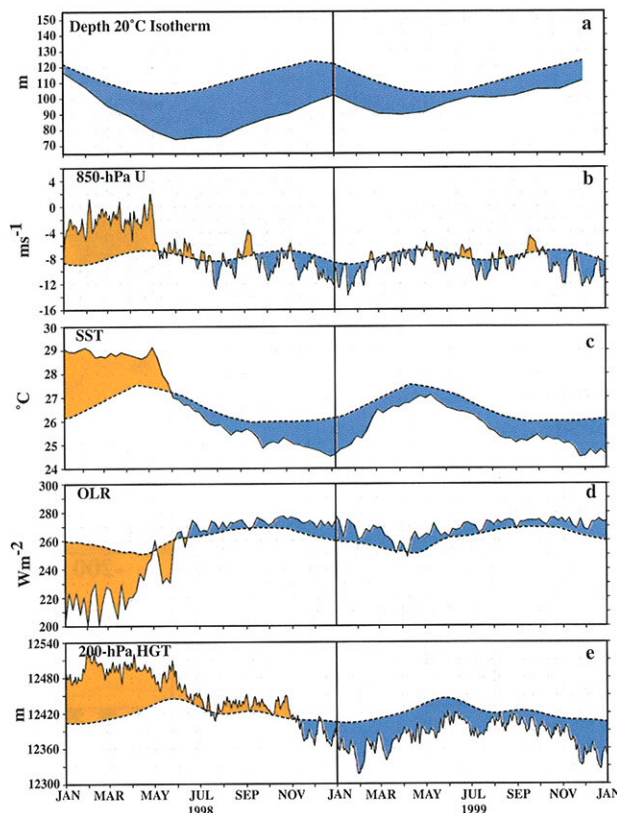


FIG. 14. Monthly time series of (a) the depth of the 20°C isotherm (m), (b) 850-hPa zonal wind speed ( $\text{m s}^{-1}$ ), (c) sea surface temperature (SST,  $^{\circ}\text{C}$ ), (d) outgoing longwave radiation (OLR,  $\text{W m}^{-2}$ ), and (e) 200-hPa height (m). Values in (a)–(d) are determined by averaging over the region bounded by 5°N–5°S and 180°–100°W; in (e) over the region 20°N–20°S and 180°–100°W. The solid curve in all panels shows the monthly mean values and the dashed curve shows the climatological mean. The anomalies are shown shaded, with orange (blue) shading indicating positive (negative) anomalies, except for (d) where the shading convention is reversed. The climatology and anomalies are computed with respect to the 1979–95 base period.

were Indonesia, the tropical Indian Ocean, the western tropical Pacific, and the western and central subtropical South Pacific, all of which experienced well above-average rainfall throughout the year. The cold episode also featured a nearly complete disappearance of tropical rainfall from the central and eastern equatorial Pacific.

Continuing eastward, the Caribbean Sea and tropical Atlantic experienced above-normal rainfall during much of the year, along with an extremely active Atlantic hurricane season from mid-August through November [see section 4a(2)]. Above-normal rainfall was also observed across the Sahel region of northwestern Africa during July–September [see section 4b(2)]. In the extratropics, La Niña conditions contrib-



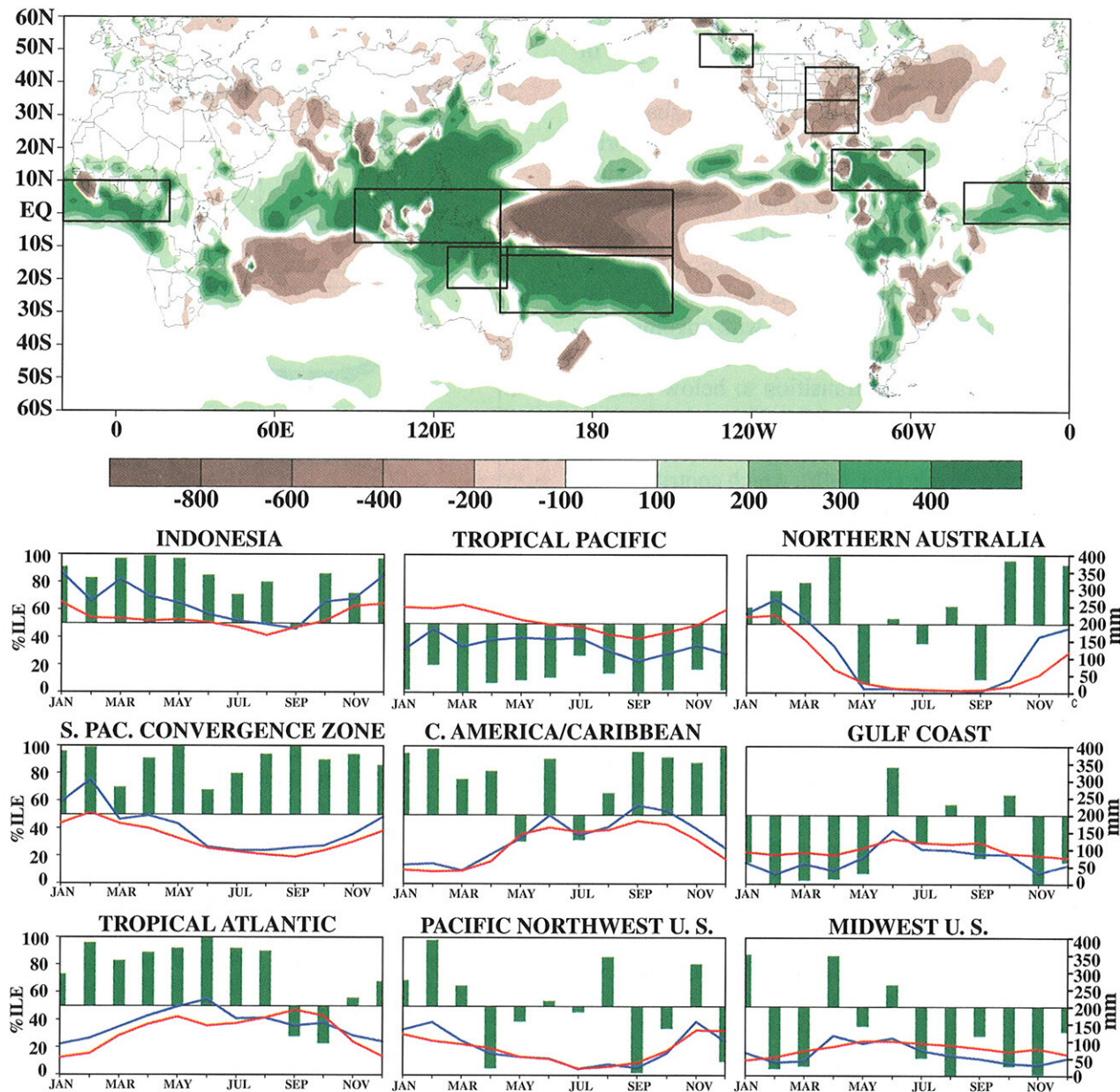


FIG. 15. Jan–Dec 1999 accumulated precipitation anomaly (top) and regional area-averaged estimates of monthly mean precipitation amounts (mm, blue lines) and precipitation percentiles (% bars) during 1999 for the six boxed regions shown in top panel. The monthly precipitation climatology (mm, dashed, red lines) is the 1979–95 base period monthly means. The percentiles are labeled on the left-hand vertical axis and totals are labeled on the right-hand vertical axis. Precipitation amounts are obtained by merging raingauge observations and satellite-derived precipitation estimates (Janowiak and Xie 1999).

uted to above-normal wintertime precipitation in southwestern Canada and the Pacific Northwest United States [see section 4a(1)], and to suppressed cool-season precipitation across the southeastern United States and Gulf Coast states.

#### c. SSTs and subsurface ocean structure

Over the equatorial Pacific the La Niña-related pattern of SSTs was characterized by a well-defined

cold tongue extending westward from the west coast of South America to the vicinity of the date line (Figs. 16a,c,e,g). This cold tongue extended farther west than normal throughout the year, as indicated by a westward retreat of the 28°C isotherm to near 160°E. Temperatures within this cold tongue averaged less than 25°C during most of the year, with the exception of MAM (Fig. 16c) when they approached 26°C in association with the normal peak in the annual cycle.



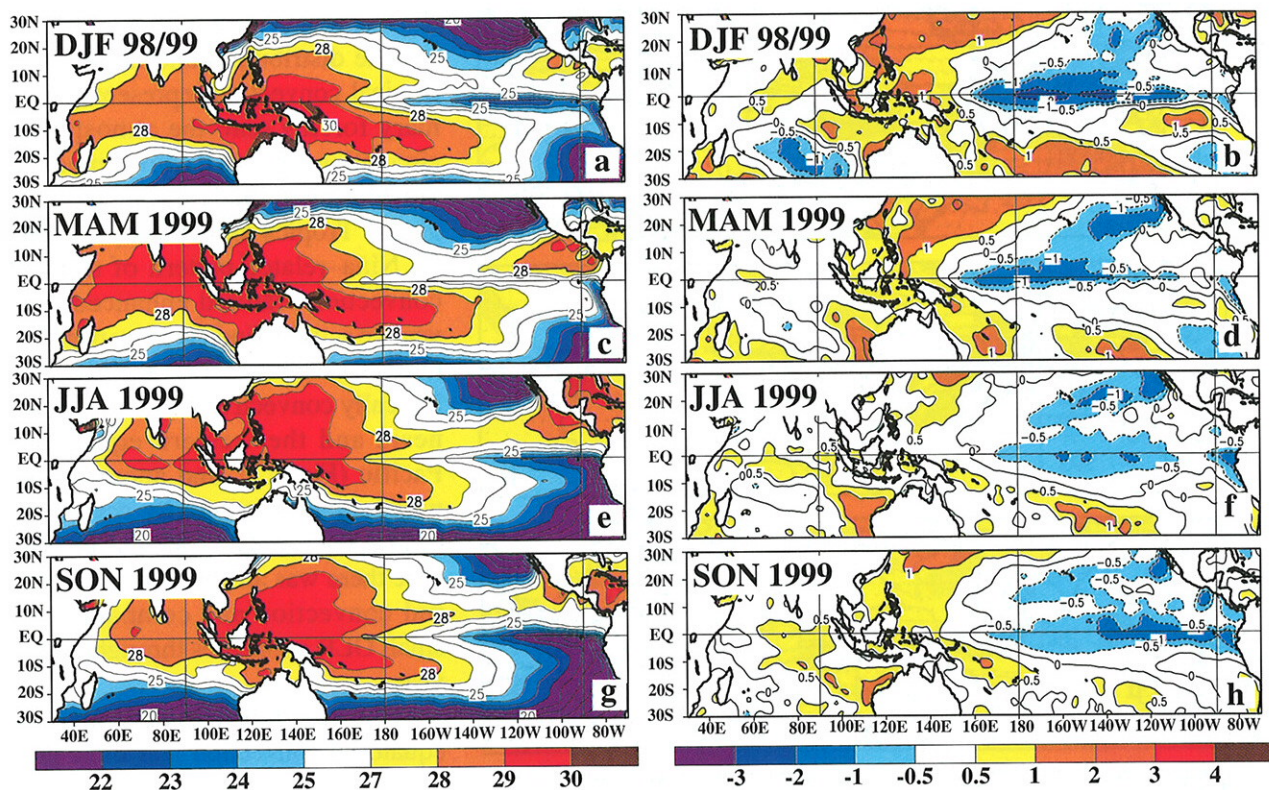


FIG. 16. Seasonal SST (left) and anomaly (right) for (a, b) DJF 1998/99, (c, d) MAM 1999, (e, f) JJA 1999, and (g, h) SON 1999. Contour interval is  $1^{\circ}\text{C}$ , with the  $0.5^{\circ}\text{C}$  anomaly contour included. Anomalies are departures from the 1961–90 adjusted Optimal Interpolation (OI) climatology (Smith and Reynolds 1998).

These temperatures were well below the  $28^{\circ}\text{C}$  value generally considered to be the approximate threshold for deep tropical convection (Gadgil et al. 1984) and were consistent with the disappearance of deep tropical convection from this region throughout the year (Fig. 17).

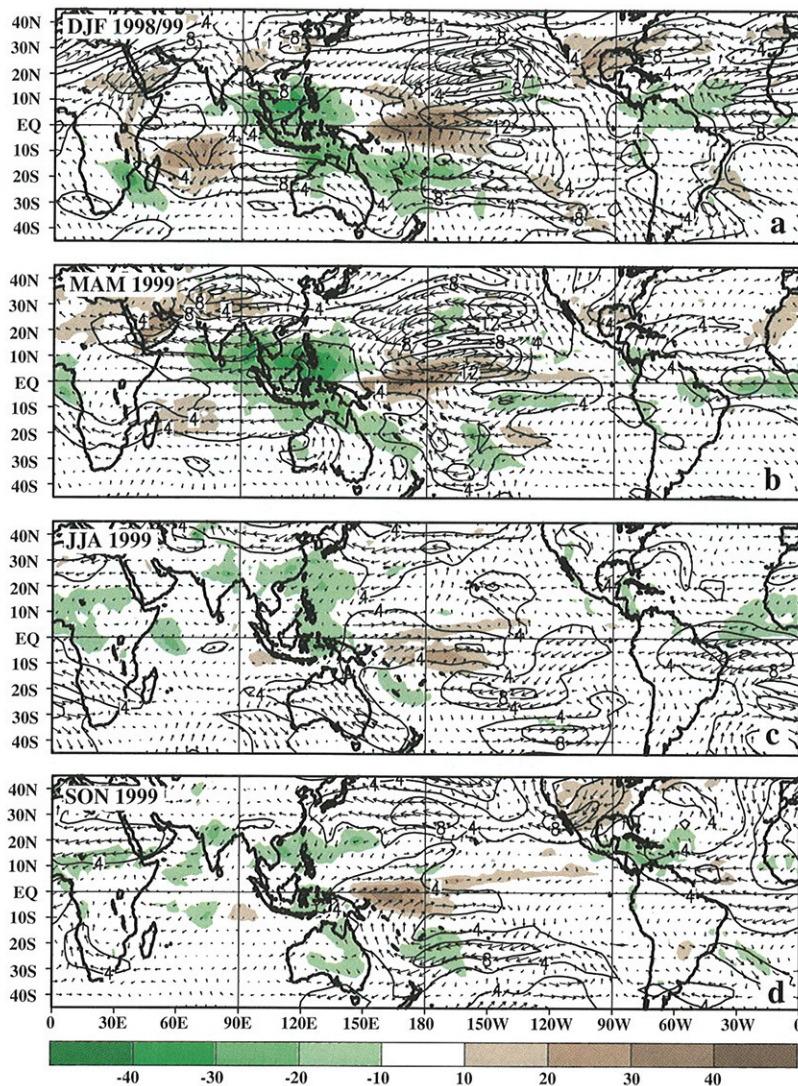
The cold episode and anomalous westward extension of the equatorial cold tongue are further highlighted by the pattern of negative SST anomalies across the central and eastern Pacific. SSTs averaged more than  $0.5^{\circ}\text{C}$  below normal across the entire eastern half of the tropical Pacific throughout the year (Figs. 16b,d,f,h), with the most significant negative anomalies occurring during DJF and MAM when temperatures dropped to  $1^{\circ}\text{--}2^{\circ}\text{C}$  below average (Figs. 16b,d). These conditions were accompanied by anomalously warm SSTs over the western tropical Pacific during most of the year, with the largest positive SST anomalies (averaging  $0.5^{\circ}\text{--}1.0^{\circ}\text{C}$ ) also observed during DJF and MAM.

The SST anomaly fields also indicate that the cold episode weakened during JJA and subsequently strengthened during SON. By December 1999, mod-

erately strong cold episode conditions had reappeared, with SSTs averaging more than  $1^{\circ}\text{C}$  below normal across the entire central and eastern equatorial Pacific (*Climate Diagnostics Bulletin*, December 1999, their Fig. T18).

An examination of the subsurface thermal structure indicates that the anomalously cold ocean temperatures extended down to approximately 150 m depth across the central and eastern equatorial Pacific (Fig. 18), while anomalously warm ocean temperatures were evident over the western Pacific between approximately 50 and 225 m depth. These subsurface temperature anomalies reflected an increased slope of the oceanic thermocline and resulted from the characteristic La Niña-related pattern of strong oceanic upwelling over the eastern half of the Pacific and increased downwelling over the western Pacific. The weakening of the cold episode during JJA, and subsequent strengthening during SON, is also evident in the pattern of subsurface temperature anomalies in the eastern equatorial Pacific, which indicates only modest negative anomalies during JJA (Fig. 18c), followed by a substantial expansion of the region of below-normal temperatures during SON (Fig. 18d).





#### d. Tropical convection

The distribution and intensity of tropical convection represents a primary forcing onto the atmospheric circulation through its direct modulation of the wind and mass fields in the global Tropics and subtropics. The La Niña-related pattern of tropical convection featured enhanced convective activity (indicated by negative OLR anomalies) across the climatologically convective regions of Indonesia and the western equatorial Pacific (Fig. 17), and anomalously weak convective activity across the central Pacific. Over the eastern Pacific there was an absence of equatorial convection and comparatively small OLR anomalies throughout the year.

This overall pattern of anomalous equatorial convection was most pro-

FIG. 17. Outgoing longwave radiation (OLR) anomalies (shaded) and 200-hPa vector wind anomalies and isotachs for (a) DJF 1998/99, (b) MAM 1999, (c) JJA 1999, and (d) SON 1999. Contour interval for isotachs is  $4 \text{ m s}^{-1}$ . Shading interval for OLR anomalies is  $10 \text{ W m}^{-2}$ . Anomalies are departures from the 1979–95 base period monthly means.

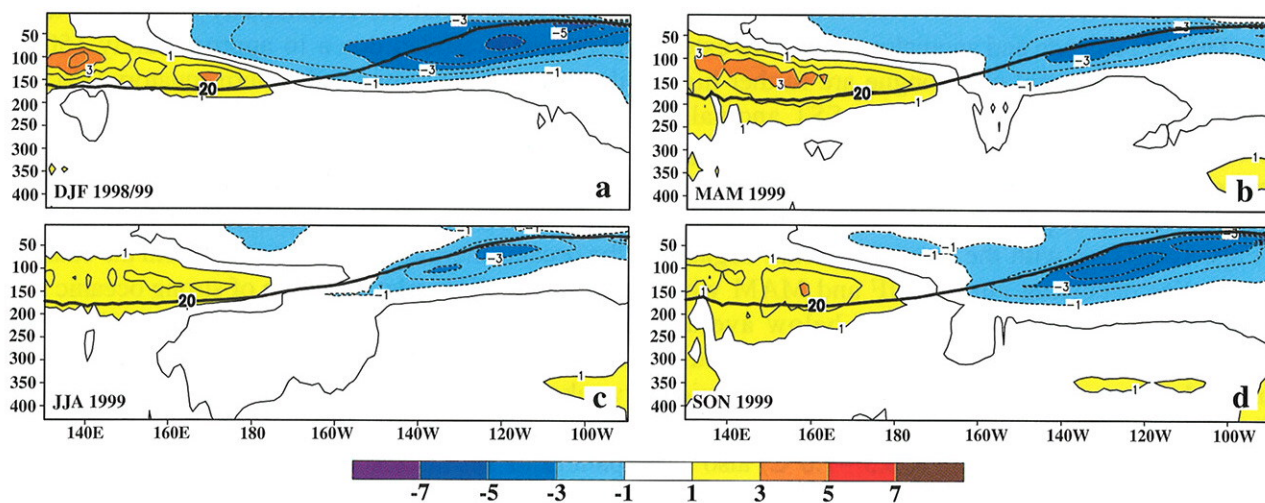


FIG. 18. Equatorial depth–longitude section of ocean temperature anomalies for (a) DJF 1998/99, (b) MAM 1999, (c) JJA 1999, and (d) SON 1999. Contour interval is  $1^\circ\text{C}$ . The dark line is the  $20^\circ\text{C}$  isotherm. Data are derived from an analysis system that assimilates oceanic observations into an oceanic GCM (Behringer et al. 1998). Anomalies are departures from the 1983–92 base period means.



nounced during DJF and MAM, but remained prominent even during JJA and SON. These conditions were accompanied by enhanced convection over large portions of Central America and the western Caribbean Sea throughout the year, as well as across the African Sahel during the June–September rainy season in that region [see section 4b(2)].

#### e. Atmospheric circulation

##### 1) PACIFIC BASIN

Several atmospheric circulation features common to past Pacific cold episodes prevailed during 1999. In the Tropics, these features included 1) upper-level westerly wind anomalies across the central and eastern Pacific during DJF and MAM (Figs. 17a,b) and over the western half of the tropical Pacific during JJA and SON (Figs. 17c,d), 2) lower-level easterly wind anomalies across the central and western Pacific throughout the year (Fig. 19), 3) enhanced ascending motion and convective activity over the western Pacific and Indonesia, and 4) anomalous descending motion and suppressed convective activity over the central Pacific. These conditions are consistent with an enhanced equatorial Walker circulation across the Pacific basin, which is a well-known feature of Pacific cold episodes.

The circulation also featured anomalous upper-level equatorward flow over the central tropical Pacific in all seasons (Fig. 17), along with a combination of anomalous upper-level convergence and lower-level divergence in that region (implied by the anomalous OLR pattern in Fig. 17). These conditions were accompanied by a suppressed Hadley circulation over the central tropical Pacific, another well-known feature of Pacific cold episodes.

The La Niña–related tropical convection also contributed to coherent anomaly patterns in the atmospheric mass and wind fields in the subtropics and extratropics of both hemispheres. In particular, the absence of convective activity over the central and eastern Pacific led to cooler-than-normal mean tropo-

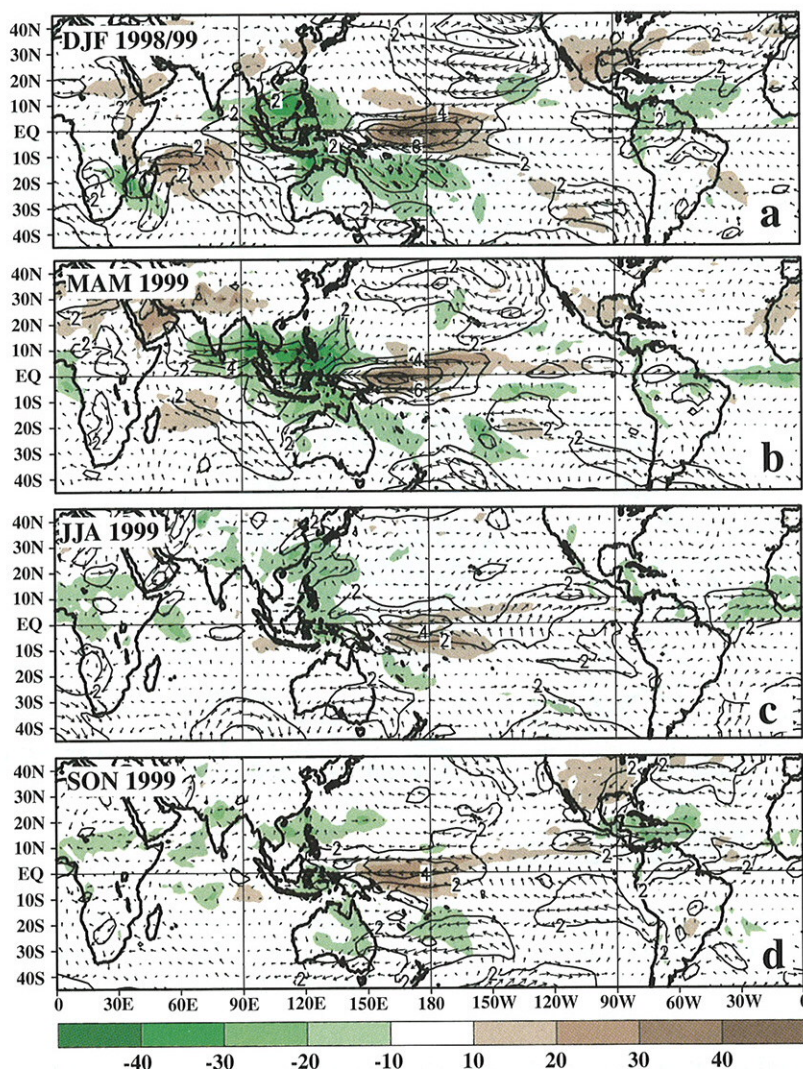


FIG. 19. Outgoing longwave radiation (OLR) anomalies (shaded) and 850-hPa vector wind anomalies and isotachs for (a) DJF 1998/99, (b) MAM 1999, (c) JJA 1999, and (d) SON 1999. Contour interval for isotachs is  $2 \text{ m s}^{-1}$ . Shading interval for OLR anomalies is  $10 \text{ W m}^{-2}$ . Anomalies are departures from the 1979–95 base period monthly means.

spheric temperatures (Fig. 7) and to decreased upper-level heights in those regions in all seasons (Figs. 14e, 20a). These conditions were accompanied by an amplification of the mid-Pacific troughs in both hemispheres, and by a confinement of the low-latitude ridges to the heavy convection region of the western Pacific and Australasia (Fig. 20). These circulation features were particularly pronounced during DJF (Fig. 20b), when the strong east–west variations in tropical convective activity were also manifested in enhanced east–west variations in the upper-level heights across the low latitudes of the Pacific basin.

In the Northern Hemisphere, this anomalous low-latitude height field during DJF impacted the structure



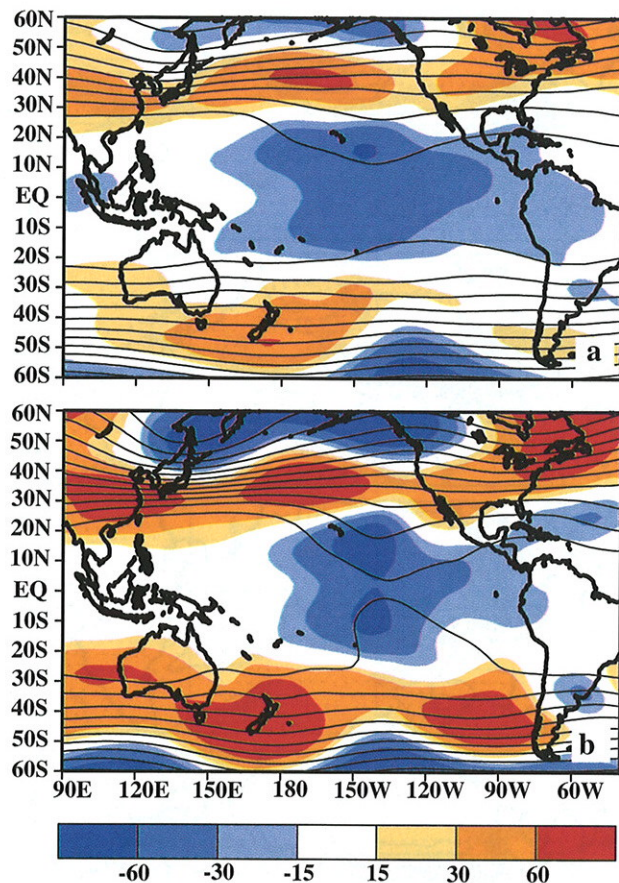


FIG. 20. 200-hPa height (contours, m) and anomalies (shaded) during (a) 1999 and (b) December 1998–February 1999. Anomalies are departures from the 1979–95 base period means.

and location of the East Asian jet stream (Fig. 21), as well as the extratropical atmospheric circulation over the higher latitudes of the North Pacific. In particular, the confinement of the low-latitude ridge to the western Pacific (Fig. 20b) contributed to a more northward position of the East Asian jet in the area west of the date line (Fig. 21), with the jet axis located near  $32.5^{\circ}\text{N}$  in the region of strong north–south height and temperature contrast along the poleward flank of the ridge. Farther east, the amplified mid-Pacific trough was associated with a decrease in the magnitude of both the upper-level height gradient (implied by the anomaly pattern in Fig. 20b) and jet stream winds (Fig. 21) across the eastern Pacific up to  $30^{\circ}\text{N}$  [indicated by easterly wind anomalies (blue shading) in the jet exit region (Fig. 21)].

This anomalous low-latitude height field also contributed to enhanced upper-level diffuence over the central Pacific along the equatorward flank of the East Asian jet exit region. In turn, this enhanced diffuence favored an amplification of the thermally indirect

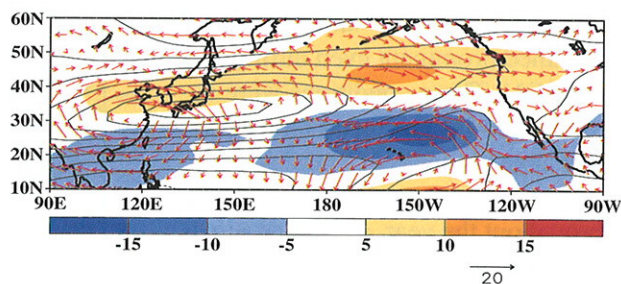


FIG. 21. 200-hPa zonal wind (contours, interval is  $10 \text{ m s}^{-1}$ ) and anomalies (shaded) during December 1998–February 1999. Seasonal vector wind anomalies are also shown. Anomalies are departures from the 1979–95 base period means.

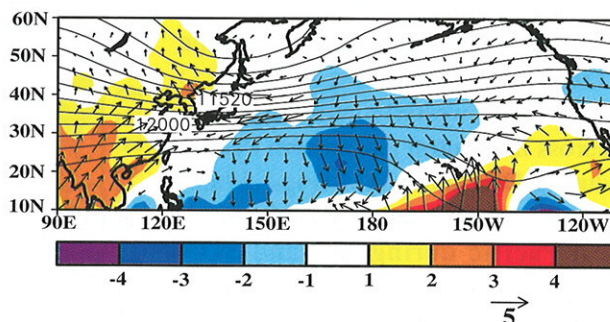


FIG. 22. December 1998–February 1999 200-hPa heights (contours, interval is 120 m), anomalous ageostrophic wind vector, and the meridional component of the anomalous ageostrophic wind (shaded,  $\text{m s}^{-1}$ ). Anomalies are departures from the 1979–95 base period.

transverse ageostrophic circulation normally found throughout the jet exit region, as indicated by anomalous upper-level ageostrophic flow directed equatorward toward higher heights (Fig. 22). This enhanced ageostrophic circulation is consistent with accentuated along-stream speed decreases that air parcels experienced as they exited the jet core and decelerated to below-normal wind speeds in the region south of  $30^{\circ}\text{N}$ .

This anomalous ageostrophic flow in the jet exit region has important dynamical implications for the extratropical atmospheric circulation at high latitudes. For instance, it results in enhanced upper-level divergence over the central North Pacific along the poleward flank of the jet exit region (indicated by the sense of the anomalous ageostrophic wind in Fig. 22), which provides a source for enhanced anticyclonic vorticity and increased heights in that region. Enhanced westerlies and increased storminess were observed in the region poleward of these increased heights [see section 4a(1), Fig. 27], which ultimately contributed to



above-normal precipitation in the Pacific Northwest United States and western Canada [see section 4a(1)].

## 2) ZONALLY SYMMETRIC STREAMFUNCTION ANOMALY PATTERN

Anticyclonic circulation anomalies, indicated by positive streamfunction anomalies in the Northern Hemisphere and negative streamfunction anomalies in the Southern Hemisphere, were evident in the lower and middle latitudes of both hemispheres in all seasons (Fig. 23). This global-scale anomaly pattern is a leading mode of interannual variability, explaining approximately 43% of the total interannual variance (Mo and Kousky 1993). This mode is strongly influenced by the ENSO cycle, with the pattern of tropical convection typical of La Niña conditions favoring the anomalous streamfunction pattern observed during 1999. In contrast, an El Niño-like pattern of tropical convection favors a reversal in the sign of the streamfunction anomalies and an opposite phase of the mode.

This global-scale mode of atmospheric variability also strongly modulates Atlantic and eastern Pacific basin hurricane activity during the August–November period (Bell and Chelliah 1999) as well as rainfall across the Sahel region of western Africa. The phase of the mode observed during 1999 favors persistent regional circulation features that are conducive to increased tropical storm activity over the North Atlantic and to a wet Sahel, along with a suppressed eastern Pacific hurricane season. The opposite phase of the mode, as was observed during the 1997–98 El Niño, favors persistent regional circulation features that suppress tropical storm activity over the North Atlantic, which contribute to a drier-than-normal Sahel and which are conducive to an active eastern Pacific hurricane season.

## 4. Regional climate highlights

### a. North America

#### 1) HEAVY WINTERTIME PRECIPITATION IN THE PACIFIC NORTHWEST

The Pacific Northwest region of the United States receives its most substantial rains during the cool season. The largest totals are typically observed during

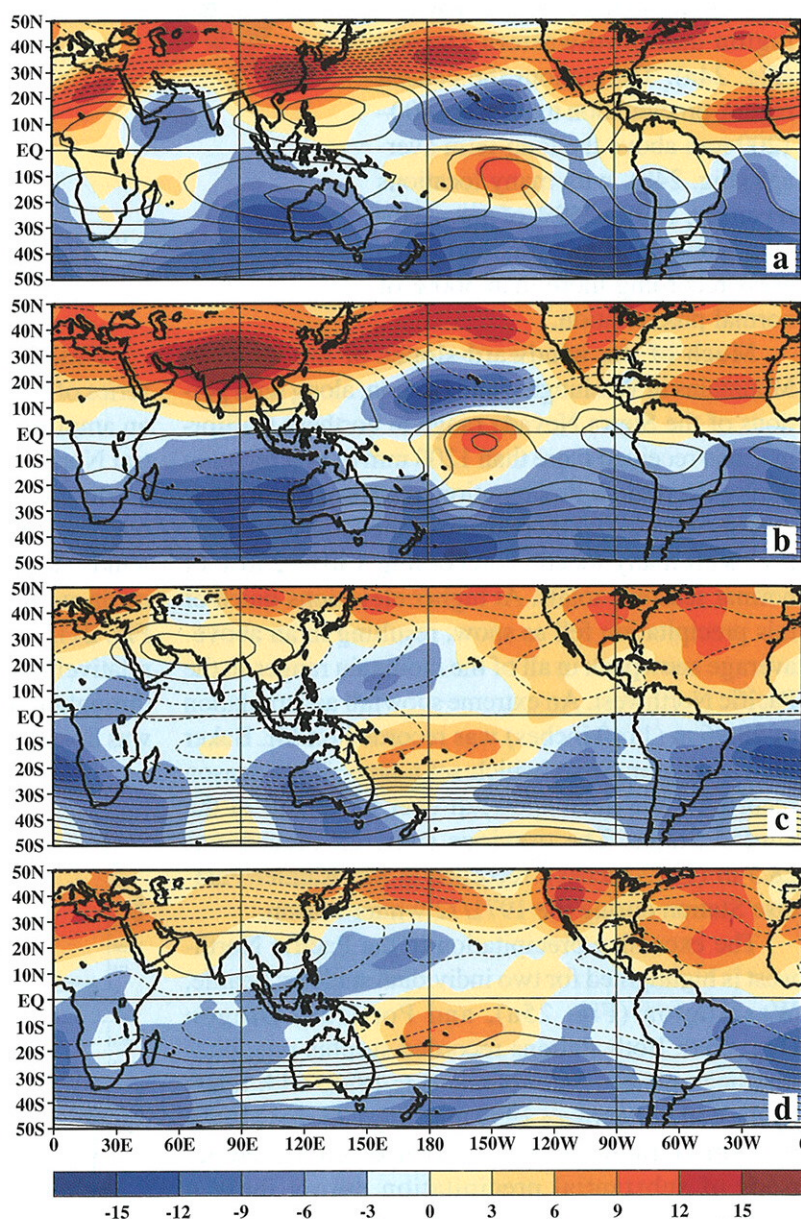


FIG. 23. Seasonal 200-hPa streamfunction (contours) and anomalies (shaded) during (a) DJF 1998–99, (b) MAM 1999, (c) JJA 1999, and (d) SON 1999. Units are  $1.0 \times 10^{-6} \text{ m}^2 \text{ s}^{-1}$ . Contour interval is 10. In the Northern Hemisphere, positive (negative) values indicate an anticyclonic (cyclonic) circulation. In the Southern Hemisphere, negative (positive) values indicate a cyclonic (anticyclonic) circulation. Anomalies are departures from the 1979–95 base period means.



November–February along the coast, and also along the windward slopes of the mountain ranges that extend from Canada southward through western Washington and Oregon to central California. During November 1998–February 1999, much of the coastal region recorded more than 1600 mm of precipitation, with the largest totals exceeding 2000 mm over the Olympic Peninsula of Washington and northwestern Oregon (Fig. 24a). Throughout the coastal region, precipitation totals were 400–1200 mm above the long-term average (Fig. 24b), with many locations recording 150%–250% of normal total seasonal precipitation and some areas recording more than 300% of normal precipitation.

Much of the windward slopes of the Cascade Mountains in Washington and Oregon, along with portions of the Sierra Nevada range in northern California, also received more than 1200 mm of precipitation during the period. Precipitation totals in each of these regions were 200–800 mm above the long-term average, with many locations recording 150%–250% of normal seasonal totals. At higher elevations much of this precipitation fell as snow, resulting in an above-average snowpack in all of the mountain ranges in the Pacific Northwest. An extreme snowfall accumulation of 28.96 m (1140 inches) was recorded on Mt. Baker in Washington State, which set a new single-season record for the most snowfall ever measured in the United States. The previous snowfall record was 28.5 m (1122 inches), recorded at Mt. Rainier/Paradise Station during the 1971/72 winter season.

The excessive precipitation in the Pacific Northwest is highlighted for two individual stations: Seattle, Washington (Fig. 25a), and Portland, Oregon (Fig. 26a). Both stations recorded surplus precipitation beginning in early November 1998, with totals by the end of February 1999 reaching 875 mm (165% of normal). Both stations experienced prolonged periods of substantial precipitation during these 4 months, interspersed often with only a few days of dryness between major precipitation events (Figs. 25b, 26b). The most prolonged periods of nearly continuous precipitation at both stations were recorded between mid-November and mid-December, and from mid-January through the end of February.

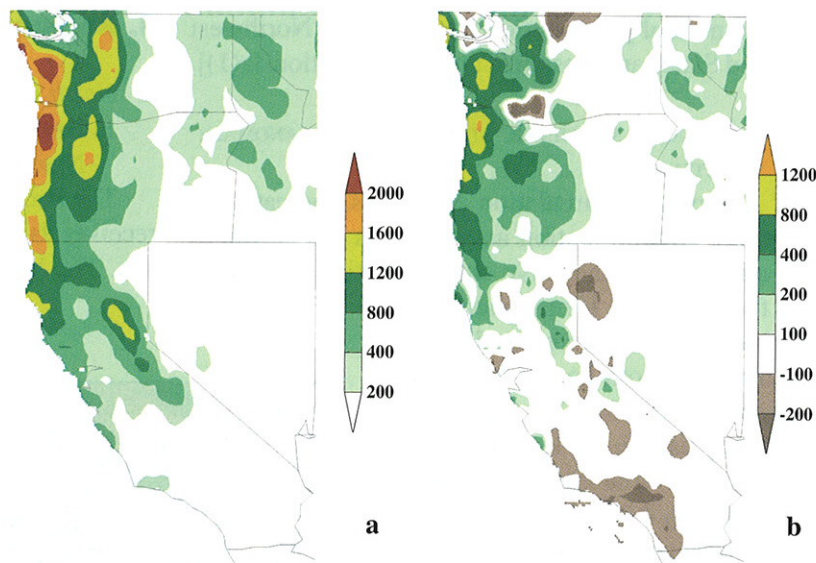


FIG. 24. November 1998–February 1999 (a) total precipitation and (b) precipitation anomalies (in mm). Anomalies are departures from the 1961–90 base period means.

This above-average precipitation resulted from a series of major winter storms that were associated with an amplified storm track that extended from the central North Pacific to the Pacific Northwest and southwestern Canada (Fig. 27). This enhanced storm track was located within a region of enhanced westerly winds along the poleward (cyclonic shear) side of the mean wintertime jet stream (compare Fig. 27 with Fig. 21), and also contributed to an enhanced flow of relatively mild marine air into western North America throughout the period. This anomalous westerly flow was linked to a large-scale pattern characterized by be-

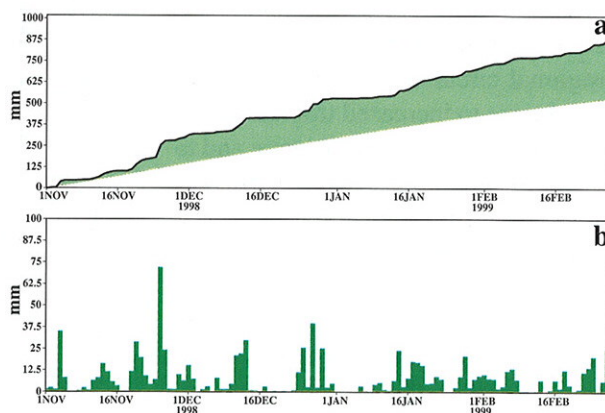


FIG. 25. Daily rainfall (mm) at Seattle, Washington, during November 1998–February 1999: (a) accumulated observed (thick line) and accumulated climatological mean (thin line, 1961–90 base period), and (b) observed daily total. Shading in (a) shows the accumulated departure from normal, with green shading indicating positive departures.



low-average heights over the high latitudes of the North Pacific and above-average heights over the central North Pacific in association with ongoing La Niña conditions [see section 3e(1), Fig. 20b].

## 2) THE 1999 NORTH ATLANTIC AND EASTERN NORTH PACIFIC HURRICANE SEASONS

### (i) The North Atlantic hurricane season

The North Atlantic hurricane season runs from June through November and exhibits a peak in activity between mid-August and mid-October, primarily in response to systems developing from African easterly wave disturbances. In an average season, 9–10 tropical storms are generally observed over the North Atlantic, with 5–6 becoming hurricanes and 2 reaching intense hurricane status [measured by a category 3, 4, or 5 on the Saffir–Simpson scale (Simpson 1974)]. The 1999 season featured 12 named storms, with 8 of these systems becoming hurricanes and 5 reaching intense hurricane status. Most systems developed over the tropical Atlantic, Caribbean Sea and the southern Gulf of Mexico, which is typical of the main development region observed during other active years (Shapiro and Goldenberg 1998). Only one system during the 1999 season developed prior to 18 August, and four systems developed after 12 October. Three of these late-season storms became hurricanes, with the last (Hurricane Lenny) reaching category-4 status. Lenny developed in mid-November and moved eastward across the central Caribbean Sea. This unusual track enabled it to become the first hurricane to strike the Lesser Antilles Islands from the west.

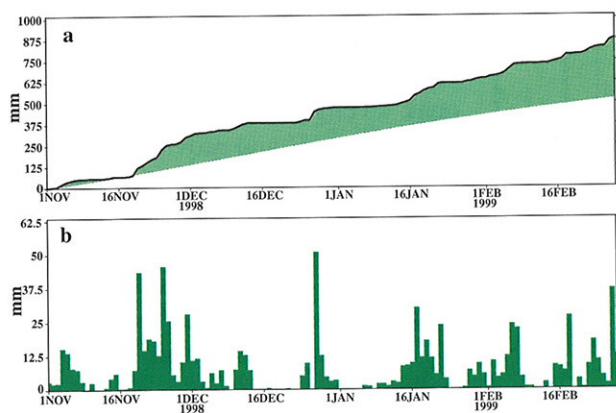


FIG. 26. Daily rainfall (mm) at Portland, Oregon, during Nov 1998–Feb 1999: (a) accumulated observed (thick line) and accumulated climatological mean (thin line, 1961–90 base period), and (b) observed daily total. Shading in (a) shows the accumulated departure from normal, with green shading indicating positive departures.

Five tropical systems made landfall in the United States during the 1999 season. The first of these was intense Hurricane Bret, which hit a sparsely populated region of southeastern Texas in late August. The second and third landfalling systems were Tropical Storm Dennis and Hurricane Floyd, which produced extremely large rainfall totals over southeastern Virginia and eastern North Carolina and led to record flooding in some areas [see section 4a(4)(ii)]. The fourth was Tropical Storm Harvey, which formed in the Gulf of Mexico and impacted southern Florida and the Florida Keys. The fifth was Hurricane Irene, which also moved across southern Florida and produced considerable freshwater flooding in that region.

Two measures of overall seasonal activity are used extensively by Gray and colleagues (1999, personal communication). The first is net tropical cyclone activity (NTC), which is based on a linear combination of the number of named storms, number of hurricanes, number of intense hurricanes, number of named storm days, number of hurricane days, and number of intense hurricane days. However, these six parameters represent highly discrete distributions and are also strongly statistically correlated. The second measure of overall seasonal activity is referred to as the hurricane destruction potential (HDP), which is calculated by summing the squares of the estimated 6-hourly maximum sustained wind speed ( $V_{\max}^2$ ) for all periods in which the system is a hurricane. This index represents a single, continuous distribution that implicitly accounts for numbers of hurricanes, yet also gives more weight to strong systems and long-lasting systems. A slight modification of the HDP index involves accumulating  $V_{\max}^2$  for all 6-hourly periods in which the system is either a tropical storm or hurricane, thereby also accounting for the number and duration of storms

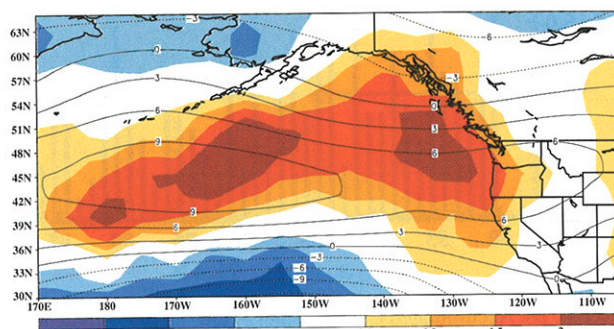


FIG. 27. Nov 1998–Feb 1999 anomalous 200-hPa zonal wind (contours,  $\text{m s}^{-1}$ ) and standardized anomalous variance of high-pass filtered (2.5–6 day) 700-hPa heights (shaded). Anomalies are departures from the 1964–99 base period monthly means.



while at a tropical storm status. This modified HDP index is referred to as accumulated cyclone energy (ACE) index (Fig. 28), and is both a physically and statistically reasonable measure of overall activity during a given hurricane season.

Overall, the 1999 hurricane season was extremely active by all measures, and according to the ACE index was ranked seventh in terms of overall activity since 1950 (Fig. 28). This index also indicates that four of the seven most active years since 1950 have occurred since 1995. This frequency of occurrence of extremely active years since 1995 is in sharp contrast to the 1970–94 period, which was marked by generally reduced overall tropical storm and hurricane activity.

Tropical storm and hurricane activity over the North Atlantic is strongly influenced by the vertical wind shear between the upper (200 hPa) and lower (850 hPa) levels of the atmosphere over the western Atlantic and Caribbean Sea. Active years feature low vertical shear (less than approximately  $8 \text{ m s}^{-1}$ ) in these regions, while inactive years feature high vertical shear.

The August–October 1999 period featured very low wind shear across the western tropical Atlantic, Caribbean Sea, and southern Gulf of Mexico (Fig. 29a), with mean shear values in some regions dropping below  $4 \text{ m s}^{-1}$ . Over much of the tropical Atlantic, this shear was anomalously low (Fig. 29b), which is typical of other active hurricane seasons (Landsea et al. 1998; Goldenberg and Shapiro 1997). Over the Caribbean Sea and western Atlantic, these low shear val-

ues resulted from a combination of anomalous upper-level easterly winds averaging  $2\text{--}4 \text{ m s}^{-1}$  (Fig. 30a) and anomalous low-level westerly winds averaging  $1\text{--}3 \text{ m s}^{-1}$  (Fig. 30b). At upper levels, these easterly wind anomalies covered the entire Atlantic in both hemispheres between  $20^\circ\text{N}$  and  $20^\circ\text{S}$ , and also extended across the entire tropical and subtropical eastern Pacific. At lower levels, the pattern of westerly wind anomalies was also quite extensive, spanning the area from the eastern North Pacific eastward to the African Sahel region (Fig. 30b). These upper-level and lower-level wind anomalies were linked to a global-scale circulation pattern featuring positive upper-level streamfunction anomalies across the entire middle latitudes of the Northern Hemisphere [see section 3e(2), Fig. 23c] and negative streamfunction anomalies across the entire subtropical and middle latitudes of the Southern Hemisphere.

Tropical cyclogenesis in active years is often associated with African easterly waves, whose evolution is strongly influenced by the structure and location of the African Easterly Jet (AEJ). The AEJ is centered near 600–700 hPa and provides the background flow within which the African easterly waves move and evolve (Reed et al. 1977). There are notable differences in both the structure and location of the AEJ between active and inactive years (Bell and Halpert 1998; Halpert and Bell 1997), and these differences represent another fundamental component of the coherent atmospheric variability associated with active and inactive hurricane seasons (Bell and Chelliah 1999).

The AEJ normally extends from western Africa to the central subtropical North Atlantic (Fig. 31a), with the jet core located near  $15^\circ\text{N}$ . The jet reaches peak strength between the 600- and 700-hPa levels and provides the “steering flow” for the easterly waves. It is also an important energy source for the waves, which propagate through the cyclonic shear zone (Fig. 31b) along the equatorward flank of the jet (Reed et al. 1977). This cyclonic shear zone is normally well defined over the eastern tropical Atlantic and western Africa between  $8^\circ$  and  $15^\circ\text{N}$  and overlaps the area of low vertical wind shear (indicated by shading in Figs. 31a,b). This overlap is generally most extensive during the climatological September peak in hurricane activity.

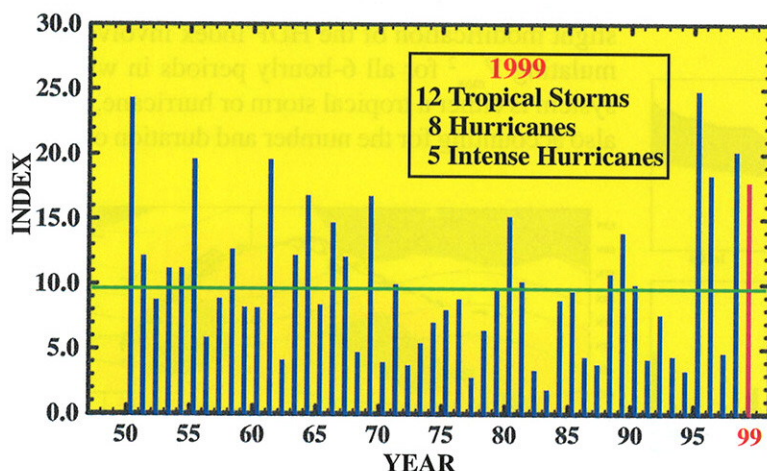


FIG. 28. Accumulated Cyclone Energy (ACE) Index indicating overall Atlantic basin tropical storm and hurricane activity for each Jun–Nov season between 1950 and 1999. The ACE index is calculated by summing the squares of the 6-hourly maximum sustained wind speed ( $V_{\max}^2$ ) for all named storms during their existence as a tropical storm or hurricane. Seasonal index values have been divided by 100 000 for display purposes only.



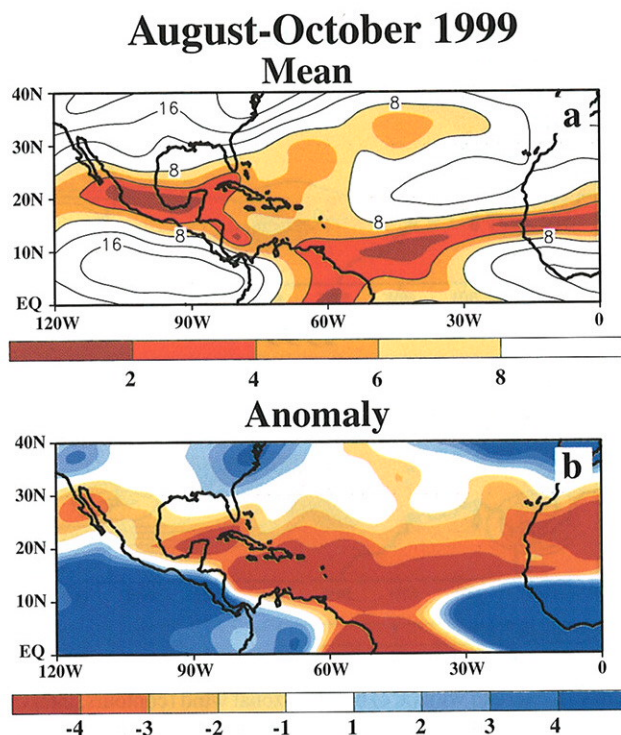


FIG. 29. Magnitude of the August–October 1999 mean and anomalous vertical wind shear. Wind shear is calculated as the difference in wind speeds between 200 and 850 hPa (contour interval is  $4 \text{ m s}^{-1}$ ). Shaded areas in (a) indicate where the vertical wind shear is less than  $8 \text{ m s}^{-1}$  and are considered favorable for tropical cyclone formation. Below-average wind shear values in panel (b) are shaded red, while above-average shear values are shaded blue.

There is considerable year-to-year variability in the latitudinal position of the AEJ, in the westward extent of the AEJ, and in the strength and westward extent of the cyclonic vorticity along the southern flank of the jet (Bell and Chelliah 1999). During the active August–October 1999 season, the AEJ was very well defined and located between  $17.5^\circ$  and  $20^\circ\text{N}$  (Fig. 31c), which is approximately  $2.5^\circ$ – $5^\circ\text{N}$  of its climatological mean position. This position of the AEJ during 1999 is typical of other active hurricane seasons, and is also considerably farther north than its mean latitude ( $10^\circ$ – $12^\circ\text{N}$ ) often observed during inactive years (Bell and Halpert 1998). The AEJ also featured strong cyclonic shear along its entire equatorward flank between  $10^\circ$  and  $15^\circ\text{N}$  during 1999 (Fig. 31d), along with a westward extension of this high vorticity zone to the central tropical Atlantic. These high values of cyclonic vorticity resulted from large westerly wind anomalies near  $10^\circ\text{N}$  throughout the lower troposphere over the central and eastern Atlantic (Fig. 30b). These high vorticity values and

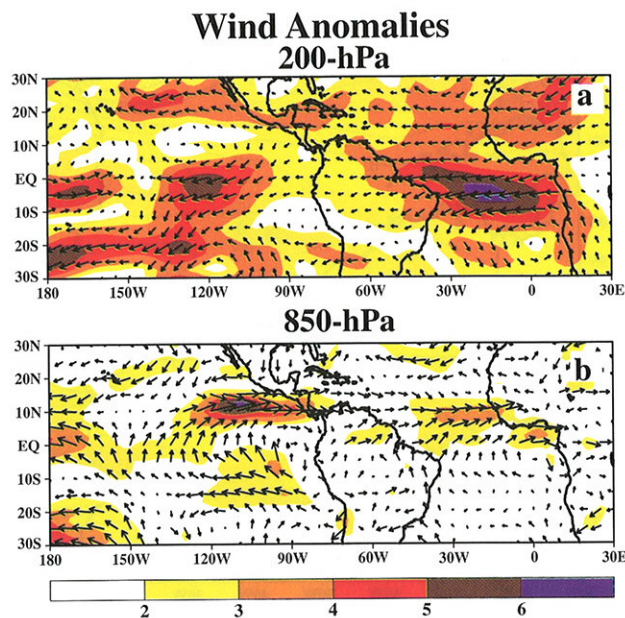


FIG. 30. Aug–Oct anomalous wind speed (shaded;  $\text{m s}^{-1}$ ) and anomalous vector wind at (a) 200 and (b) 850 hPa. Anomalies are departures from the 1979–95 base period means.

their pronounced westward extent are typical of other active hurricane seasons. They are also distinct from the climatological mean conditions (Fig. 31b) and from inactive hurricane years that feature low values of cyclonic vorticity north of  $10^\circ\text{N}$  and a confinement of high cyclonic vorticity to the eastern tropical Atlantic (e.g., Bell and Halpert 1998, their Fig. 34).

Also during 1999, the region of high cyclonic vorticity strongly overlapped the area of low vertical wind shear (indicated by the shading) over the central Atlantic (Fig. 31d). While the area of overlap between the 1999 season and the climatological normal (Fig. 31b) is similar, the magnitude of cyclonic relative vorticity is much stronger in the overlap region during the 1999 season. This favorable location and horizontal structure of the African easterly jet, combined with its proximity to the extended region of low vertical wind shear, contributed to the recurring tropical cyclogenesis and intense hurricane development from easterly waves observed during the season. The increased cyclonic vorticity and westerly wind anomalies at low levels were also evident across the African Sahel region and contributed to enhanced July–September 1999 rainfall in that region [see section 4b(2)].

This variability in the AEJ is also strongly coupled to the prominent global-scale mode of upper-level streamfunction anomalies (Fig. 23c), which is ulti-



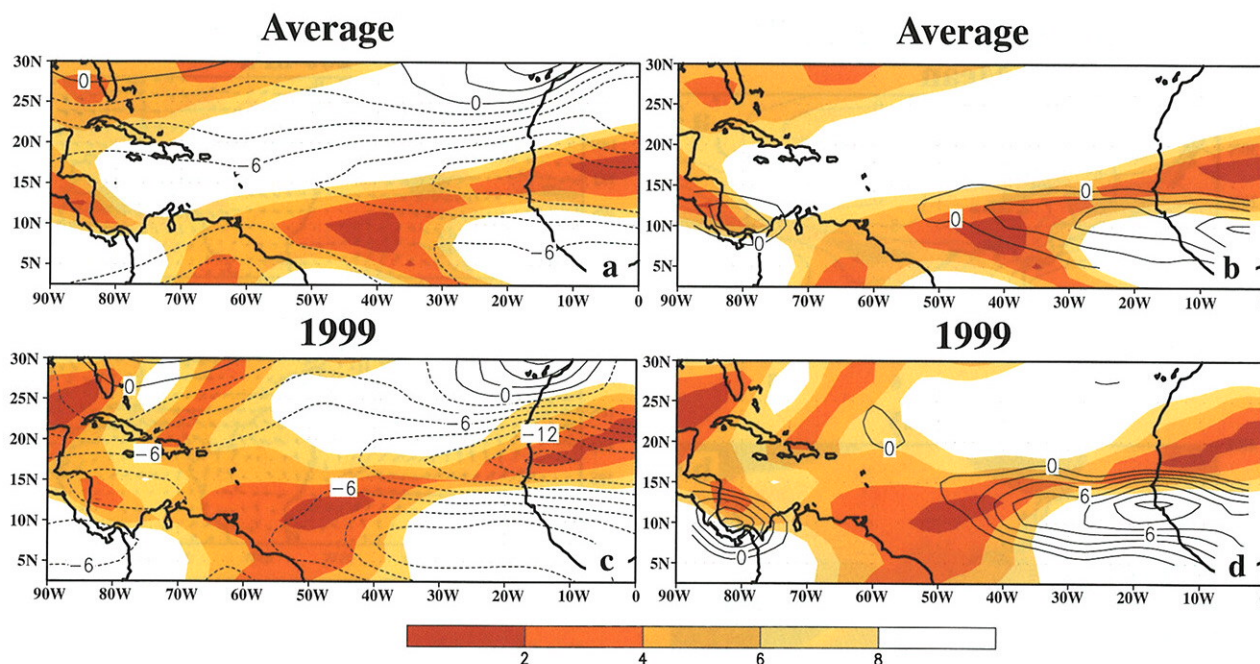


FIG. 31. Aug–Sep mean 200–850-hPa vertical wind shear (shaded,  $\text{m s}^{-1}$ ), overlaid with (a, c) 600-hPa zonal wind (contours, interval is  $2 \text{ m s}^{-1}$ ) and (b, d) 600-hPa cyclonic relative vorticity (contours, interval is  $2 \times 10^{-6} \text{ s}^{-1}$ ). Panels (a, b) show 1979–95 climatological mean conditions and panels (c, d) show 1999 mean conditions.

mately linked to the patterns of tropical convection. As discussed in section 3e(2), this mode was established early in the year (Fig. 23b) and neither the La Niña nor its attendant convection patterns dissipated during the next several months. The expected persistence of the global mode during the summer months led to a strong expectation that the 1999 hurricane season would indeed feature anomalous upper-level easterly winds across the tropical Atlantic, low vertical wind shear across the central and western tropical Atlantic, and a structure and location of the AEJ that was similar to the observed features. As a result, it was evident that there was a strong likelihood of above-normal tropical storm and hurricane activity over the North Atlantic even well prior to the onset of the season.

#### (ii) Eastern North Pacific hurricane season

The eastern North Pacific hurricane season runs from May through November. On average, there are 16 named storms during the season, 9 of which typically become hurricanes and 4 of which become intense hurricanes. Overall, the 1999 season was one of the most inactive on record with only 9 tropical storms, 6 of which became hurricanes and 2 of which became intense hurricanes. This relative inactivity was linked to a large region of high vertical wind shear that

covered much of the main development region of the eastern North Pacific for most of the season (Fig. 29a).

There is often a negative correlation between Pacific basin and Atlantic basin hurricane activity, with relatively inactive Pacific hurricane seasons accompanying active Atlantic hurricane seasons and vice versa. This relationship results from the large-scale pattern of anomalous vertical wind shear, which, during active Atlantic hurricane seasons, is below normal across the North Atlantic and above normal over the eastern tropical North Pacific. This dipole pattern of shear anomalies was prominent during the 1999 hurricane season (Fig. 29b) and was related to a combination of upper-level easterly wind anomalies (Figs. 30a) and lower-level westerly wind anomalies (Fig. 30b) across the North Atlantic and eastern North Pacific.

#### 3) THE JULY–SEPTEMBER 1999 SOUTHWESTERN UNITED STATES SUMMER MONSOON

During July–September precipitation over Mexico and the southwestern United States is controlled by the continental-scale monsoon circulation. Interannual variations in this summer monsoon can be influenced by various ocean-based and land-based factors (e.g., SST, soil moisture) that provide sources of “memory” of antecedent climate anomalies such as extremes in the ENSO cycle. In a recent study Higgins et al. (1998)



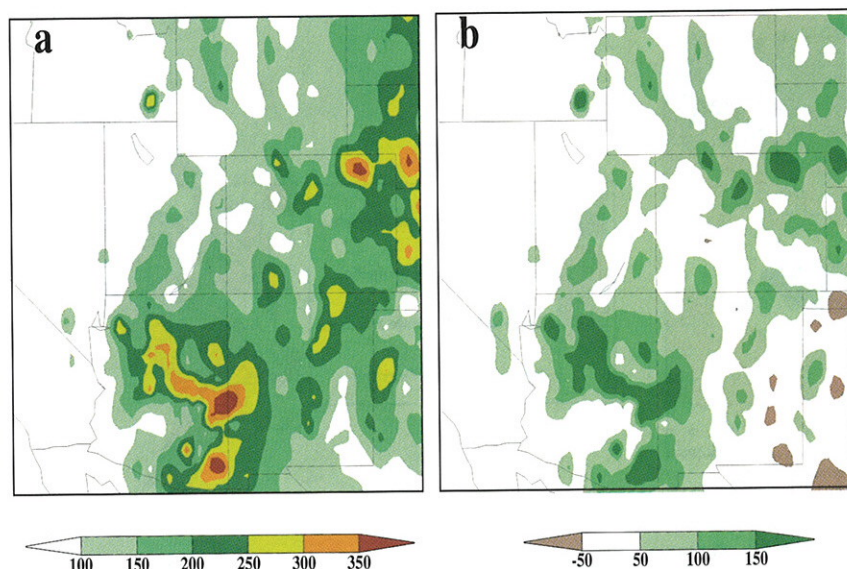


FIG. 32. Jul–Sep 1999 (a) rainfall totals (mm) and (b) departures from normal (mm) over the southwestern United States. Departures are from the 1961–90 base period means.

showed that wet summer monsoons in the southwestern United States often follow winters characterized by a combination of dry conditions in the southwestern United States and wet conditions in the Pacific Northwest, as is typical of La Niña episodes. Consistent with this finding, Gutzler and Preston (1997) showed that interannual fluctuations of summer rainfall in New Mexico are linked to antecedent spring snowpack over the southern U.S. Rocky Mountains. They argue that La Niña events during the preceding winter and spring often contribute to a relatively poor snowpack in the southern Rockies and vice versa for El Niño. Consequently, relatively less heating is required in low-snowpack years to establish the necessary land–sea thermal contrast that helps drive the summer monsoon. Under these circumstances wetter-than-normal conditions are often observed over the southwestern United States during the monsoon season.

Overall, the 1999 southwestern U.S. monsoon season featured substantial rainfall throughout the southwestern United States (Fig. 32a), with seasonal totals generally above average throughout the region (Fig. 32b). The largest anomalies during the season were observed in Arizona and New Mexico, where the combined rainfall total in these two states was the second largest in the historical record dating back to 1960 (Fig. 33). Much of central and northern Arizona, and portions of western New Mexico, recorded totals that were more than 150 mm above-normal during the season, with many locations recording more than twice the normal seasonal total.

The onset of the summer rains in the southwestern United States occurred during the first week of July, which is very close to the climatologically favored time for this region. Much of the monsoonal rainfall occurred during July and August, although heavy precipitation also continued over much of Arizona during September. Farther south, Mexico and Central America also experienced increased monsoon rainfall, particularly during June and September with a midsummer dry period during August.

The wetter-than-normal conditions over the southwestern United States and Mexico were linked to an enhanced upper-level

monsoon anticyclone that was extended northward of its climatological mean position (Fig. 34). This feature was embedded in a much larger-scale anomalous large-scale anticyclonic circulation that covered much of the United States, Mexico, and the adjacent ocean waters (Fig. 23c), and allowed enhanced monsoonal flow to penetrate the southwestern United States from both the Gulf of Mexico and the Gulf of California. This anomalous anticyclonic circulation was likely influenced by the strong 1998–99 La Niña episode and by the accompanying relatively poor snowpack in the southern Rockies during the preceding two seasons

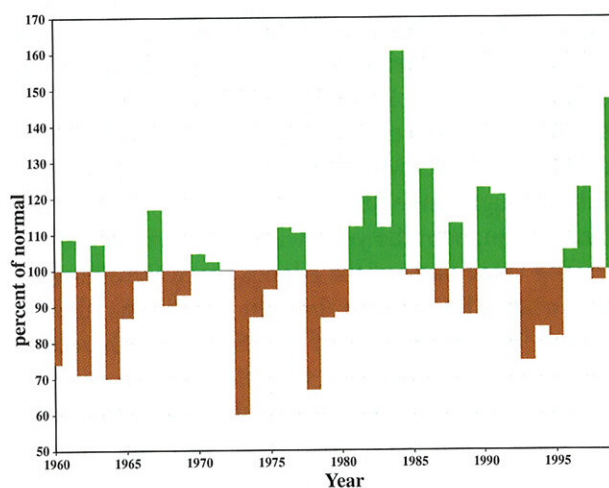


FIG. 33. Areal weighted percent of normal precipitation relative to the 1961–90 base period for the Jul–Sep period over Arizona and New Mexico (32°–37°N; 102.5°–115°W).



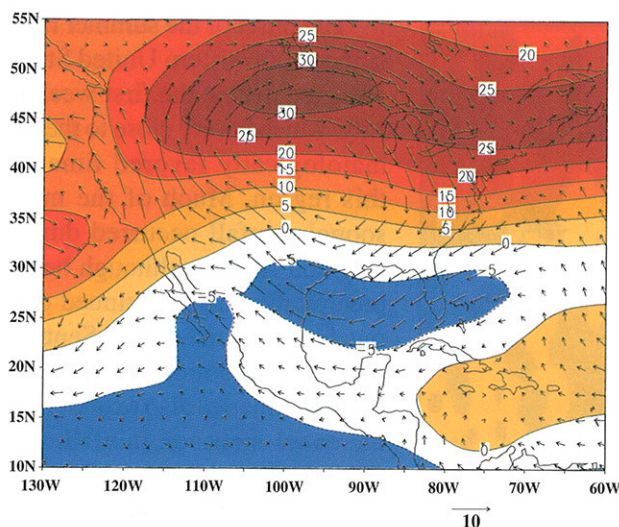


FIG. 34. Jul–Aug 1999 200-hPa zonal wind ( $\text{m s}^{-1}$ , shading) and departures of vector wind from normal. Departures are from the 1979–95 base period means. The characteristic vector length is  $10 \text{ m s}^{-1}$ .

(see section 2a, Figs. 4a,b). In contrast, in the region downstream of this enhanced anticyclonic circulation, significantly below-normal rainfall and severe drought conditions were observed across large portions of the central and eastern United States during July and August [see section 4a(4)].

#### 4) DROUGHT IN THE UNITED STATES

Drought impacted large portions of the United States during 1999, with 46 states experiencing at least some moisture deficits and 29 states affected by severe to extreme drought. Overall, the most significant drought conditions occurred in three general regions: (a) across large portions of the northeastern quadrant of the country during April–August, with long-term dryness dating back to July 1998 in some areas; (b) in the Ohio Valley, Tennessee Valley, interior Southeast, middle and lower Mississippi Valley, and Texas from July through November; and (c) in the Hawaiian Islands throughout the year, with long-term dryness affecting some parts of the Islands since October 1997. Elsewhere, less severe drought conditions also impacted interior sections of the Pacific Northwest and Intermountain West from May through November.

The various droughts across the United States during 1999 were associated with many agricultural and ecological impacts. According to the U. S. Department of Agriculture (USDA) drought conditions during 1999 resulted in a 3.2% decrease from 1998 in total national corn production, in a 4% decrease in soybean

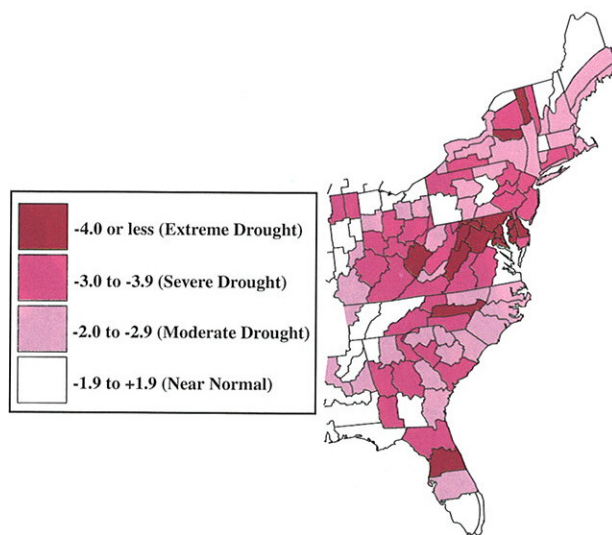


FIG. 35. Palmer drought severity index ending 14 Aug 1999.

production, and in a 9.6% decrease in the combined spring and winter wheat crops to levels not seen since 1996. In addition, approximately 5.7 million acres were consumed by wildfires across the United States during the year [National Interagency Coordination Center (NICC)], which is 65% above the 1991–99 average and is the largest consumed acreage recorded since 1996.

#### (i) The Northeast, Mid-Atlantic, central Appalachians, and middle Ohio Valley

Severe drought occurred from April through mid-August 1999 in the Northeast, the mid-Atlantic, central Appalachians, and the middle Ohio Valley regions (Fig. 35). Precipitation totals for this 4.5-month period were less than 300 mm across most of the region (Fig. 36a), and less than 200 mm in eastern Pennsylvania, northeastern Virginia, and central Maryland. Totals were generally more than 100 mm below the long-term average throughout this region (Fig. 36b) and 200–300 mm below average in south-central Ohio, parts of Virginia, central Maryland, and southeastern Pennsylvania. In many locations from central Maryland northeastward to southeastern Maine, rainfall during the period was less than half the long-term mean. In Delaware and Rhode Island, statewide precipitation totals for April–July 1999 were the lowest in the last 105 years of record (Fig. 37a). Statewide totals were the second lowest on record for this period in Connecticut, Maryland, New Jersey, and West Virginia, and one of the seven lowest on record in most of the remaining northeastern states.



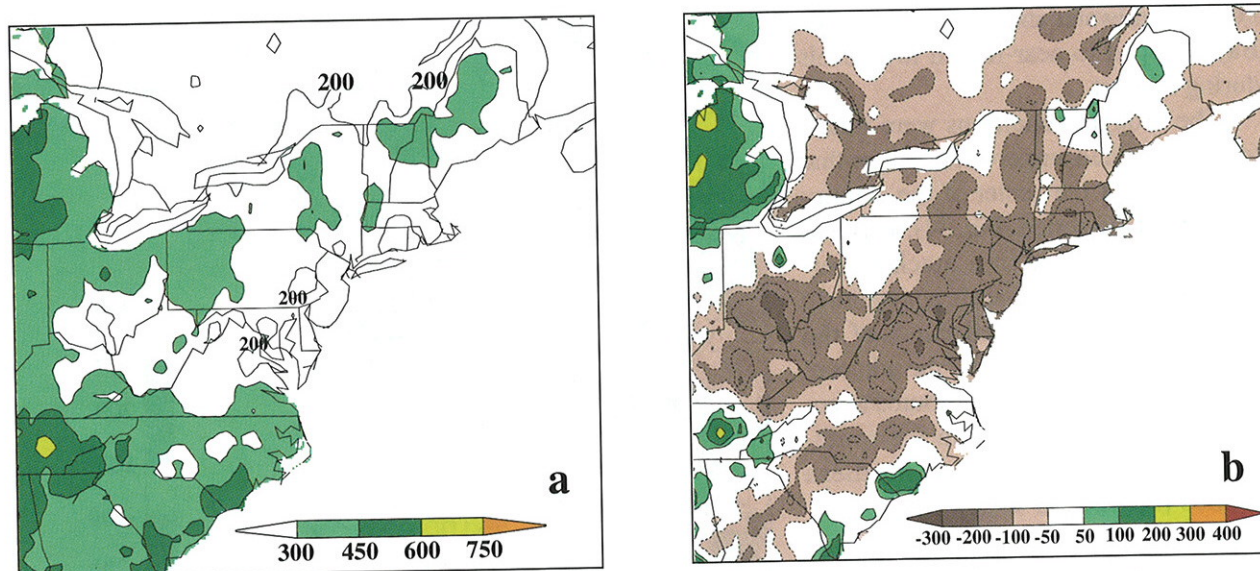


FIG. 36. Precipitation (a) totals and (b) anomalies in mm during 1 Apr–13 Aug 1999. Anomalies are departures from the 1961–90 base period means.

The 1999 drought followed a prolonged period of below-average rainfall that began in July 1998 and was interrupted by near-average to above-average precipitation only during January–March 1999. For the July 1998–July 1999 period as a whole, rainfall was 60%–65% of normal, with the largest rainfall deficits (exceeding 300 mm) observed in northern Virginia, northwestern Maryland, and scattered portions of southwestern Virginia, West Virginia, and southern Ohio (Fig. 38). Other parts of the mid-Atlantic region and central Appalachian Mountain region recorded deficits exceeding 200 mm during the period. Statewide, July 1998–July 1999 was the driest such period in 104 years of record in Virginia, the second driest in Maryland, the third driest in both New Jersey and West Virginia, and the fourth driest in Delaware (Fig. 37b).

This drought was associated with a variety of impacts across the region. The USDA reported that corn crop production in Pennsylvania and Maryland dropped 47% and 23% from 1998, respectively, and the Virginia tobacco crop production fell 9%. Also,

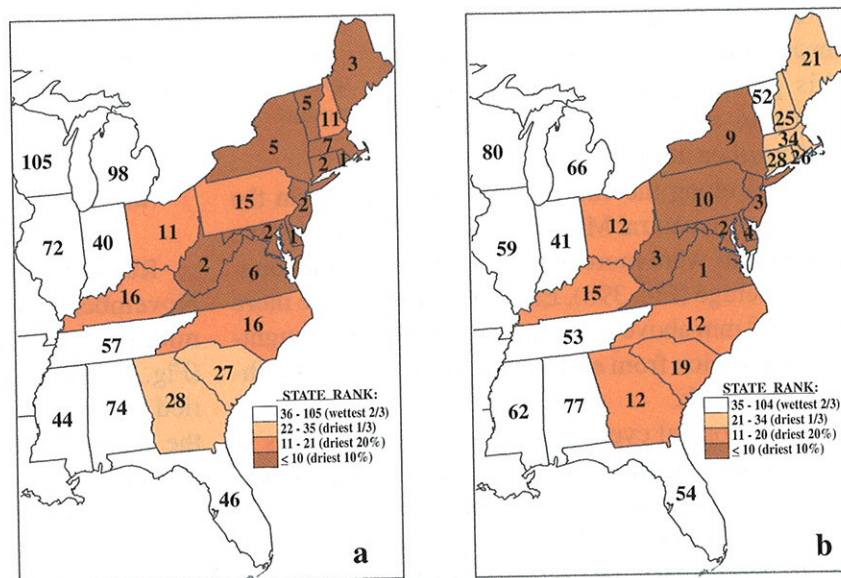


FIG. 37. Statewide rankings of precipitation totals during (a) Apr–Jul 1999 and (b) Jul 1998–Jul 1999. Ranks are based on total precipitation during the above periods from 1895–1999. A rank of 1 indicates that statewide rainfall during 1999 was the lowest in the historical record dating back to 1895.

hay production in West Virginia and Pennsylvania declined 15% to 30% from 1998. Stream flows were generally below the tenth percentile level in the mid-Atlantic and Northeast, according to the U.S. Geological Survey (USGS), and water supplies dropped to alarmingly low levels at times in some areas, requiring local and state governments to implement mandatory water restrictions. In the Chesapeake Bay area,



both groundwater and total inflow to the Bay dropped to near-record low levels during August.

The drought conditions were linked to an enhanced upper-level ridge that persisted over the center of the country throughout the period (Fig. 34). This feature was embedded in a much larger-scale anomalous large-scale anticyclonic circulation that covered much of the United States, Mexico, and the adjacent ocean waters, and also contributed to enhanced monsoonal rains in the southwestern United States and northern Mexico [see section 4a(3)].

*(ii) Drought-ending rains in north-eastern quadrant of United States*

Severe drought conditions in the northeastern United States ended during mid-August–mid-October in response to exceptionally large rainfall totals throughout the region (Fig. 39a). During this period rainfall totals exceeded 750 mm in eastern North Carolina and northeastern South Carolina, and 300 mm along the entire eastern seaboard from the Carolinas to central Maine. In eastern North Carolina these totals were more than 500 mm above the long-term average (Fig. 39b). Elsewhere, totals were more than 200 mm above average over most of the drought-stricken region from eastern South Carolina to southern New York.

Two tropical cyclones, Tropical Storm Dennis in late August and Hurricane Floyd in early September, contributed significantly to this excessive rainfall. Rainfall totals from Tropical Storm Dennis were largest in eastern North Carolina and southeastern Virginia where they exceeded 100 mm (Fig. 40a), and in central North Carolina and central Virginia where they averaged 50–100 mm. Two weeks later, rainfall from Hurricane Floyd impacted the entire East Coast from South Carolina to Maine (Fig. 40b), with totals exceeding 200 mm from South Carolina to New York. The largest rainfall totals associated with Floyd occurred in northeastern South Carolina and eastern North Carolina, where 5-day totals exceeded 400 mm. Locally, 24-hour amounts during this period approached 500 mm near the approximate landfall site of Wilmington, North Carolina.

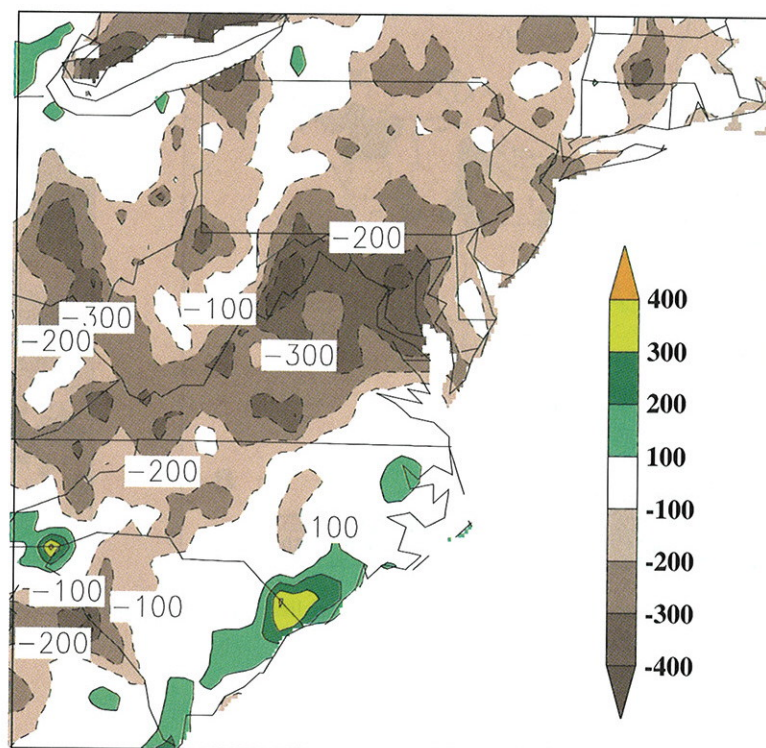


FIG. 38. Total precipitation (a) and anomalies (b) during 1 Jul 1998–31 Jul 1999. Units are mm. Anomalies are departures from the 1961–90 base period means.

*(iii) The Ohio Valley, Tennessee Valley, middle and lower Mississippi Valley, and Texas*

Rainfall was well below normal from July–November 1999 throughout the Ohio Valley, the middle and lower Mississippi Valley, and Texas (Fig. 41). Precipitation totals during this 5-month period were more than 100 mm below normal throughout the region, with the largest deficits reaching 200–400 mm in northeastern Texas, southern Arkansas, northern Louisiana, northern and western Mississippi, the western Tennessee Valley, and parts of Missouri. On a statewide basis, Arkansas experienced its driest July–November period in 105 years of record (Fig. 42), while Indiana and Missouri endured their second-driest such period, and Illinois and Louisiana experienced their third driest. In addition, totals were the fourth lowest since 1895 in Kentucky and Texas, and the fifth lowest in Tennessee. For the region as a whole (for the area depicted in brown in the inset in Fig. 43), July–November 1999 ranks as the driest such period in the past 105 years, with area-averaged precipitation deficits reaching 180 mm. This deficit exceeds the previous record negative anomaly of 150 mm set in 1924 and contrasts with the generally wetter-than-normal conditions that have been observed in this region since



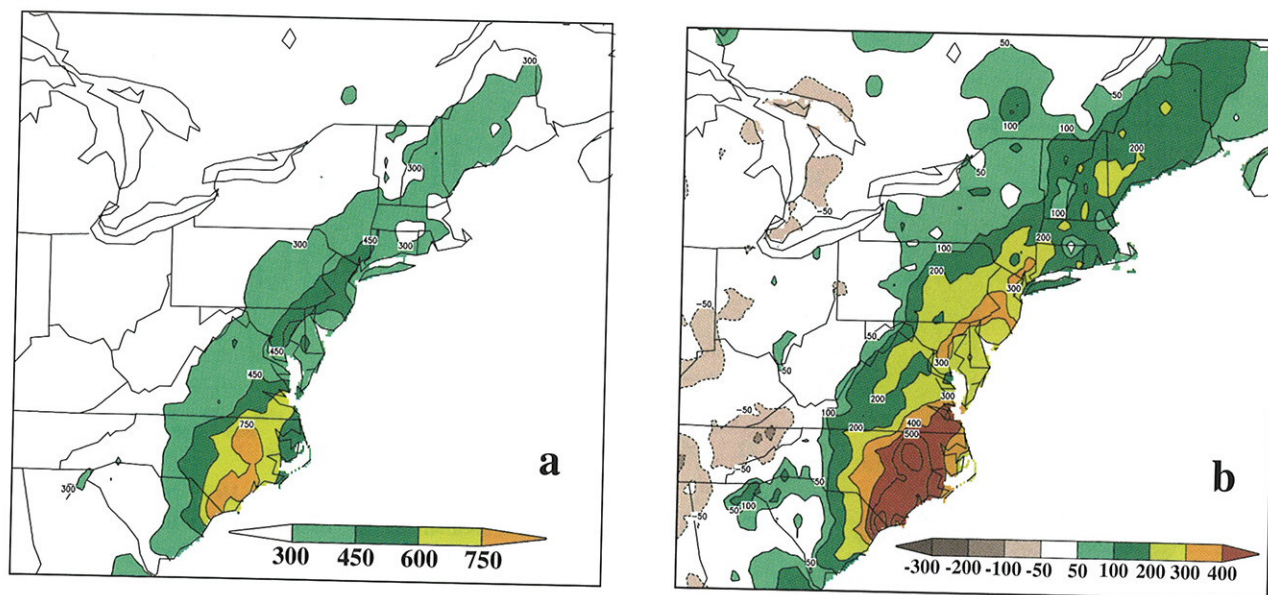


FIG. 39. (a) Total precipitation and (b) anomalies during 15 Aug–31 Oct 1999. Units are mm. Anomalies are departures from the 1961–90 base period means.

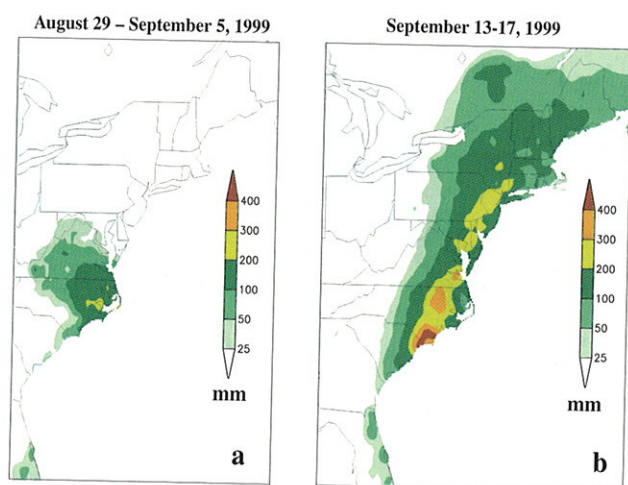


FIG. 40. Total precipitation (mm) from (a) Tropical Storm Dennis during 29 Aug–5 Sep 1999 and (b) Hurricane Floyd during 13–17 Sep 1999.

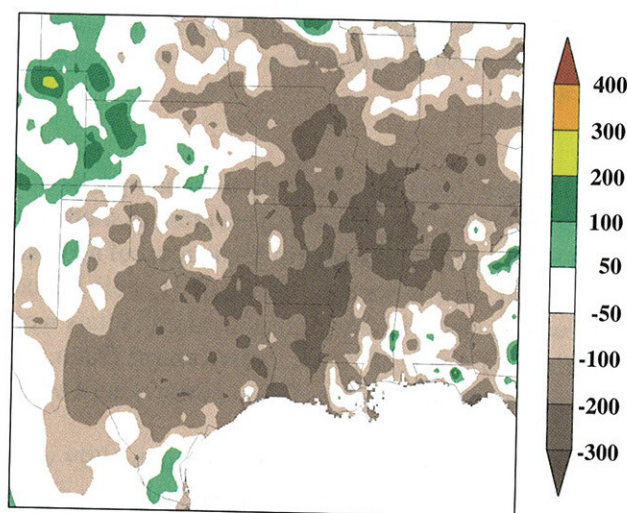


FIG. 41. Precipitation anomalies (mm) during Jul–Nov 1999. Anomalies are departures from the 1961–90 base period means.

1970. By the end of 1999, long-term dryness remained a concern throughout the region, with acute dryness still affecting central and northern Texas and the lower Mississippi Valley.

This drought was associated with substantial agricultural and hydrologic impacts. According to the USDA, Missouri and Ohio each reported 13%–16% decrease in corn and soybean production compared to 1998 levels. The wheat crop in Oklahoma experienced a 24% decline in output compared to 1998 levels, and hay production was 16%–31% lower than 1998 levels in several states. Stream flows were also greatly re-

duced during the last half of 1999, with many river levels below the tenth percentile in areas east of the Mississippi River and south of the Great Lakes (USGS).

#### (iv) Hawaii

Large portions of the Hawaiian Islands experienced a second consecutive year of below-normal rainfall during 1999, although totals were generally larger than those observed in 1998. This dryness contrasts with above-average rains that the islands have typically experienced during past La Niña episodes (Ropelewski



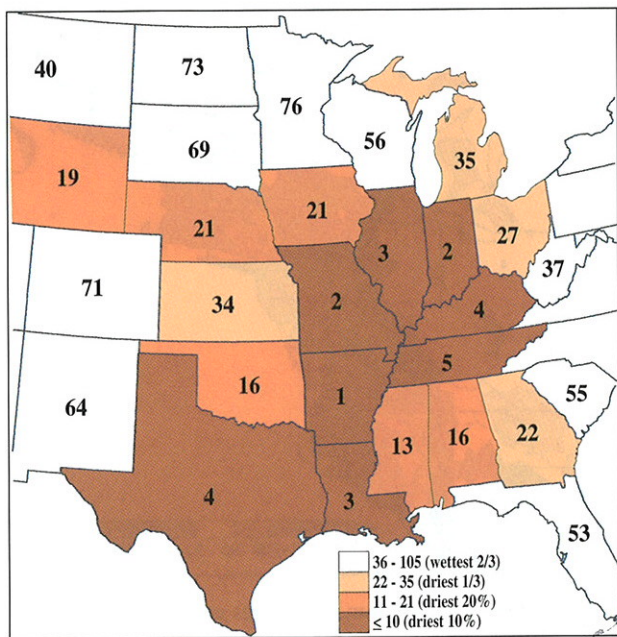


FIG. 42. Statewide rankings of precipitation totals during Jul–Nov 1999. Ranks are based on total precipitation during the above periods from 1895–1999. A rank of 1 indicates that statewide rainfall during 1999 was the lowest in the historical record dating back to 1895.

and Halpert 1989). The most significant dryness during 1999 (25%–50% of normal) occurred in southeastern Oahu, central and southern Maui, most of Molokai and Lanai, and western sections of Hawaii Island. Elsewhere, near- or above-normal rainfall totals were confined to much of Kauai, west-central Oahu, the higher elevations of eastern Oahu, northwestern Maui, and eastern Hawaii Island.

Rainfall totals from late 1997 through 1999 were exceptionally low at many locations, including southern and western Oahu, central and southwestern Maui, Molokai (Fig. 44a), Lanai, and southern and western parts of the Big Island, all of which received less than half of normal rainfall during 1998–99. In Honolulu, total rainfall during 1998 and 1999 was 412 mm (Fig. 44b), which is the lowest amount at this site for any two consecutive calendar years since reliable records began in 1947. This total is also more than 100 mm below the previous record low value of 524 mm set during 1952–53. Accumulated precipitation shortfalls during 1998–99 were also large across windward sections of Hawaii Island, where normals are typically extremely large. For example, Laupahoeh, in northeastern Hawaii Island, recorded 4450 mm of rain during 1998 and 1999, which is more than 3000 mm below the long-term average.

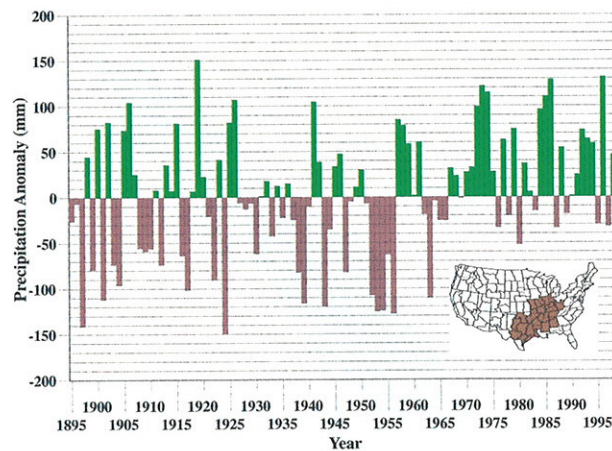


FIG. 43. Time series from 1895–1999 of area-averaged precipitation anomalies (mm) during Jul–Nov for the area shown shaded in the inset. Anomalies are departures from the 1895–1999 base period means.

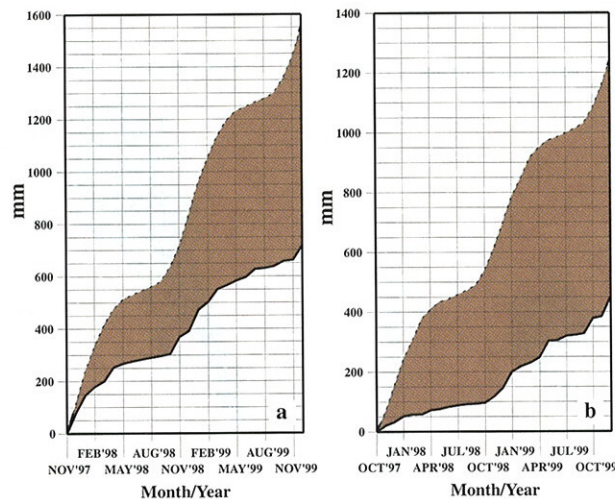


FIG. 44. Oct 1997–Dec 1999 accumulated observed precipitation (solid) and accumulated climatological mean precipitation (dashed, 1961–90 base period mean) at (a) Molokai, Hawaii, and (b) Honolulu, Hawaii. Shading shows the accumulated negative departure from normal.

#### b. Africa

##### 1) THE 1998–99 SOUTHERN AFRICA RAINY SEASON

Southern Africa receives the bulk of its mean annual rainfall during October to April, with the largest totals typically observed between December and March. The climatologically wet region of southeastern Africa tends to be drier than average during El Niño episodes, and wetter than average during La Niña episodes (Ropelewski and Halpert 1987, 1989, 1996; Janowiak 1988; Hastenrath 1995; Dai et al. 1997). Overall, the 1998–99 rainy season was



characterized by significant rains across much of southeastern Africa (Figs. 45a,b), and by drier-than-normal conditions over much of interior southern Africa. The season also featured an early onset of the rains in October and November 1998 and an early withdrawal of the rains in March and April 1999 (Fig. 45d). The overall wetness over southeastern Africa was consistent with the ongoing La Niña episode and is in contrast to the below-normal to near-normal rainfall observed in this region during the 1997–98 rainy season in association with El Niño conditions.

Regionally, 1998–99 seasonal rainfall totals were near normal to above normal over much of Mozambique, southern and central Malawi, eastern Zimbabwe, the Northern Transvaal, Kwazulu/Natal, and eastern cape provinces of South Africa. Rainfall totals in these areas averaged between 500 and 900 mm. Accumulated rainfall and daily rainfall totals during the season are shown for two reporting stations within these wetter-than-average regions: Pietersburg, South Africa (Fig. 46a), and Harare, Zimbabwe (Fig. 47a). Rainfall at both stations occurred almost on a daily basis from November 1998 through January 1999 (Figs. 46b, 47b). Harare also experienced substantial rainfall during most of February and again in mid-March. In contrast, the rains at Pietersburg ended in late January, with only episodic, light rain observed after that. Only minimal rainfall was observed at both stations during late March and April.

The climatologically dry regions of southwestern and south-central Africa received near-normal to significantly below-normal precipitation during the 1998–99 rainy season (Figs. 45b,c). For example, near-normal rainfall was observed over Swaziland and Lesotho, and below-normal rainfall was recorded over portions of the Free State and North-West Province of South Africa, and across southern Botswana westward into Namibia. Elsewhere, exceptionally dry conditions were observed in the desert regions of central Namibia and southwestern Botswana, where rainfall totals less than 100 mm were only in the 5–10th percentile (Fig. 45c).

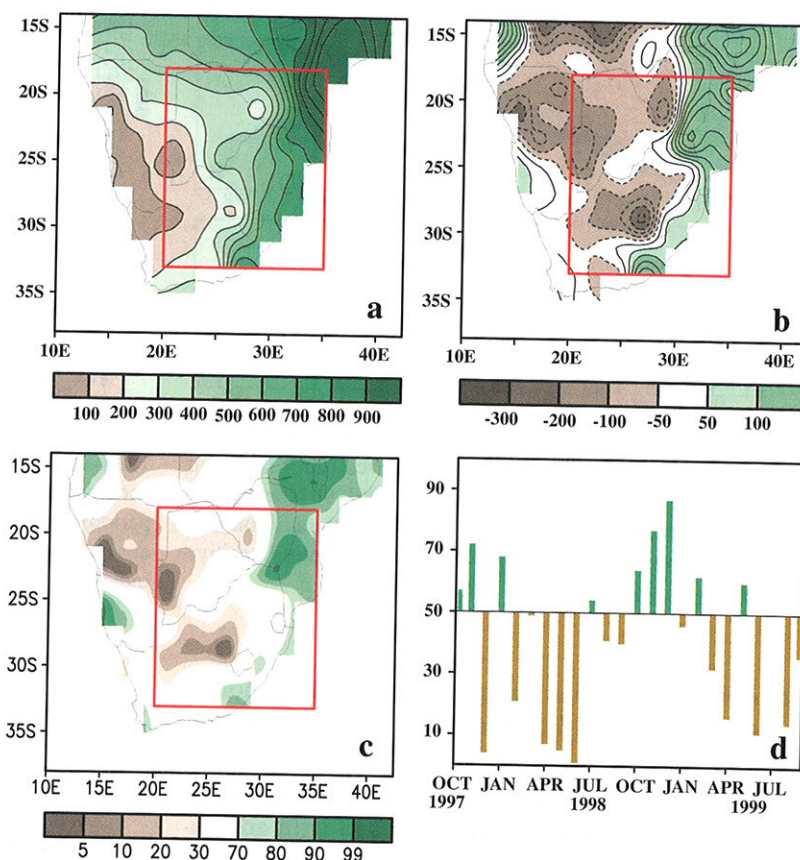


FIG. 45. Oct 1998–Apr 1999 (a) total precipitation (mm), (b) precipitation anomalies (mm), (c) precipitation percentiles based on a gamma distribution fit to the 1961–90 base period. Panel (d) shows a monthly time series of precipitation percentiles, based on precipitation totals averaged over the boxed region depicted in panels (a)–(c).

Overall, the low-level atmospheric circulation for the 1998–99 rainy season featured easterly winds that averaged  $4\text{--}8\text{ m s}^{-1}$  from the eastern Indian Ocean westward to Madagascar and across portions of interior southern Africa (Fig. 48a). Over the Indian Ocean, this easterly flow was found along the poleward flank of the Mascarene high pressure system. A notable break in this easterly flow was evident in the region between southern Africa and Madagascar, which experienced only weak low-level easterlies during the season.

The primary anomalous circulation during the season occurred during DJF (Fig. 48b), in association with a pronounced amplification and poleward shift of the low-level Mascarene high across the western and central Indian Ocean. This anomaly feature was accompanied by enhanced easterlies between  $10^{\circ}$  and  $20^{\circ}\text{S}$  across the central and western Indian Ocean, and with anomalous poleward flow in the region between Madagascar and Mozambique. Farther west, an anomalous cyclonic circulation was evident over in-



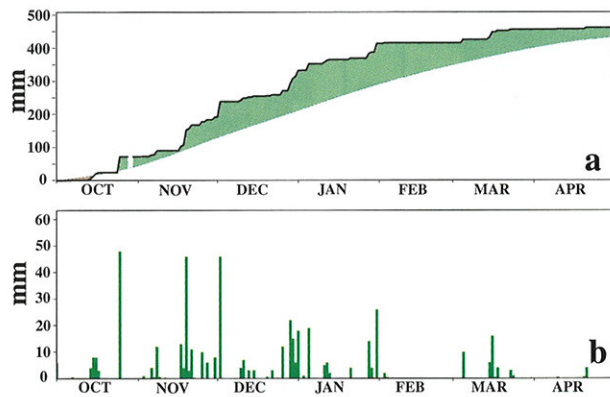


FIG. 46. Daily rainfall (mm) at Pietersburg, South Africa, during Oct 1998–Apr 1999: (a) accumulated observed (thick line) and accumulated climatological mean (thin line, 1961–90 base period), and (b) observed daily total. Shading in (a) shows the accumulated departure from normal, with green shading indicating positive departures.

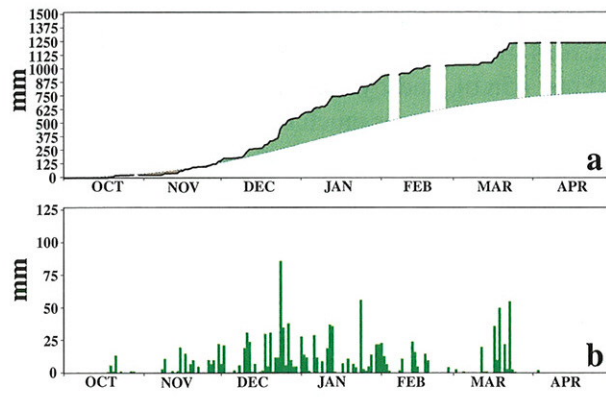


FIG. 47. Daily rainfall (mm) at Harare, Zimbabwe, during Oct 1998–Apr 1999: (a) accumulated observed (thick line) and accumulated climatological mean (thin line, 1961–90 base period), and (b) observed daily total. Shading in (a) shows the accumulated departure from normal, with green shading indicating positive departures, and breaks indicating missing data.

terior southern Africa during the period, with anomalous westerly flow found near  $15^{\circ}\text{S}$  along the northern flank of this circulation. Overall, these conditions were associated with confluence extending southwestward along the Mozambique coast and with anomalous large-scale convergence across southeastern Africa and the Mozambique Channel. These circulation features were accompanied by an anomalous anticyclonic circulation at upper levels in association with an amplification/southward shift of subtropical ridge. Collectively, these conditions represented an enhanced monsoonal circulation over southeastern Africa, and were consistent with the above-average rainfall observed during the period. At upper levels this anomaly pattern was linked to the much larger-scale pattern of anticyclonic streamfunction anomalies previously noted in the lower and middle latitudes of both hemispheres [see section 3e(2)].

## 2) JUNE–SEPTEMBER 1999: WESTERN AFRICA RAINY SEASON

The Sahel region (bounded by  $8^{\circ}$ – $18^{\circ}\text{N}$ ,  $18^{\circ}\text{W}$ – $20^{\circ}\text{E}$  and indicated by the boxed region in Fig. 49) receives approximately 90% of its mean annual rainfall during the June–September period. This rainfall pattern is closely related to the intertropical convergence zone (ITCZ), which starts its northward movement in March and reaches its northernmost position (near  $15^{\circ}\text{N}$ ) in August. Rainfall typically varies widely across the region, with long-term average totals reaching 1300 mm in the southwest, 700 mm in the southeast, and 100–300 mm in the north.

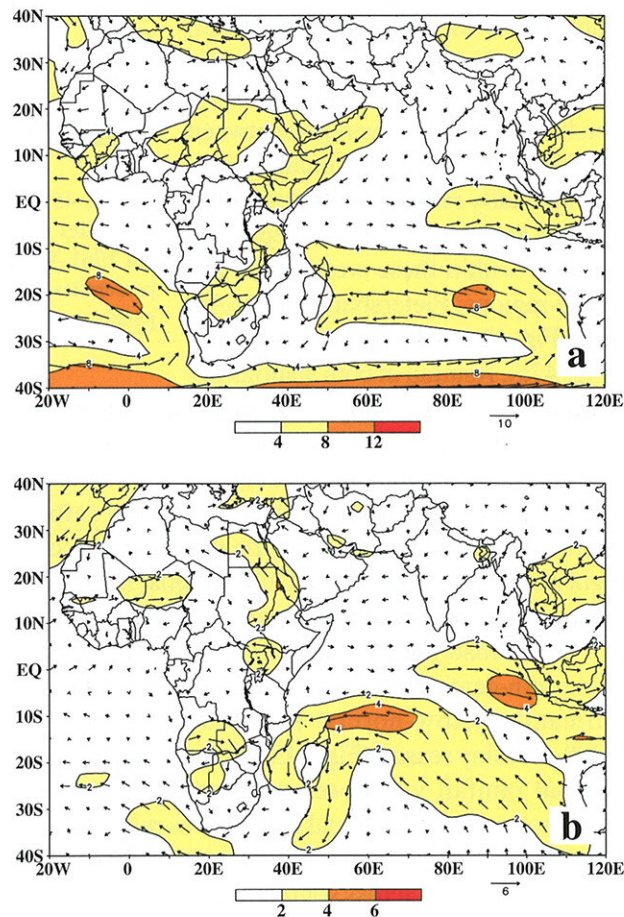


FIG. 48. 850-hPa zonal wind for (a) Oct 1998–Apr 1999 and (b) DJF 1998–99 zonal wind anomalies. Anomalies are departures from the 1979–95 base period means.



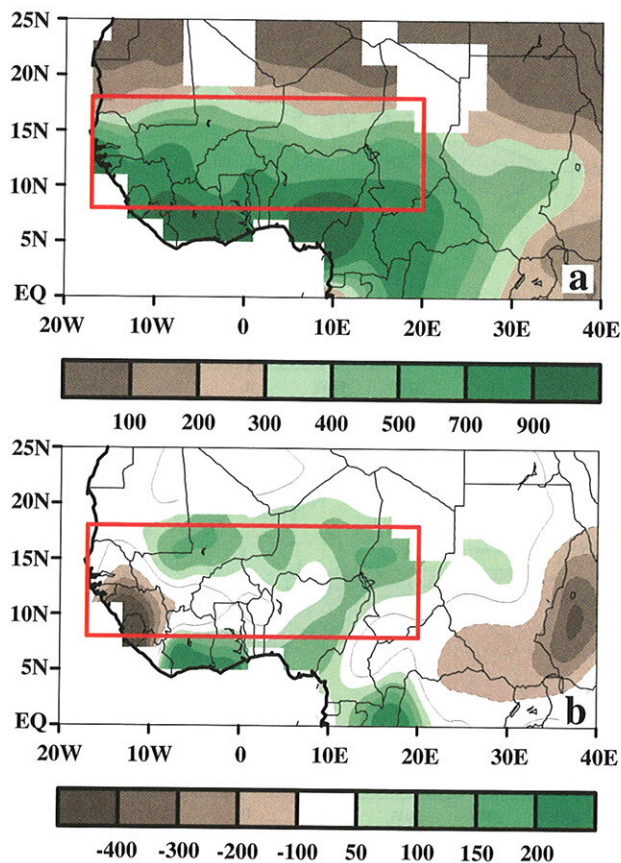


FIG. 49. Jun–Sep 1999 (a) total precipitation (mm) and (b) anomalies (mm) for the African Sahel region. The boxed region denotes the approximate boundaries of the West African Sahel region.

Overall, the Sahel experienced an exceptionally wet rainy season during 1999 (Fig. 49), with area-averaged totals reaching the highest levels since 1967 (Fig. 50). These plentiful rains followed a near-average 1998 rainy season and suppressed 1997 rainy season. Wetter-than-normal precipitation was observed primarily across the northern portion of the Sahel during 1999 (Fig. 49b) and near-average totals were observed in the south. The only part of western Africa that experienced below-average rainfall during the season was the southwestern Sahel area, which recorded totals that were approximately 400 mm below the 1961–90 mean. However, this area still recorded more than 900 mm of rain during the season.

The atmospheric circulation during the 1999 season featured a strong southerly and southwesterly flow of tropical moisture at 925 hPa into the Sahel region (Fig. 51) as well as a significant penetration of moist, southwesterly flow into the northern part of the Sahel. The largest wind anomalies at 925 hPa were observed

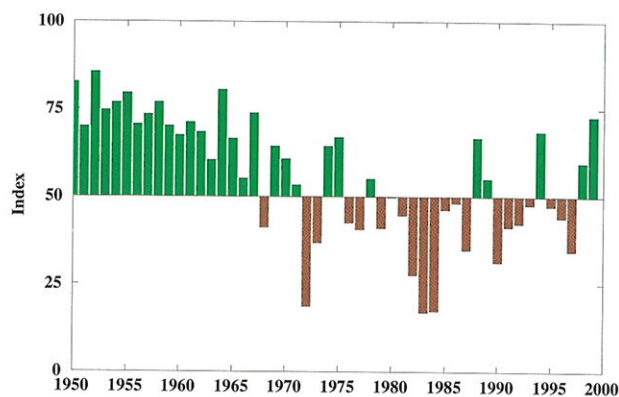


FIG. 50. Percentile index (average gamma percentiles of station precipitation within region) for the African Sahel during Jun–Sep. Percentiles are computed for the 1961–90 base period.

over the western Sahel (Fig. 52a) where westerly anomalies averaging  $1\text{--}3\text{ m s}^{-1}$  extended well inland from the eastern tropical Atlantic Ocean. This enhanced monsoonal flow was even more prominent at 850 hPa (Fig. 52b) where westerly wind anomalies averaging  $2\text{--}4\text{ m s}^{-1}$  extended from the eastern tropical Atlantic eastward to the southwestern Sahel and across the entire Gulf of Guinea. This anomalous flow was associated with enhanced cyclonic vorticity along the equatorward flank of the African easterly jet (AEJ) [see section 4a(2), Fig. 31d] and with enhanced low-level convergence over much of the Sahel.

These low-level circulation features were associated with an overall poleward shift of the AEJ and with a strengthening of the upper-level jet or tropical easterly jet (TEJ) from the eastern Pacific eastward to Indonesia (Figs. 17c, 30a). All of these conditions typify other wet Sahel years as well.

During 1999, the regional conditions that contributed to abundant Sahel rains were linked to a global-scale atmospheric circulation pattern characterized by an amplification and poleward extension/shift of the subtropical ridges in both hemispheres from the eastern Pacific eastward across the Atlantic and Africa to Australasia (Fig. 23c). As discussed in section 3e(2), this global-scale mode of atmospheric variability was associated with the La Niña-related pattern of tropical rainfall shown in Figs. 17 and 19.

### c. Asia

#### 1) INDIAN SUMMER MONSOON

The Indian subcontinent lies along the western flank of the Southeast Asian summer monsoon system and receives most of its annual rainfall during June–September. Climatologically, two rainfall



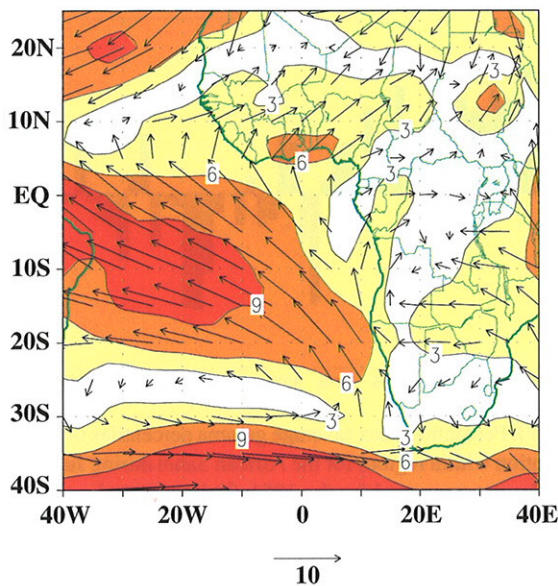


FIG. 51. 925-hPa wind speed ( $\text{m s}^{-1}$ ) and vector wind during Jun–Sep 1999.

maxima with totals exceeding 1200 mm are observed over India and the surrounding Indian Ocean during the monsoon season (Fig. 53a). The first maximum is centered over the Bay of Bengal and extends north-westward into eastern and central India. The second maximum is located along the west coast of India on the windward side of the Western Ghats Mountains. A relative minimum in rainfall of less than 500 mm is found in the climatological mean between these two regions in the southeastern state of Tamil Nadu. Relatively low climatological rainfall totals of 400–600 mm are also observed across northern India, while the lowest totals (200–400 mm) are observed in north-western India in the vicinity of the Great Indian Desert.

During the 1999 monsoon season, precipitation was below average for the Indian subcontinent as a whole (Fig. 53b), with much of the rainfall deficit observed during July and August (Fig. 53c). The largest precipitation deficits were observed along the west coast, in the northwest, and in the south. However, the percent of normal seasonal mean precipitation (not shown) varied considerably along the west coast with approximately one-third of normal rainfall recorded in Surat (north of Bombay) and 125% of normal rainfall observed in Mangalore (south of Bombay). Elsewhere, above-average rainfall was observed over portions of northeastern India with departures exceeding 200 mm in some locations (Fig. 53b).

Also during 1999, eastern India was affected in late October by two major tropical cyclones, which moved

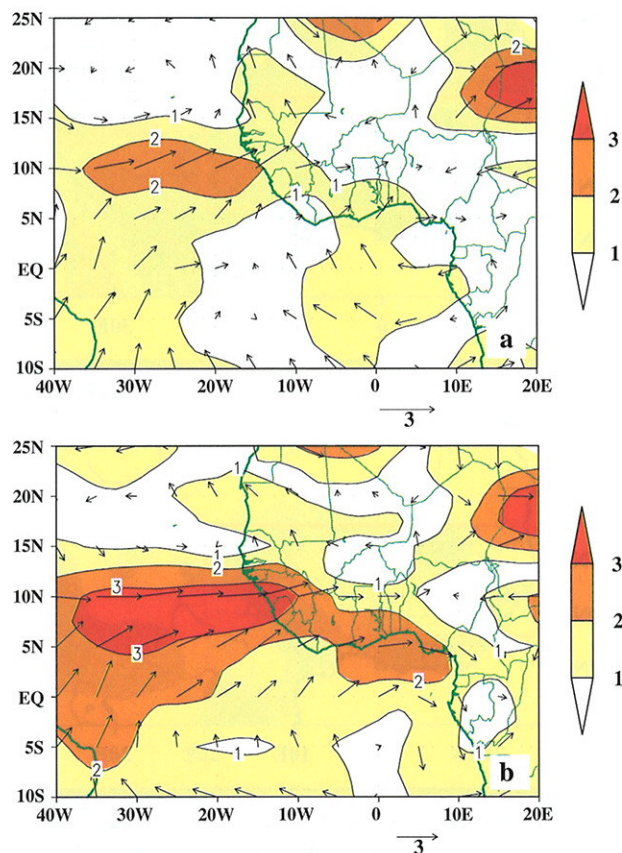


FIG. 52. Anomalous wind speed ( $\text{m s}^{-1}$ ) and anomalous vector wind during Jun–Sep 1999 at (a) 925 hPa and (b) 850 hPa. Anomalies are departures from the 1979–95 base period means.

inland from the Bay of Bengal with maximum sustained winds of up to 300 kph (190 mph). The largest impacts from these cyclones were felt in the state of Orissa, located near  $20^\circ\text{N}$  in eastern India. Approximately 10 million people were left homeless from these cyclones, with millions also losing their crops and their access to clean water and health services. The human death toll from these cyclones was estimated to be over 10 000, and the cattle death toll was estimated at 175 000.

Historically, above- (below) average Indian monsoon rainfall has been generally associated with the cold (warm) phase of the ENSO. However, Krishna Kumar et al. (1999) note that this relationship has become markedly less clear since the 1980s. Recent examples of this unclear relationship between Indian rainfall and the ENSO cycle include the above-average 1997 rainy season that occurred during strong El Niño conditions, and the below-average 1999 rainy season that occurred during La Niña conditions.

In contrast to Indian rainfall alone, the overall India/Asia monsoon circulation does exhibit a fairly



strong relationship with the ENSO cycle. Perhaps one of the most important components of this circulation is the upper-level monsoon ridge, which reflects the overall strength of the entire southeast Asian monsoon complex and not simply rainfall over India. This monsoon ridge tends to be suppressed during significant El Niño episodes and enhanced during La Niña episodes. For example, the monsoon ridge was particularly suppressed during the 1997 season when strong El Niño conditions were present (Fig. 54a). In contrast, it was enhanced and extended westward during both the 1998 (Fig. 54b) and 1999 monsoon seasons (Fig. 54c) in association with La Niña conditions. These coherent variations in the Asian monsoon ridge were also evident in the subtropics of both hemispheres extending from the eastern Pacific eastward to Australasia. As noted in section 3e(2), this large-scale anomaly pattern represents the leading mode of atmospheric variability on both interannual and interdecadal timescales (Mo and Kousky 1993).

## 2) CENTRAL CHINA RAINFALL

The largest rainfall totals across central China (indicated by the red, boxed region in Fig. 53b) typically occur between April and September (black curve, Fig. 53d) with an area-averaged peak total approaching 190 mm in June. Overall, rainfall in this region was well above average during April–September 1999 (Fig. 53b) with above-normal totals observed in every month except September (Fig. 53d). The increased rainfall was observed primarily across the eastern and southern portions of central China, with the largest anomalies exceeding 400 mm in the east. This above-average rainfall was associated with a much larger area of increased precipitation that covered the western tropical and subtropical North Pacific, the entire South China Sea, Indonesia, and the eastern half of the equatorial Indian Ocean (see section 3, Fig. 15).

### d. South America

Typical La Niña-related impacts in South America include wetter-than-normal conditions over the Amazon basin and northern South America, and drier-than-normal conditions over southern Brazil, Uruguay, and

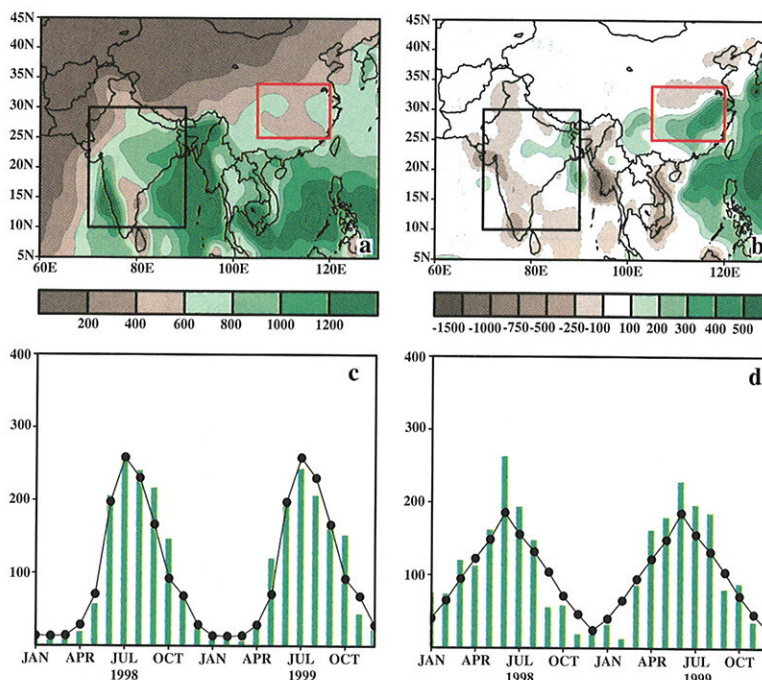


FIG. 53. (a) Climatological mean precipitation (mm) and (b) precipitation anomalies (mm) for Jun–Sep 1999. Monthly time series of total precipitation (mm, bars) and the 1961–90 mean (mm, line) averaged over (c) the boxed region centered on India and (d) the boxed region centered on eastern China.

northeastern Argentina (Aceituno 1988; Ropelewski and Halpert 1989). These average features display considerable seasonality with the wetter-than-normal conditions extending into northeast Brazil during March–May and being confined to extreme northern South America during September–December, and the drier-than-normal conditions farther south being most prominent from September–December.

Many of the precipitation anomalies observed over South America during 1999 (Fig. 55) are consistent with those recorded during past cold episodes. Above-average precipitation was observed over the Amazon basin during DJF 1998–99 and MAM 1999 (Figs. 55a,b) and over extreme northern South America throughout the year.

In northern Venezuela the persistent pattern of above-normal rainfall resulted in saturated soil conditions and was a contributing factor in producing the devastating floods and landslides in that country during 14–17 December 1999. High-resolution experimental satellite estimates of precipitation during 15–17 December indicate that up to 475 mm fell in coastal sections near Caracas (R. Scofield, NESDIS, 1999, personal communication). Local observations (L. Hidalgo 1999, personal communication) indicate that in the vicinity of the coast and along the slopes of



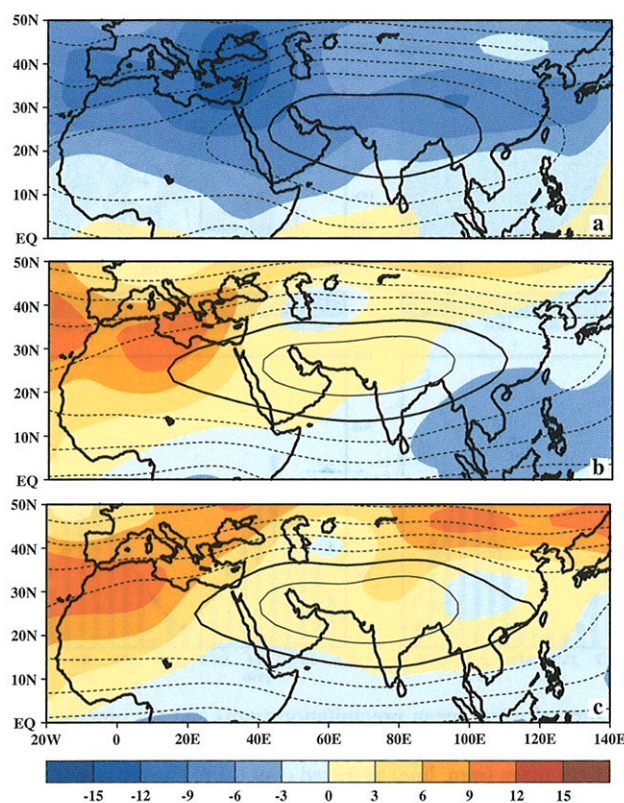


FIG. 54. 200-hPa streamfunction (contours) and anomalies (shading) during (a) Jul–Sep 1997, (b) Jul–Sep 1998 and (c) Jul–Sep 1999. Units are  $1.0 \times 10^6 \text{ m}^2 \text{ s}^{-1}$ . Contour interval is 10. Anomalies are departures from the 1979–95 base period means.

the coastal mountains rainfall totals may have been up to twice as large as the satellite estimates.

Farther south, rainfall deficits accumulated substantially during SON over southern Brazil, Paraguay, Uruguay (Fig. 57a), and also over northeastern Argentina (Fig. 57b), consistent with La Niña-related conditions. Rainfall deficits for the season exceeded 200 mm in portions of these regions (Figs. 55d, 57).

In other parts of northern South America, the observed rainfall pattern during 1999 deviated from that expected during cold episodes. For example, coastal Ecuador and northern Peru experienced above-average rainfall during DJF 1998–99 (Fig. 56a), while portions of northeastern Brazil experienced rainfall deficits during DJF and MAM (Figs. 56a,b).

#### e. Storminess across central Europe

##### 1) EXCESSIVE JANUARY–FEBRUARY SNOW

Much of the Alps region of central and eastern Europe recorded well above-average wintertime precipitation during late January–February, which led to

a series of deadly avalanches in France, Switzerland, Austria, and Italy. In many areas, this precipitation led to snowfall totals that were the highest in 50 years. This excessive snowfall, combined with alternating warm and cold spells, led to unstable snow packs at higher elevations as the top layers of snow thawed and refroze, thus becoming more compact and dense than the underlying powdery snow. These conditions ultimately culminated in the deadly avalanches.

The excessive snowfall resulted from a series of four major storms that impacted central and eastern Europe during the period, as highlighted by the time series of liquid equivalent precipitation at St. Anton, Austria (Fig. 58). During each of these storms the precipitation was associated with extremely heavy snowfall, with substantial snowfall occurring every day between 16 and 26 February in association with the last two storms.

St. Anton is located less than 20 km from the mountainous ski resort of Galtür, which was the site of several landslides during February. One of these landslides, which devastated the resort on 24 February, resulted from the buildup of an exceptionally large and unstable slab of snow above the town. This slab was estimated to have weighed 170 000 tons and to have sped downhill at  $83 \text{ m s}^{-1}$ , taking less than one minute to reach the valley floor (L. Malone, WMO, 2000, personal communication).

The 700-hPa heights and wind speeds (Fig. 59) associated with each of the four storms on the day of heaviest precipitation at St. Anton (28 January, 7 February, 17 February, and 24 February) indicate that the precipitation was related primarily to very strong upslope flow in the region upstream of a major amplifying trough. The first two of these storms (Figs. 59a,b) eventually became classic Genoa cyclogenesis events (Mattocks and Bleck 1986; Bell and Bosart 1994) featuring a closed cyclonic circulation at upper levels over central/southern Italy. The last two storms (Figs. 59c,d) were centered over eastern Europe and also brought heavy precipitation to that region.

These four storms occurred within a mean flow characterized by a diffluent trough extending southward across central Europe and a large-amplitude ridge over the eastern North Atlantic (Fig. 60). The jet stream winds were highly asymmetric with respect to the trough axis, with the strongest meridional (northwesterly) flow located between the ridge and downstream trough axes. This circulation favored a situation whereby transient shortwave trough/jet streak systems



propagated through the ridge axis and subsequently amplified as they approached the downstream diffluent trough. In the first two storms, cyclogenesis was also aided in the southern lee of the Alps by low static stability air at lower levels of the atmosphere, which is typically observed in that region due to the proximity of the Mediterranean Sea and the confinement of deep, cold air masses to the region north of the Alps.

## 2) DECEMBER WIND STORMS

Extremely strong (hurricane force) winds were observed over large parts of Europe during December 1999 in association with a series of severe storms. These storms caused more than 100 deaths and billions of dollars (\$US) in damage. Also, numerous buildings and vast areas of forest were destroyed by the winds, and transport and power outages were common and lasted for days. In perhaps one of the most unfortunate instances of tree damage, several hundred extremely old trees were destroyed at the palace of Versailles, France, in late December by the extremely strong winds.

The first major wind storm hit Europe on 3 December and affected Denmark, northern Germany, southern Sweden, and the Baltic states. Locally, Denmark was hit with wind speeds reaching  $37 \text{ m s}^{-1}$  and the Island of Romo recorded gusts of  $51 \text{ m s}^{-1}$ . A second major wind storm on 26 December brought  $42 \text{ m s}^{-1}$  sustained winds to northern France (Fig. 61b), south-

ern Germany, and Switzerland. In the mountains, many stations recorded sustained wind speeds exceeding  $55 \text{ m s}^{-1}$ . Extreme winds and heavy rains also ravaged southern France on 27–28 December (Fig. 61b), with speeds exceeding  $33 \text{ m s}^{-1}$  throughout the region.

These strong wind storms were associated with a very powerful Atlantic jet stream that extended across the eastern North Atlantic and into western Europe during the month (Fig. 61a). This enhanced jet stream

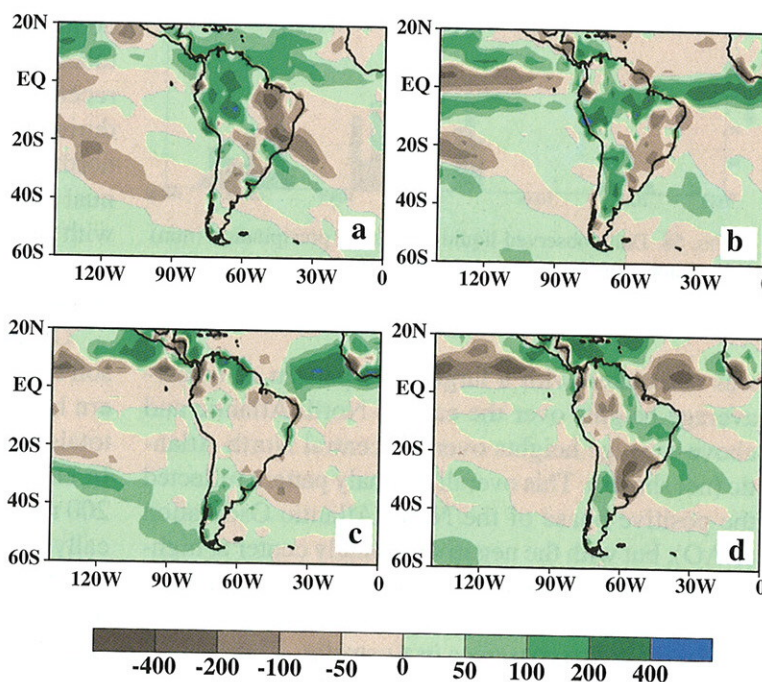


FIG. 55. Precipitation anomalies during (a) DJF 1998–99, (b) MAM 1999, (c) JJA 1999, and (d) SON 1999. Anomalies are departures from the 1979–95 base period means.

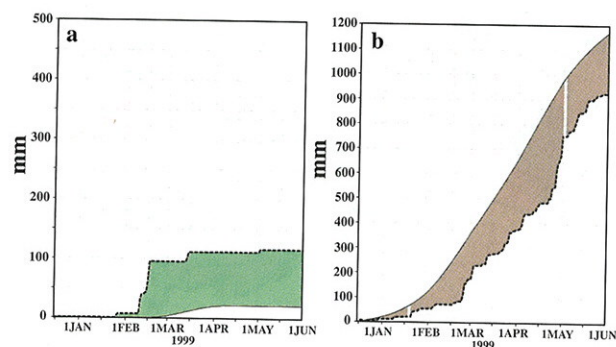


FIG. 56. 16 Dec 1998–1 Jun 1999 accumulated observed (thick line) and accumulated climatological mean (thin line, 1961–90 base period) rainfall totals (mm) at (a) Talara, Peru, and (b) Fortaleza, Brazil. Shading shows the accumulated departure from normal, with green shading indicating positive departures and brown shading indicating negative departures.

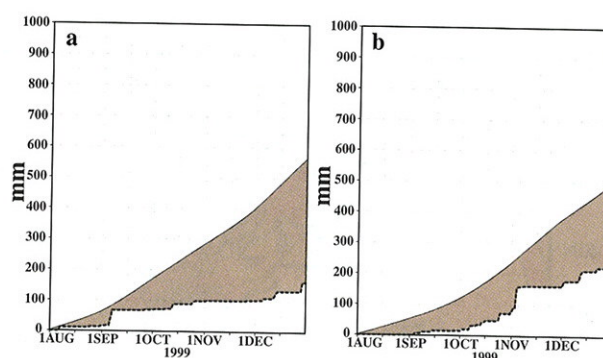


FIG. 57. 1 Aug 1999–31 Dec 1999 accumulated observed (thick line) and accumulated climatological mean (thin line, 1961–90 base period) rainfall totals (mm) at (a) Salto, Uruguay, and (b) Resistencia, Argentina. Shading shows the accumulated departure from normal, with brown shading indicating negative departures.



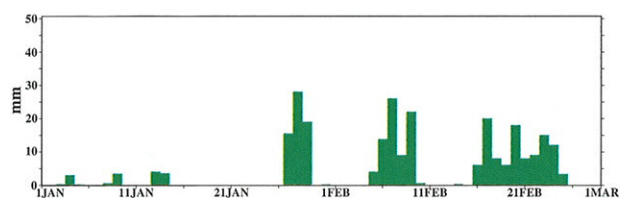


FIG. 58. Daily observed liquid equivalent precipitation (mm) at St. Anton, Austria, during Jan–Feb 1999.

was associated with a large-scale pattern of below-average heights over the eastern North Atlantic and above-average heights over the central North Atlantic (not shown). This overall anomaly pattern reflected the positive phase of the North Atlantic Oscillation (NAO), but with the negative anomaly center at high-latitudes shifted from Iceland toward Scandinavia.

#### f. Precipitation extremes in Australia

##### 1) NORTHERN AND NORTHWESTERN AUSTRALIA

Northern Australia (indicated by the boxed area in Fig. 62a) experiences a tropical climate with a well-

defined rainy season that typically begins during October and ends in April (Fig. 62c). Much of the area receives more than 75% of its mean annual rainfall during this 7-month period, with portions of extreme northern Australia recording more than 90%. This annual cycle is modulated by the Southern Oscillation with below- (above) average rainfall often observed during Pacific warm (cold) episodes (Ropelewski and Halpert 1987, 1989).

Overall, the October 1998–April 1999 rainy season featured above-average rainfall across the northern half of northern Australia (Fig. 62a) with record totals observed in portions of northwestern Australia. In each of these regions, totals averaged more than 200 mm above normal during the season with the locally extreme totals in some areas leading to significant flooding. In northern Australia rainfall was above average in every month of the season except January (Fig. 62c, green bars), with particularly excessive totals observed in November–December 1998 and in March–April 1999. The increased rainfall in December, March, and April was partly associated with a se-

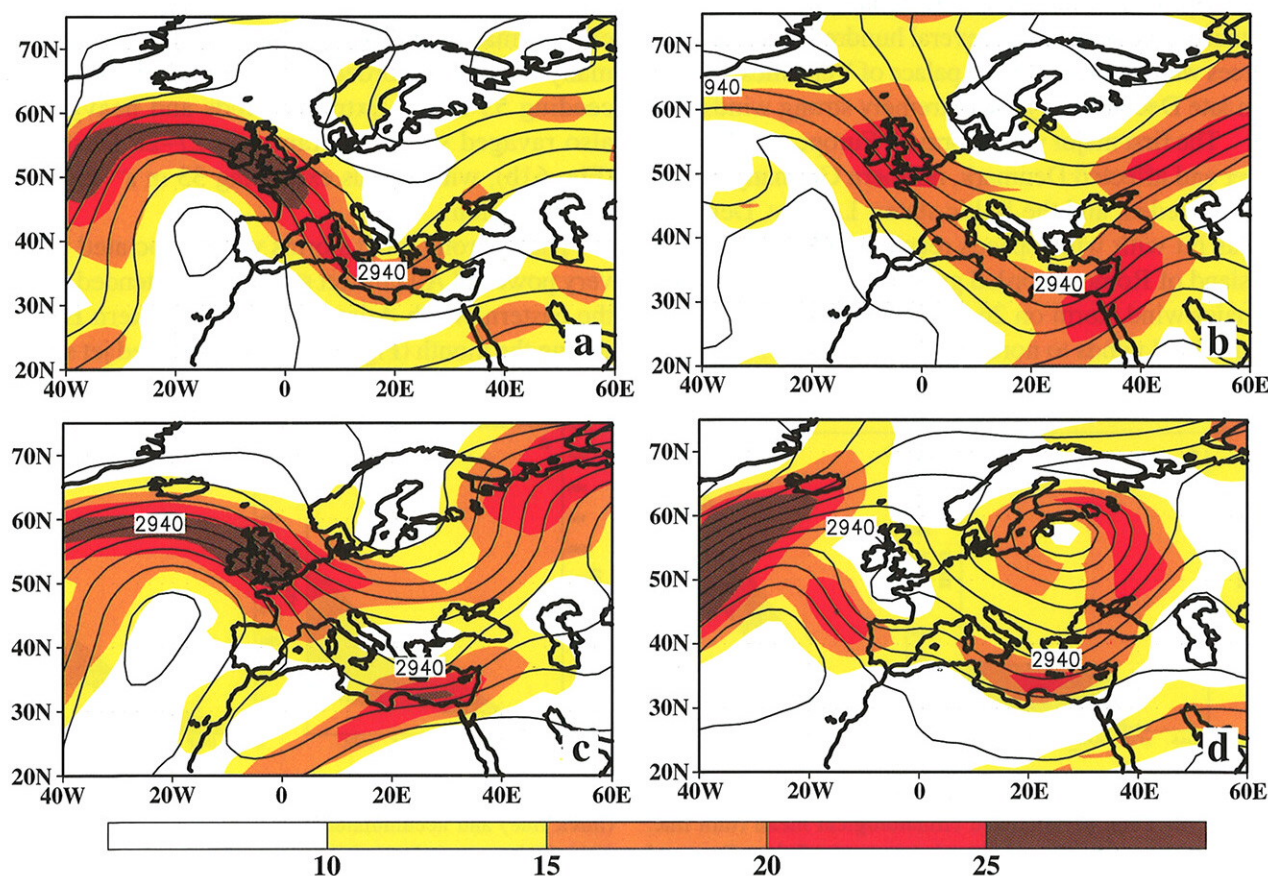


FIG. 59. 700-hPa heights (contours, interval is 60 m) and wind speeds (shaded,  $\text{m s}^{-1}$ ) on (a) 28 Jan 1999, (b) 7 Feb 1999, (c) 17 Feb 1999, and (d) 24 Feb 1999.



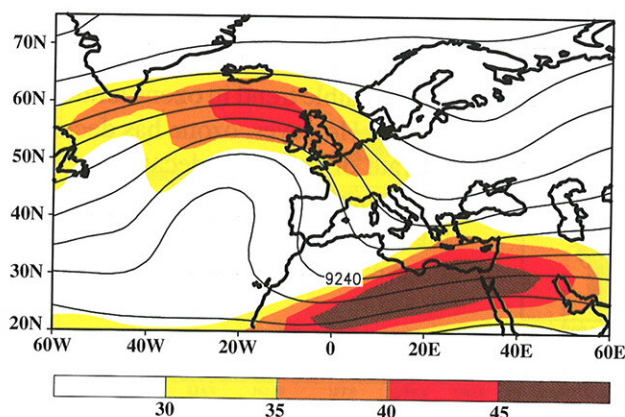


FIG. 60. Mean 300-hPa heights (contours, interval is 120 m) and wind speeds (shaded,  $\text{m s}^{-1}$ ) during Feb 1999.

ries of five tropical cyclones (TC), which included TC Thelma in December, TC Rona in February, TC Vance in March, TC Elaine in March, and TC Gwenda in April. These systems, with the exception of TC Rona, also produced copious rainfall totals over portions of western Australia.

At Darwin, Australia, indicated by the yellow dot in Fig. 62a, seasonal rainfall totals reached 2250 mm (Fig. 63a), which approached the record total of 2499 mm observed during the previous record 1997/98 wet season (Bell et al. 1999). The largest rainfall event during the 1998/99 season at this station was a 2-day total of 420 mm, in association with category-5 TC Thelma in December 1998 (Fig. 63b). This single rainfall event contributed to more than half of the total seasonal anomaly of 750 mm. Darwin also recorded measurable rainfall nearly every day from January to mid-April, with several substantial rain events (totals reaching 50 mm each) observed during the period.

In northwestern Australia 1998/99 seasonal rainfall totals at Wittendom Gorge (Fig. 64), location indicated by the red dot in Fig. 62a, reached 850 mm (Fig. 64a). This total is 525 mm, and 260%, larger than the climatological mean. Most of this excess rainfall resulted from three major precipitation events (Fig. 64b), two of which occurred in February and one of which occurred in mid-March in association with TC Elaine.

## 2) SOUTHEASTERN AUSTRALIA

Significantly below-average rainfall was observed over southeastern Australia (indicated by the boxed region in Fig. 62b) from April 1999 through the end of the year (Fig. 62d). Rainfall was below average during every month of this period (Fig. 62d) with the most significant deficits observed during June–December.

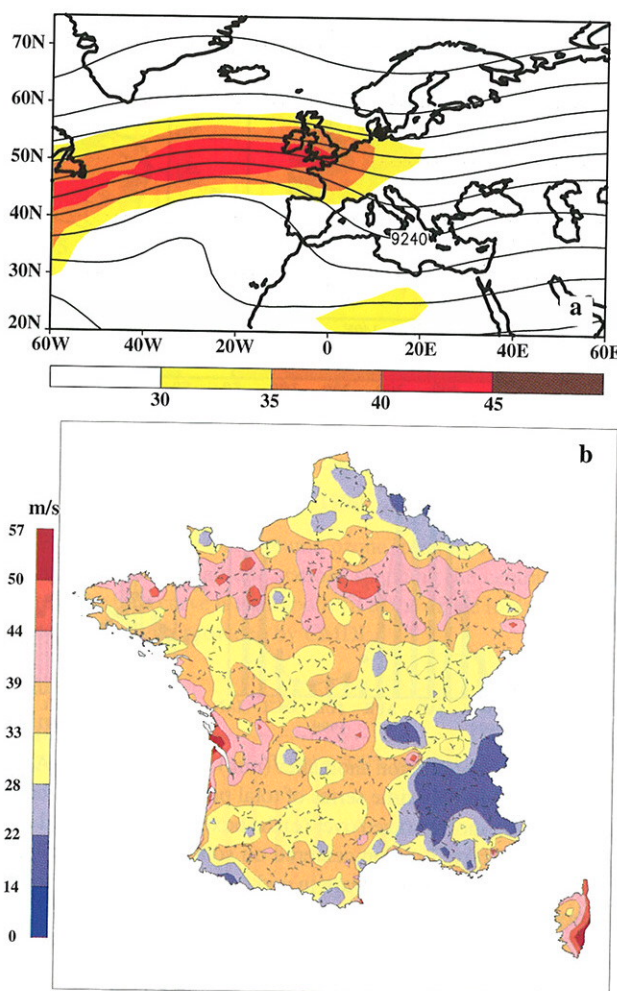


FIG. 61. (a) Mean 300-hPa heights (contours, interval is 120 m) and wind speeds (shaded,  $\text{m s}^{-1}$ ) during Dec 1999 and (b) maximum sustained wind speeds ( $\text{m s}^{-1}$ ) recorded in France during 26–28 Dec 1999 at elevations below 500 m. [Analysis in (b) provided by Météo France.]

Overall, totals during this period were generally more than 200 mm below average across nearly all of Victoria, which includes major cities such as Melbourne and Sydney. The state of Victoria has recorded significantly below-average rainfall since late 1996, with December 1996–December 1999 deficits exceeding 500 mm throughout the region. These long-term moisture deficits have led to severe drought over most of southeastern Australia.

## 5. Trace gases

### a. Ozone

#### 1) CONTINENTAL UNITED STATES AND HAWAII

The NOAA Climate Monitoring and Diagnostics Laboratory (CMDL), in cooperation with several other



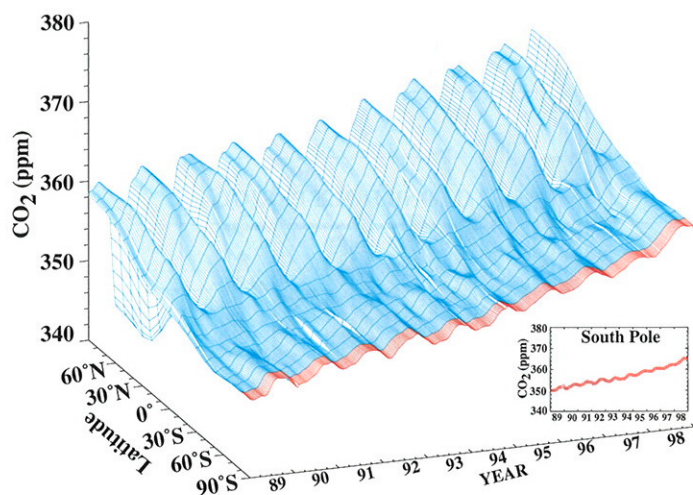


FIG. 70. Three-dimensional representation of the latitudinal distribution of atmospheric carbon dioxide ( $\text{CO}_2$ ) in the marine boundary layer based on measurements from the NOAA/CMDL cooperative air sampling network. Measurements from South Pole are shown in red. (Analysis provided by CMDL.)

north-south gradient is strongest in spring when respired  $\text{CO}_2$  has accumulated in the atmosphere. Carbon cycle models attempt to reproduce this measured distribution by combining source/sink functions with atmospheric transport models, while inversion techniques combine the data with a transport model to deduce sources and sinks.

## 2) METHANE

Methane contributes about 20% of the direct radiative forcing attributed to those long-lived greenhouse gases that are directly affected by human activities. Changes in the burden of methane also feed back into atmospheric chemistry and indirectly affect climate by influencing other greenhouse gases such as tropospheric  $\text{O}_3$ , stratospheric  $\text{H}_2\text{O}$ , and the concentration of  $\text{OH}$ . These indirect effects are estimated to add ~40% to the direct climate effect of methane (Lelieveld et al. 1993). It is suggested that reducing methane emissions to the atmosphere would decrease its potential effect on climate. However, before reasonable policies can be developed to reduce  $\text{CH}_4$  emissions, its budget of sources and sinks must be better understood.

High-precision measurements of atmospheric methane indicate that approximately 70% of  $\text{CH}_4$  emissions are in the Northern Hemisphere. As a result, methane concentra-

tions are also higher in that hemisphere, with the largest concentrations observed at higher latitudes (Fig. 71). There is a strong seasonal cycle to methane concentrations throughout the globe, with a particularly regular seasonal cycle observed in the high latitudes of the Southern Hemisphere (see inset Fig. 71). In the Northern Hemisphere middle and high latitudes ( $30^\circ$ – $90^\circ\text{N}$ ), the seasonal cycle features a peak in  $\text{CH}_4$  concentrations from mid-January through mid-February (Fig. 72a, blue curve) and a minimum concentration in April.

There is also an upward trend in  $\text{CH}_4$  concentrations through the globe, with a deseasonalized trend in the Northern Hemisphere extratropics of  $8.0 \text{ ppb yr}^{-1}$  evident between 1984 and 1998 (black curve, Fig. 72a). However, the instantaneous growth rate of methane in this region, determined as the derivative of the trend line (Fig. 72b), has decreased by  $0.9 \text{ ppb yr}^{-1}$ .

Superimposed upon this long-term decrease in growth rate are significant interannual variations. One outstanding feature is the large increase in growth rate during 1998, possibly related to increased  $\text{CH}_4$  emissions from wetlands due to anomalously warm temperatures in that year. This suggests that changes in climate could have a large impact on  $\text{CH}_4$  emissions, and, therefore, on the contribution of methane to earth's radiative budget.

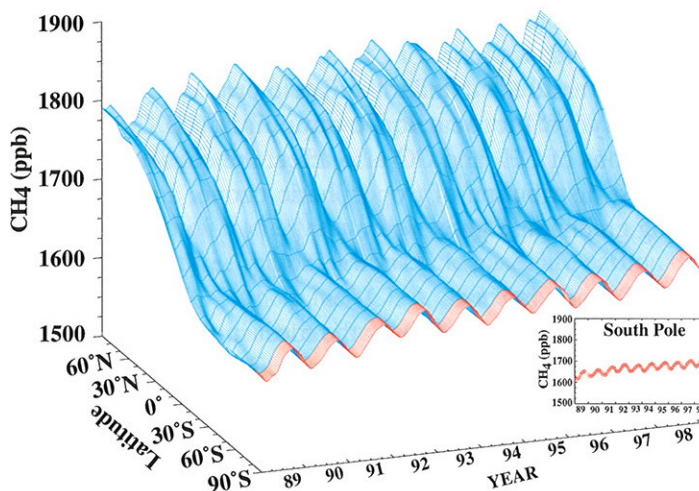


FIG. 71. Three-dimensional representation of the latitudinal distribution of atmospheric methane ( $\text{CH}_4$ ) in the marine boundary layer based on measurements from the NOAA/CMDL cooperative air sampling network. Measurements from South Pole are shown in red. (Analysis provided by CMDL.)



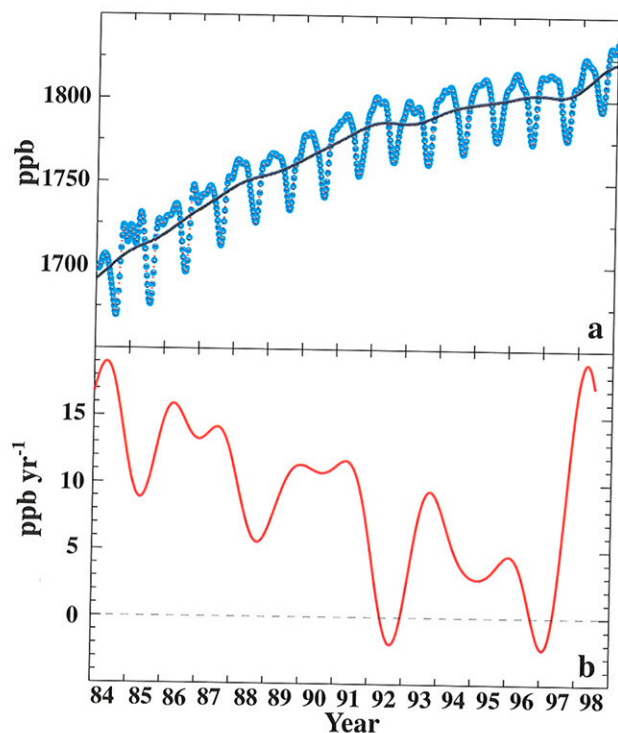


FIG. 72. (a) Methane weekly zonal averages for the latitude band 30°–90°N (blue) and the trend line (black) and (b) the instantaneous  $\text{CH}_4$  growth rate for the latitude band 30°–90°N. (Analysis provided by CMDL.)

### 3) CARBON MONOXIDE

Unlike  $\text{CO}_2$  and  $\text{CH}_4$ , carbon monoxide is not a strong absorber in the terrestrial IR spectral region, yet it still has an impact on climate through its chemistry. The chemistry of CO affects OH (which influences the lifetimes of  $\text{CH}_4$  and HFCs) and tropospheric  $\text{O}_3$  (itself a greenhouse gas), so emissions of CO can be considered equivalent to emissions of  $\text{CH}_4$  (Prather 1996). Current emissions of CO may contribute more to radiative forcing over decadal time-scales than do emissions of anthropogenic  $\text{N}_2\text{O}$  (Daniel and Solomon 1998).

The lifetime of CO is on the order of weeks to months, depending on location and season. As a result, CO has large spatial gradients (Fig. 73). At the South Pole, CO varies from about 30 ppb during summer to 60 ppb in winter. However, CO values are much larger in the Northern Hemisphere where emissions are largest. For example, at Barrow, Alaska, CO varies from 200 ppb during winter to 90 ppb during summer. During most of the 1990s, globally averaged CO amounts decreased by approximately

2%  $\text{yr}^{-1}$ , possibly due to decreased emissions as a result of catalytic converters on automobiles (Bakwin et al. 1994). As with  $\text{CH}_4$  and  $\text{CO}_2$ , 1998 was anomalous in that a significant global increase in CO was observed.

### c. Chlorofluorocarbons (CFCs)

Tropospheric concentrations of total organic equivalent effective chlorine (EECl) continued to decline through the late 1990s (Fig. 74). EECl takes both stratospheric release and the increased weighting of bromine into consideration and essentially represents the ability of the chlorine and bromine in tropospheric gases to contribute to stratospheric ozone depletion. In the past few years, CFC-11, CFC-113, and  $\text{CCl}_4$  all declined at rates of less than 1% per year. CFC-12, which had been increasing in recent years due to its longer lifetime and to continued emission from automobile air conditioners, had a 1999 growth rate near zero in the Northern Hemisphere but continued to increase in the Southern Hemisphere. The growth of CFC-12 concentrations in the Southern Hemisphere results mainly from interhemispheric transport.

The primary gas driving the decrease in total organic chlorine is the solvent methyl chloroform ( $\text{CH}_3\text{CCl}_3$ ) (Fig. 75). The Montreal Protocol banned production of  $\text{CH}_3\text{CCl}_3$  in developed countries in 1996, along with that of the CFCs and carbon tetra-

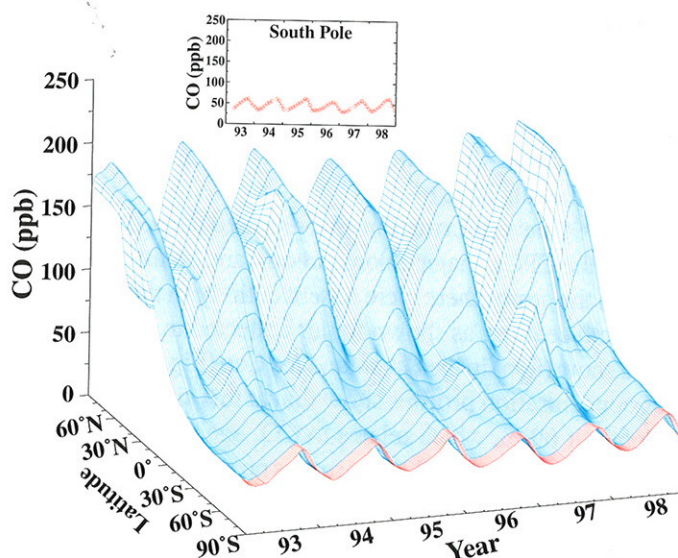


FIG. 73. Three-dimensional representation of the latitudinal distribution of atmospheric carbon monoxide (CO) in the marine boundary layer based on measurements from the NOAA/CMDL cooperative air sampling network. Measurements from South Pole are shown in red. (Analysis provided by CMDL.)



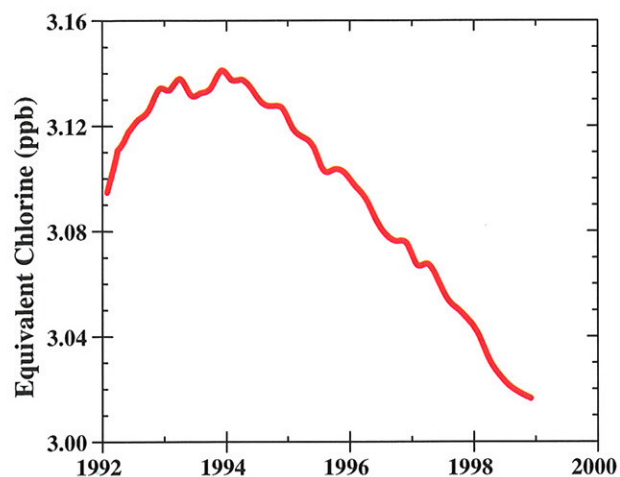


FIG. 74. Total equivalent effective chlorine (EECI) in the troposphere since 1992. (Analysis provided by CMDL.)

chloride ( $\text{CCl}_4$ ), another industrial solvent and a precursor to CFC production. Methyl chloroform has a much shorter lifetime than the CFCs (5–6 years versus 50–120 years) and is therefore being removed more rapidly from the atmosphere at a rate of more than  $15\% \text{ yr}^{-1}$ . This rate will decrease in the future as  $\text{CH}_3\text{CCl}_3$  is depleted from the atmosphere (Montzka et al. 1999).

Increases in halon concentrations, particularly for H-1211 ( $\text{CBrClF}_2$ ) (Butler et al. 1998; Fraser et al. 1998), are also of concern and underscore the need for adherence to the Montreal Protocol guidelines if a decline in total chlorine is to continue. The bromine in these gases has the potential to outweigh the effects of decreasing chlorine in the atmosphere. The atmospheric burden of HCFCs increased during 1999 at rates similar to those reported for the early 1990s (Montzka et al. 1996).

In 1999 new information was reported demonstrating that the CFCs, major chlorocarbons, and halons presently in the atmosphere were absent entirely in the early twentieth century, as shown for air collected in consolidated snow (firn) in the Greenland Ice Cap (Fig. 76). The gas concentration profiles show that at this site beyond a depth of 69 m, which relates to  $\text{CO}_2$  age related concentrations present in 1929, there was no evidence of any of the CFCs, chlorocarbons, and halons listed in Fig. 76. Measurements of these gases in air trapped at high Northern and Southern Hemispheric latitudes showed further that models of anthropogenic emissions could explain the atmospheric histories of these gases (Butler et al. 1999). This work confirmed that the often-invoked

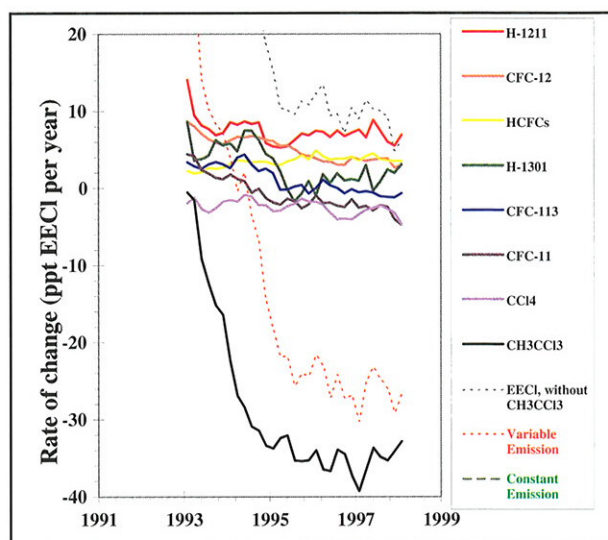


FIG. 75. Contributions of individual halocarbons to equivalent effective chlorine (EECI) since 1993. (Analysis provided by CMDL.)

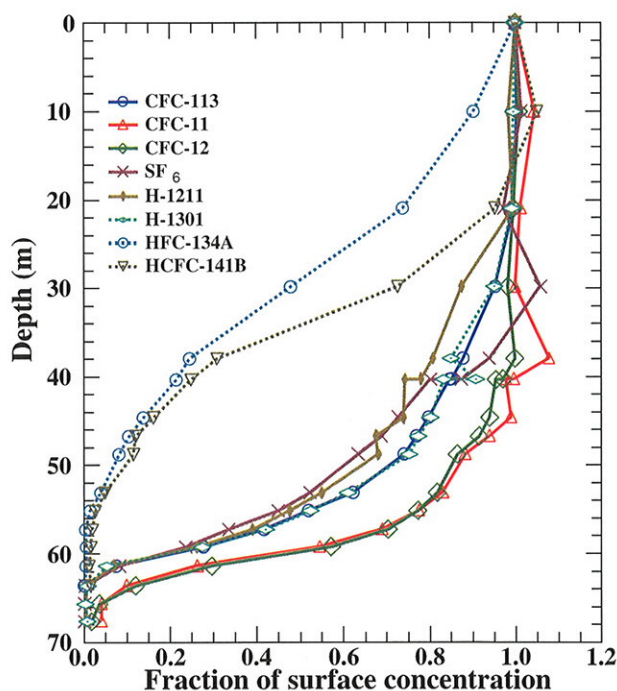


FIG. 76. Measured depth profiles of anthropogenic gases in Greenland firn air. (Analysis provided by CMDL.)

volcanic and biospheric emissions are inconsequential or nonexistent in their effects upon atmospheric budgets of these gases, and that the presence of these gases in the atmosphere is due almost entirely to human sources.



## 6. Seasonal summaries

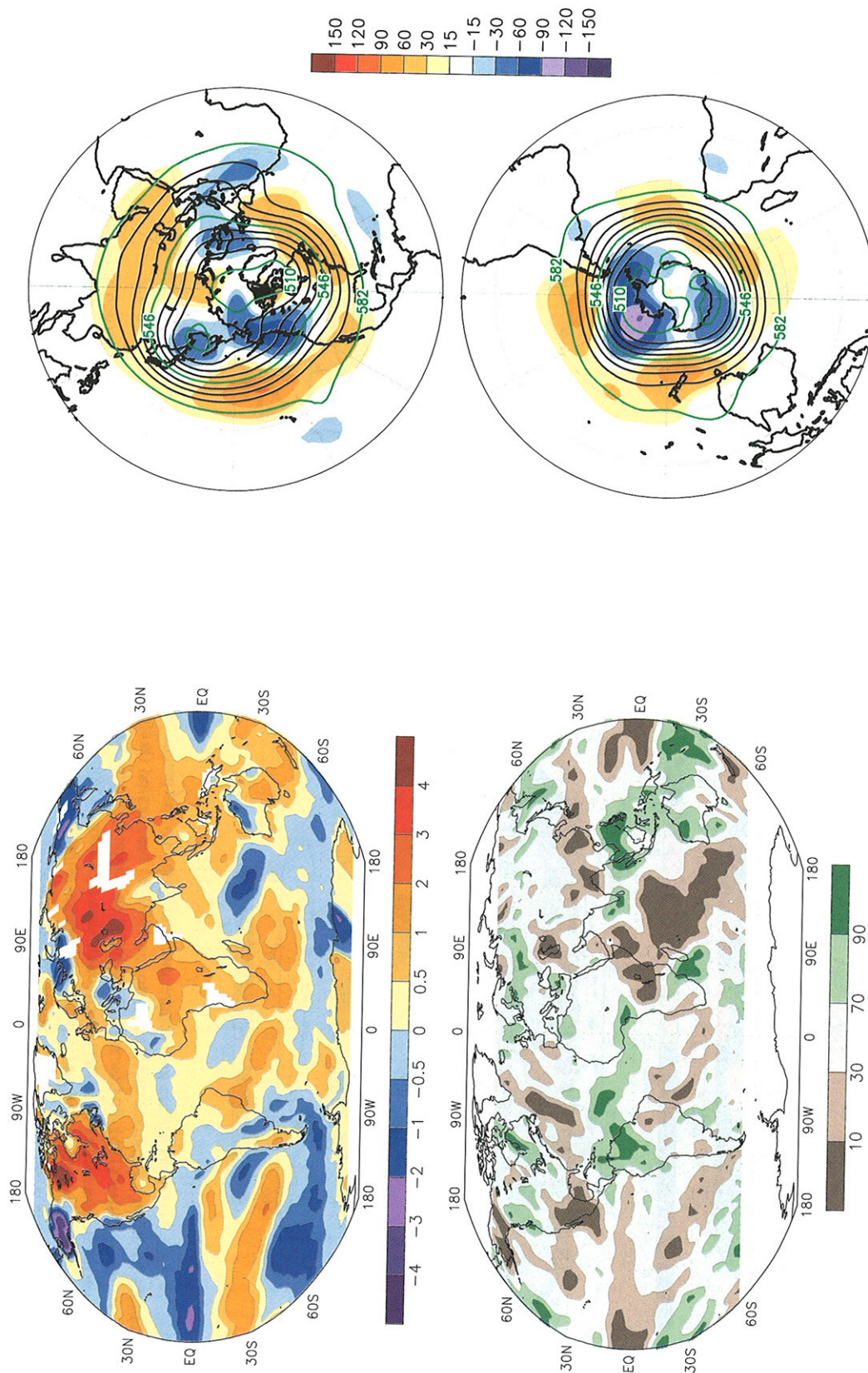


FIG. 77. Dec 1998–Feb 1999 surface temperature anomalies (top, °C) and precipitation percentiles based on a gamma distribution fit to the 1979–95 base period (bottom). Temperature anomalies (1961–90 base period) are based on station data over land and sea surface temperature data over water. Precipitation data are obtained from a merge of rain gauge observations and satellite-derived precipitation estimates (Xie and Arkin 1997). The analysis is omitted in data-sparse regions (white areas).

FIG. 78. Dec 1998–Feb 1999 Northern Hemisphere (top) and Southern Hemisphere (bottom) 500-hPa geopotential heights (contours, interval is 9 dam) and anomalies (shading). Anomalies are departures from the 1979–95 base period means.



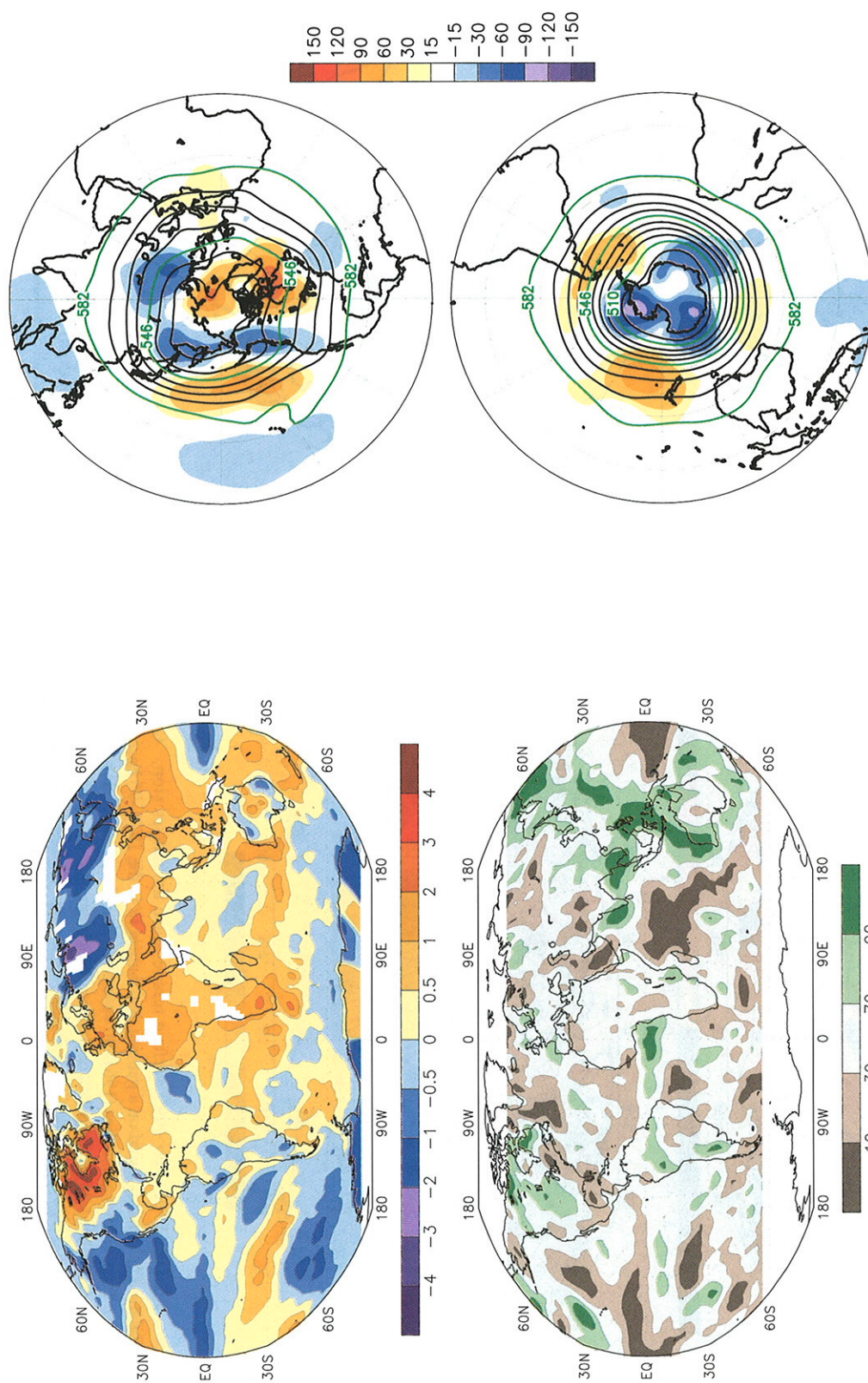


FIG. 79. Mar–May 1999 surface temperature anomalies (top, °C) and precipitation percentiles based on a gamma distribution fit to the 1979–95 base period (bottom). Temperature anomalies (1961–90 base period) are based on station data over land and sea surface temperature data over water. Precipitation data are obtained from a merge of rain gauge observations and satellite-derived precipitation estimates (Xie and Arkin 1997). The analysis is omitted in data-sparse regions (white areas).

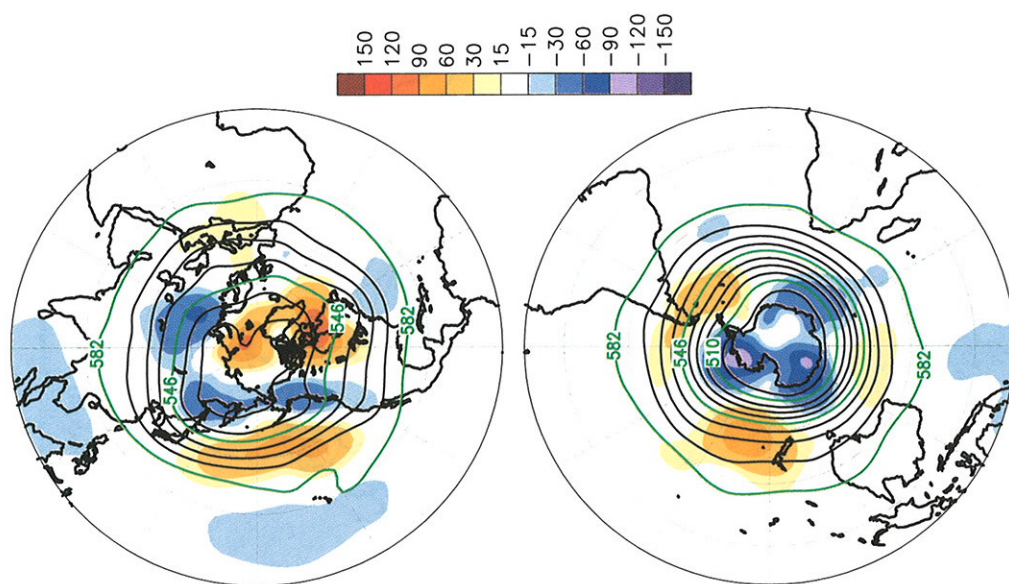


FIG. 80. Mar–May 1999 Northern Hemisphere (top) and Southern Hemisphere (bottom) 500-hPa geopotential heights (contours, interval is 9 dam) and anomalies (shading). Anomalies are departures from the 1979–95 base period means.



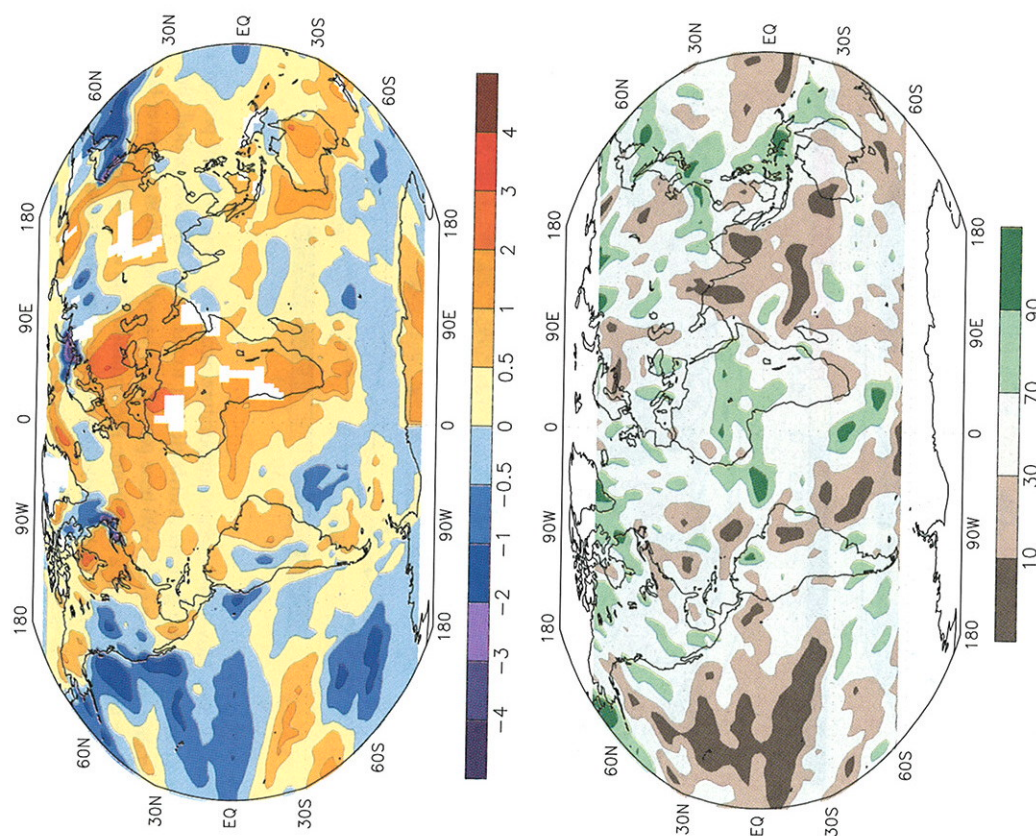


FIG. 81. Jun-Aug 1999 surface temperature anomalies (top, °C) and precipitation percentiles based on a gamma distribution fit to the 1979–95 base period (bottom). Temperature anomalies (1961–90 base period) are based on station data over land and sea surface temperature data over water. Precipitation data are obtained from a merge of rain gauge observations and satellite-derived precipitation estimates (Xie and Arkin 1997). The analysis is omitted in data-sparse regions (white areas).

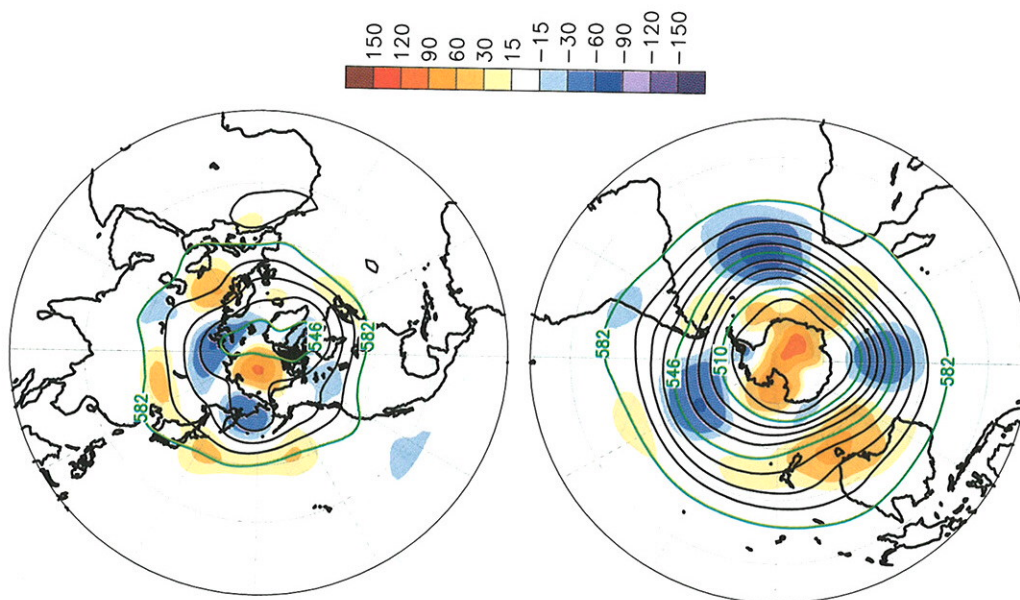


FIG. 82. Jun-Aug 1999 Northern Hemisphere (top) and Southern Hemisphere (bottom) 500-hPa geopotential heights (contours, interval is 9 dam) and anomalies (shading). Anomalies are departures from the 1979–95 base period means.



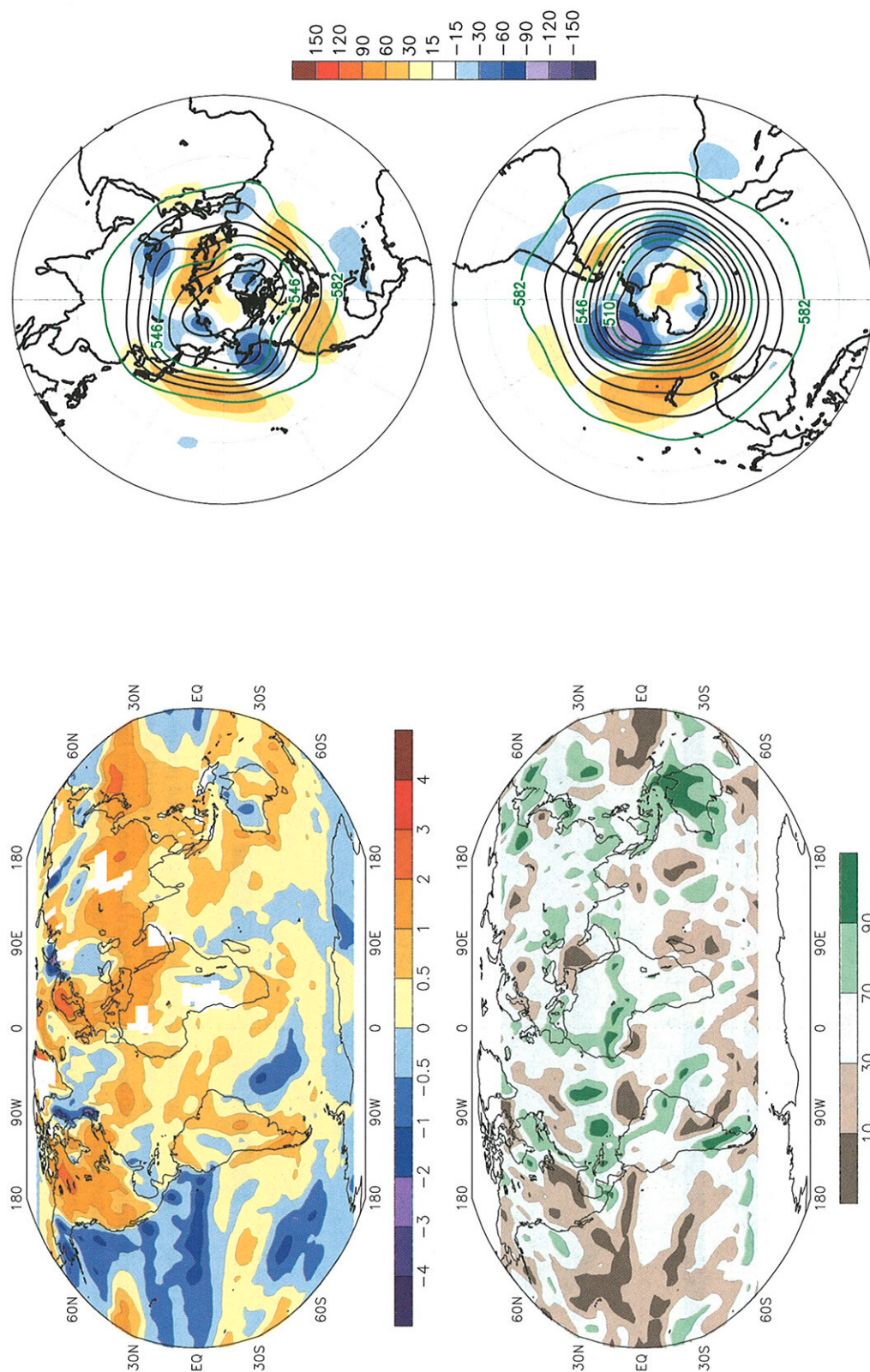


FIG. 83. Sep–Nov 1999 surface temperature anomalies (top, °C) and precipitation percentiles based on a gamma distribution fit to the 1979–95 base period (bottom). Temperature anomalies (1961–90 base period) are based on station data over land and sea surface temperature data over water. Precipitation data are obtained from a merge of rain gauge observations and satellite-derived precipitation estimates (Xie and Arkin 1997). The analysis is omitted in data-sparse regions (white areas).

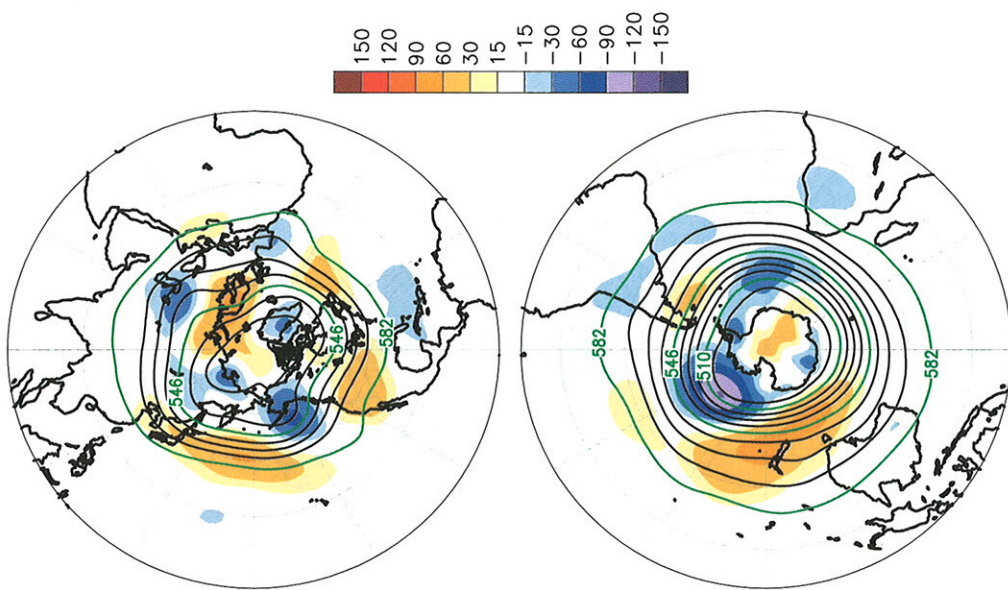


FIG. 84. Sep–Nov 1999 Northern Hemisphere (top) and Southern Hemisphere (bottom) 500-hPa geopotential heights (contours, interval is 9 dam) and anomalies (shading). Anomalies are departures from the 1979–95 base period means.



## Appendix: Contributors

Atmospheric Environment Service, Environment Canada  
 • R. Whitewood

Australian Bureau of Meteorology, National Climate Centre,  
 Climate Analysis Section  
 • W. Wright

Centro de Previsão de Tempo e Estudos Climáticos (CPTEC),  
 Brazil  
 • I. Cavalcanti

Central University of Venezuela, Caracas, Venezuela  
 • L. Hidalgo

Climate Prediction Center/NCEP/NWS/NOAA  
 • D. Lecompte  
 • D. Garrett  
 • M. Gelman  
 • J. Janowiak  
 • C. Long  
 • P. Sabol

Climate Monitoring and Diagnostics Laboratory/ERL/NOAA  
 • J. Butler  
 • T. Conway  
 • E. Dlugokencky  
 • B. Johnson  
 • S. Montzka  
 • P. Novelli  
 • S. Oltmans

Climatic Research Unit, University of East Anglia, United Kingdom  
 • P. Jones

Deutscher Wetterdienst, Hamburg, Germany  
 • G. Rosenhagen

Hadley Centre for Climate Prediction and Research, United  
 Kingdom  
 • B. Horton  
 • D. Parker

Météo-France  
 • Pierre Bessmoulin

World Meteorological Organization  
 • L. Malone  
 • P. Scholefield

*Acknowledgments.* This assessment would not have been possible without the cooperation and contributions from various scientists representing a cross section of the NOAA climate community. We also wish to acknowledge the contributions from the scientists outside of NOAA in other federal laboratories, at universities, and at several sites around the world. All of these scientists are in the contributors list (appendix) and we thank them for their timely and useful input. We are especially grateful to those

international scientists who contributed their time and effort. In addition, we would like to thank J. Janowiak and the anonymous reviewers for their comments that helped to strengthen the article. This assessment is supported by a grant from the NOAA Office of Global Program's Climate Change Data and Detection Program.

## References

- Aceituno, P., 1988: On the functioning of the Southern Oscillation in the South American sector. *Mon. Wea. Rev.*, **116**, 505–525.
- Bakwin, P. S., P. P. Tans, and P. C. Novelli, 1994: Carbon monoxide budget in the Northern Hemisphere. *Geophys. Res. Lett.*, **21**, 433–436.
- Bell, G. D., and L. F. Bosart, 1994: Midtropospheric closed cyclone formation over the southwestern United States, the eastern United States, and the Alps. *Mon. Wea. Rev.*, **122**, 791–813.
- , and M. S. Halpert, 1998: Climate assessment for 1997. *Bull. Amer. Meteor. Soc.*, **79**, S1–S50.
- , and M. Chelliah, 1999: The African easterly jet and its link to Atlantic basin tropical cyclone activity and the global monsoon system. *Proc. 23rd Annual Climate Diagnostics Workshop*, NCEP/NOAA, Miami, FL, 215–218.
- Behringer, D. W., M. Ji, and A. Leetmaa, 1998: An improved coupled model for ENSO prediction and implications for ocean initialization. Part I: The ocean data assimilation system. *Mon. Wea. Rev.*, **126**, 1013–1021.
- Butler, J. H., S. A. Montzka, A. D. Clarke, J. M. Lobert, and J. W. Elkins, 1998: Growth and distribution of halons in the atmosphere. *J. Geophys. Res.*, **103** (D1), 1503–1511.
- , M. Battle, M. Bender, S. A. Montzka, A. D. Clarke, E. S. Saltzman, C. Sucher, J. Severinghaus, and J. W. Elkins, 1999: A record of atmospheric halocarbon concentrations during the twentieth century from polar firn air. *Nature*, **399**, 749–755.
- Ciais, P., P. P. Tans, and M. Trolier, 1995: A large Northern Hemisphere terrestrial CO<sub>2</sub> sink indicated by the <sup>13</sup>C/<sup>12</sup>C ratio of atmospheric CO<sub>2</sub>. *Science*, **269**, 1098–1102.
- Conway, T. J., P. P. Tans, L. S. Waterman, K. W. Thoning, D. R. Kitzis, K. A. Masarie, and N. Zhang, 1994: Evidence for interannual variability of the carbon cycle from the NOAA CMDL global air sampling network. *J. Geophys. Res.*, **99**, 22 831–22 855.
- Dai, A., I. Y. Fung, and A. D. Del Genio, 1997: Surface observed global land precipitation variations during 1900–88. *J. Climate*, **10**, 2943–2961.
- Daniel, J. S., and S. Solomon, 1998: On the climate forcing of carbon monoxide. *J. Geophys. Res.*, **103**, 13 249–13 260.
- Fraser, P. J., D. E. Oram, C. E. Reeves, S. A. Penkett, and A. McCulloch, 1999: Southern Hemispheric halon trends (1978–1998) and global halon emissions. *J. Geophys. Res.*, **104** (D13), 15 985–15 999.
- Gadgil, S. J., P. V. Joseph, and N. V. Joshi, 1984: Ocean–atmosphere coupling over monsoon regions. *Nature*, **312**, 141–143.
- Gray, W. M., 1984: Atlantic seasonal hurricane frequency. Part I: El Niño and 30-mb quasi-biennial oscillation influences. *Mon. Wea. Rev.*, **112**, 1669–1683.



- Gutzler, D. S., and J. W. Preston, 1997: Evidence for a relationship between spring snow cover in North America and summer rainfall in New Mexico. *Geophys. Res. Lett.*, **24**, 2207–2210.
- Halpert, M. S., and C. F. Ropelewski, 1992: Surface temperature patterns associated with the Southern Oscillation. *J. Climate*, **5**, 577–593.
- , and G. D. Bell, 1997: Climate assessment for 1996. *Bull. Amer. Meteor. Soc.*, **78**, S1–S49.
- Hastenrath, S., 1995: Recent advances in tropical climate prediction. *J. Climate*, **8**, 1519–1532.
- Higgins, R. W., K. C. Mo, and Y. Yao, 1998: Interannual variability of the United States summer precipitation regime with emphasis on the southwestern monsoon. *J. Climate*, **11**, 2582–2606.
- Hofmann, D. J., S. J. Oltmans, J. M. Harris, B. J. Johnson, and J. A. Lathrop, 1997: Ten years of ozonesonde measurements at the South Pole: Implications for recovery of springtime Antarctic ozone. *J. Geophys. Res.*, **102**, 8931–8943.
- Janowiak, J., 1988: An investigation of interannual rainfall variability in Africa. *J. Climate*, **3**, 240–255.
- , and P. Xie, 1999: CAMS-OPI: A global satellite-rain gauge merged product for real-time precipitation monitoring applications. *J. Climate*, **12**, 3335–3342.
- Kalnay, E., and Coauthors, 1996: The NCEP/NCAR 40-year Reanalysis Project. *Bull. Amer. Meteor. Soc.*, **77**, 437–471.
- Keeling, C. D., T. P. Whorf, M. Wahlen, and J. Vanderpligt, 1995: Interannual extremes in the rate of rise of atmospheric carbon dioxide since 1980. *Nature*, **375**, 666–670.
- Krishna Kumar, K., B. Rajagopalan, and M. A. Cane, 1999: On the weakening relationship between the Indian monsoon and ENSO. *Science*, **284**, 2156–2159.
- Landsea, C. W., G. D. Bell, W. M. Gray, and S. B. Goldenberg, 1998: The extremely active 1995 Atlantic hurricane season: Environment conditions and verification of seasonal forecasts. *Mon. Wea. Rev.*, **126**, 1174–1193.
- Lelieveld, J., P. J. Crutzen, and C. Brühl, 1993: Climate effects of atmospheric methane. *Chemosphere*, **26**, 739–768.
- Mattocks, R. C., and R. Bleck, 1986: Jet streak dynamics and geostrophic adjustment process during the initial stages of lee cyclogenesis. *Mon. Wea. Rev.*, **114**, 2033–2056.
- Mo, K. C., and V. E. Kousky, 1993: Further analysis of the relationship between circulation anomaly patterns and tropical convection. *J. Geophys. Res.*, **98**, 5103–5113.
- Montzka, S. A., J. H. Butler, R. C. Myers, T. M. Thompson, T. H. Swanson, A. D. Clarke, L. T. Lock, and J. W. Elkins, 1996: Decline in the tropospheric abundance of halogen from halocarbons: Implications for stratospheric ozone depletion. *Science*, **272** (5266), 1318–1322.
- , ———, J. W. Elkins, T. M. Thompson, A. D. Clarke, and L. T. Lock, 1999: Present and future trends in the atmospheric burden of ozone-depleting halogens. *Nature*, **398**, 690–694.
- National Academy of Sciences, 2000: Reconciling observations of global temperature change. [Available from National Academy Press, 2101 Constitution Avenue, NW, Box 285, Washington, DC 20055.]
- Prather, M. J., 1996: Natural modes and time scales in atmospheric chemistry: Theory, GWPs for CH<sub>4</sub> and CO, and runaway growth. *Geophys. Res. Lett.*, **23**, 2597–2600.
- Reed, R. J., D. C. Norquist, and E. E. Recker, 1977: The structure and properties of African wave disturbances as observed during Phase III of GATE. *Mon. Wea. Rev.*, **105**, 317–333.
- Ropelewski, C. F., and M. S. Halpert, 1987: Global and regional scale precipitation patterns associated with the El Niño/Southern Oscillation. *Mon. Wea. Rev.*, **115**, 1606–1626.
- , and ———, 1989: Precipitation patterns associated with the high index phase of the Southern Oscillation. *J. Climate*, **2**, 268–284.
- Shapiro, L. J., and S. B. Goldenberg, 1998: Atlantic sea surface temperatures and tropical cyclone formation. *J. Climate*, **11**, 578–590.
- Simpson, R. H., 1974: The hurricane disaster potential scale. *Weatherwise*, **27**, 169–186.
- Smith, T. M., and R. W. Reynolds, 1998: A high-resolution global sea surface temperature climatology for the 1961–90 base period. *J. Climate*, **11**, 3320–3323.
- Spencer, R. W., and J. R. Christy, 1992: Precision and radiosonde validation of satellite gridpoint temperature anomalies. Part II: A tropospheric retrieval and trends during 1979–90. *J. Climate*, **5**, 858–866.
- , ———, and N. C. Grody, 1990: Global atmospheric temperature monitoring with satellite microwave measurements: Method and results 1979–84. *J. Climate*, **3**, 1111–1128.
- Thompson, D. W. J., and J. M. Wallace, 2000: Annular modes in the extratropical circulation. Part I: Month-to-month variability. *J. Climate*, **13**, 1000–1016.
- Wallace, J. M., and D. S. Gutzler, 1981: Teleconnections in the geopotential height field during the Northern Hemisphere winter. *Mon. Wea. Rev.*, **109**, 785–812.
- WMO/UNEP, 1994: Scientific assessment of ozone depletion: 1994. WMO Rep. 37. [Available from the World Meteorological Organization, Case Postale No. 2300, 1211 Geneva, Switzerland.]